Supplementary Information for

Advanced enzyme-assembled hydrogels for the remediation of contaminated water

Jinlong Zhang[1], Jason C. White[2], Gregory V. Lowry[3], Jinglei He[1], Xuefeng Yu[1], Chuanhao Yan[1], Liang Dong[1], Shu Tao[1], Xilong Wang[1,*]

[1] Laboratory for Earth Surface Processes, College of Urban and Environmental Sciences, Peking University, Beijing 100871, China

[2] The Connecticut Agricultural Experiment Station, New Haven, Connecticut 06511, USA

[3] Department of Civil and Environmental Engineering, Carnegie Mellon University, Pittsburgh, Pennsylvania 15213, USA

[*]Corresponding author

E-mail: xilong@pku.edu.cn (X. Wang)

Number of pages: 110

Number of Notes: 10

Number of Tables: 15

Number of Figures: 49

Table of Contents

1. Supplementary Notes:

2. Supplementary Tables:

3. Supplementary Figures:

Supplementary Note 1: Judgment criterion of charge-assisted hydrogen bond (CAHB) formation in theory.

According to previous studies[1-10], CAHB formation can be determined by one of the following conditions: (1) when both the charged H-donor and H-acceptor are soluble and are small molecules with high purity (such as drugs), CAHB formation is governed by the absolute value of the proton affinity difference between them, expressed as $|\Delta pK_a| = |pK_{a,D} - pK_{a,A}| < \sim 5.0$; (2) when the charged H-donor or H-acceptor is soluble small molecule with high purity and the other one is an insoluble material (such as carbon nanomaterials and hydrogels), CAHB formation is determined by the absolute value of the difference in pK_a and point of zero charge (PZC) between them, since pK_a is typically only applicable to the soluble small molecules with high purity. It can be expressed as $|\Delta PZC| = |PZC - pK_a| < \sim 5.0$; (3) when the charged H-donor or H-acceptor is soluble biomacromolecule (such as enzymes) and the other one is insoluble material, CAHB formation is determined by absolute value of their PZC difference due to the complex composition of biomacromolecules (e.g., enzymes), which is expressed as $|\Delta PZC| = |PZC_{,D} - PZC_{,A}| < \sim 5.0$. The closer the $|\Delta pK_a|$ or $|\Delta PZC|$ to 0, the shorter that bond length of the H-bond (CAHB), the closer the bond angle to 180 °, and the stronger the bond energy would be. This is viewed as a three-center, four-electron covalent bond[7,8,11-16]. In this study, the formation of CAHB between the enzyme (laccase) and cellulose-based hydrogels was determined by their $|\Delta PZC|$ values.

Supplementary Note 2: Bradford method for determination of laccase content.

The laccase content in the supernatant after centrifugation for 20 min at 1900 x g was determined by Bradford method[17,18]. A solid-liquid separation was achieved using the same centrifugation method where needed, unless otherwise indicated. The Bradford method relies on formation of a measurable blue complex between Coomassie Brilliant Blue G-250 (Bradford reagent) and basic amino acids (such as Arginyl and Lysyl)/hydrophobic residues in proteins (i.e., laccase), exhibiting maximum absorption at 595 nm. Briefly, the laccase standard solution with concentrations ranging from 0 to 2.5 mg mL^{-1} was prepared in phosphate solution at pH 5.0. Then, 1.0 mL of laccase standard solution and 5.0 mL of Bradford reagent were evenly mixed for 15 min, and the absorbance at 595 nm was measured by an ultraviolet-visible-near-infrared (UV-Vis-NIR) spectrophotometer (Cary 5000, Agilent, USA). Unless otherwise specified, three replicates were employed for the above and subsequent tests (n = 3). The standard curve between laccase concentration and absorbance at 595 nm was established. Finally, 1.0 mL of the sample to be tested was evenly mixed with 5.0 mL of Bradford reagent, and the absorbance was measured under the abovementioned conditions (n = 3). The amount of laccase in the supernatant after centrifugation was calculated according to the standard curve. In this study, amount of laccase assembled on the Cellulose-CD-MMT hydrogels (mg g^{-1}) was calculated using the following formula:

$$\text{Assembled amount} = \frac{(C_0 - C_e) \times V - C_1 \times V_1}{M} \quad \text{(S1)}$$

where C_0, C_e and C_1 (mg L^{-1}) are concentrations of laccase in the aqueous phase initially added, at equilibrium, and in the cleaning solution, respectively; V and V_1 (L) represent volumes of solution for laccase assembly and the rinsing solution, respectively. M indicates the weight of Cellulose-CD-MMT hydrogels (g).

In addition, the kinetics for laccase assembly was examined within 0-48 h to find out the optimal equilibrium time. In brief, 90 mg of Cellulose-CD-MMT hydrogels were added to 40 mL of phosphate buffer solution that contained 1.0 mg mL^{-1} laccase. Then, the vials were shaken in the dark for 0-48 h at 180 rpm and 25 °C (Supplementary Fig. 46). After then, laccase concentration in the supernatant after centrifugation was measured.

Supplementary Note 3: ABTS method for determination of laccase activity.

The enzymatic activity of laccase was determined by ABTS method[19,20]. First, 1.0 mmol L^{-1} of ABTS solution was prepared in phosphate buffer solution. The free- and assembled laccase was added to 5.0 mL ABTS solution to react for 5 min. Here, the amount of free laccase added was equal to that assembled on the Cellulose-CD-MMT hydrogels. Finally, the absorbance of the aqueous phase was immediately measured at 420 nm with an UV-Vis-NIR spectrophotometer. One unit (1.0 U) is defined as the amount of laccase required to oxidate1.0 nmol substrate per minute[20]. The enzymatic activity of laccase (U g^{-1}) was calculated using the following formula:

$$\text{Laccase activity} = \frac{A \times 10^6 \times V_{\text{total}}}{\varepsilon \times t \times m} \tag{S2}$$

where, A is the absorbance of radical-cation $ABTS^{\bullet+}$ at 420 nm, and the $ABTS^{\bullet+}$ is produced by the oxidation of ABTS by laccase; V_{total} (L) represents the total volume of the reaction system; ε (36000 L mol^{-1} cm^{-1}) is the molar extinction coefficient of $ABTS^{\bullet+}$ at 420 nm; t (min) is the reaction time; m (g) refers to the weight of the free- and assembled laccase. Sorption of ABTS was considered in laccase activity calculation. In the oxidation kinetics of the substrate (ABTS) by both free laccase and that assembled on hydrogels, the kinetics parameters were obtained by measuring the initial reaction rate of laccase in both assembled and free state with ABTS, and the Linewaever-Burk double reciprocal method was used to plot. The formula is as shown below:

$$\frac{1}{v} = \frac{K_{\text{m}}}{v_{\text{max}}} \times \frac{1}{S} + \frac{1}{v_{\text{max}}} \tag{S3}$$

where, v and v_{max} (μmol L^{-1} min^{-1}) represent the initial and maximum oxidation rates of laccase, respectively. K_{m} and S (mmol L^{-1}) represent the Michaelis constant and ABTS concentration, respectively. A lower K_{m} means that the enzyme requires a lower substrate concentration to achieve v_{max} and usually suggests that the enzyme may have a higher affinity for the substrate[21]. v_{max} represents the maximum oxidation rate of substrate by laccase. A greater K_{m} and v_{max} value indicates lower affinity and higher oxidation rate, respectively[21].

Supplementary Note 4: pH, temperature, cyclic operation, storage and assembly stability experiments of immobilized- and free laccase.

As shown in Fig. 2a, to balance the assembled amount and activity of laccase, the Cellulose-CD-MMT hydrogels assembled with laccase at a concentration of 2.0 mg mL^{-1} for its doping were utilized for the stability performance tests (n = 3).

pH and temperature stability: Enzymatic activity of the assembled- and free laccase was measured in phosphate buffer solution at pH 2.0-8.0 to evaluate how pH variation may influence enzymatic stability. Except for the variation of pH, other experimental procedures and conditions are same as those described in Supplementary Note 3. Similarly, the temperature stability experiment of the assembled- and free laccase was performed with the temperature variation from 15 to 65ºC, and other experimental procedures and conditions are consistent with Supplementary Note 3. The relative activity of laccase was calculated using the maximum activity definition of 100%. Unless otherwise specified, the relative activity of laccase in the subsequent experiments was determined by the same method.

Cyclic operation stability: After the first reaction of the assembled laccase with ABTS, the assembled laccase was transferred to 40 mL phosphate buffer (pH 5.0) and shaken for 24 h at 180 rpm and 25 ºC. After centrifugation at 1900 x g for 20 min, the relative activity of the assembled laccase was also measured as described in Supplementary Note 3. The above procedures were repeated 7 times.

Storage stability: The free- and assembled laccase was stored at room temperature for one month, and the laccase activity was measured every 5 days. The relative activity was measured.

Assembly stability: After centrifugation (1900 x g, 20 min), the laccase concentration in the supernatant was measured. Then, the assembled laccase was taken out and transferred to 40 mL phosphate buffer solution (pH 5.0) and shaken for 24 h at 180 rpm and 25 ºC. After centrifugation again, the concentration of laccase in the supernatant was measured. The same

experimental procedures were repeated 7 times. The loading amount of laccase on the Cellulose-CD-MMT hydrogels after each cycle was calculated according to the following formula:

$$\text{Loading amount}_{c} = \frac{C_0 \times V_0 - \sum_{i=0}^{n} (C_{e,i} \times V_i)}{M} \quad \text{(S4)}$$

where C_0 (mg mL^{-1}) is the concentration of laccase in the aqueous phase initially added; V_0 (mL) represents the initial solution volume for laccase assembly; “i” represents the number of cycles; $C_{e,i}$ (mg mL^{-1}) is the equilibrium concentration of laccase in the aqueous phase after “i” cycles; V_i (mL) represents the solution volume for laccase assembly after “i” cycles.

Supplementary Note 5: The test details for compression properties of hydrogels, as well as ^{1}H NMR and ATR-FTIR analysis for the H/D isotope tracer experiment.

In the compression property test of the Cellulose-CD- and Cellulose-CD-MMT hydrogels, a cuboid hydrogel with a length, width and height of 10 mm, 10 mm and 20 mm was placed on the lower plate and compressed by the upper plate at a strain rate of 2 mm min^{-1}. Three replicate measurements were carried out (n = 3).

The H/D isotope replacement method was used to explore the source of the H proton in CAHB formation (solute or solvent). In brief, new phosphate buffer solution was prepared by replacing H_2O and KH_2PO_4 in the original phosphate buffer solution with D_2O and KD_2PO_4, and pH was adjusted with DCl and NaOD. Then, 2.0 mg mL^{-1} laccase solution was added to a 40 mL glass vial containing 90 mg of Cellulose-CD-MMT hydrogels. The solid hydrogels were taken out after shaking for 24 h at 180 rpm and 25 °C, and then freeze-dried for 24 h, ground to powder, and then dried and stored for ^{1}H NMR analysis. Moreover, the assembled laccase sample without deuteration (the phosphate buffer solution prepared by H_2O and KH_2PO_4) was also prepared according to the same procedure as above. Meanwhile, the laccase and Cellulose-CD-MMT hydrogels without assembling laccase were also prepared (the blanks for control) for ^{1}H NMR analysis. Each sample as mentioned above was dissolved in DMSO-d_6, and ^{1}H NMR spectra were recorded on a Bruker Avance NEO 600 MHz spectrometer. In addition, the samples used for ^{1}H NMR analysis were also used for surface functionality detection by an ATR-FTIR spectrometer. The results of ^{1}H NMR and ATR-FTIR analysis for all samples are shown in Supplementary Table 3, Figs. 3c-d, and Supplementary Fig. 11.

Supplementary Note 6: Removal experiments of pollutants.

The removal experiments of PAHs by Cellulose hydrogels, Cellulose-CD hydrogels, Cellulose-CD-MMT hydrogels, free laccase, and laccase-assembled hydrogels were conducted in 15-mL glass vials. Given that concentration of PAHs in the PAHs-polluted natural water and soil porewater are 4.14-16.37 μg L^{-1} and 5.75-34.96 μg L^{-1}, respectively[22-24], solutions with concentrations of 10, 80, 120 μg L^{-1} for PAHs (Nap, Phe, and Pyr) were prepared. The hydrogels (90 mg, Supplementary Table 15) or laccase was added to a 15-mL glass vial containing PAHs solution. The dosage of laccase-assembled hydrogels was the total amount of 90 mg hydrogels loaded with laccase, and that of free laccase was equal to the amount of laccase contained in the laccase-assembled hydrogels. For comparison, removal of PAHs by the inactivated assembled laccase was also measured to determine their possible sorption on laccase-assembled hydrogels. For this purpose, the assembled laccase was subjected to inactivation for 6 h at 90 °C and pH 10 (Supplementary Fig. 47). The degradation efficiency of PAHs by the assembled laccase was calculated by the difference of the total removal efficiency of PAHs by laccase-assembled hydrogels (sorption and degradation) and that by the hydrogels assembled with inactivated laccase (only sorption). The experiments on removal of PAHs by free- and assembled laccase were carried out at the optimal pH and temperature. The laccase-assembled hydrogel does not remain suspended and will precipitate to the bottom within approximately 7 seconds in a 15 mL vial. Hence, the samples were shaken at 180 rpm for 48 h in the dark (25 ºC) to ensure full contact with solution; for future large-scale practical applications, if shaking is unfeasible, stirring might be necessary. Subsequently, the supernatant after centrifugation (1900 x g, 20 min) was collected for UHPLC measurement (conditions present in Supplementary Note 7).

In the PAHs removal kinetics experiment, a corresponding amount of laccase-assembled hydrogels and free laccase was added to a 15 mL glass vial that contained 80 μg L^{-1} Nap, Phe or Pyr solution, and the contact time ranged from 0 to 48 h. After centrifugation at each time point, the same methods and conditions as above were used for determination of the

concentrations of Nap, Phe and Pyr in the aqueous phase.

In the reusability experiment, the laccase-assembled hydrogels were put in 15-mL solution that contained PAHs at 80 μg L^{-1} at pH 5.0, and the vials were shaken in the dark for 6 h at 180 rpm and 25 °C. After centrifugation, the concentration of PAHs in the supernatant was measured. After then, the laccase-assembled hydrogels were rinsed with phosphate buffer solution for 24 h and transferred to 15-mL solution for their removal at a concentration of 80 μg L^{-1}. The above procedures were repeated 10 times.

In the removal experiment of 16 USEPA priority PAHs from real wastewater collected from a Coal Chemical Plant in Ningxia, China, by free laccase and laccase-assembled hydrogels (including inactivated assembled laccase), the experimental procedures were consistent with those in the laboratory-prepared water. Notably, here, pH of the real wastewater was not adjusted, and the pre-experiment shows that the removal equilibrium time was 24 h (Supplementary Fig. 36). PAHs in real wastewater before and after removal were measured according to previous reports[25-27]. Briefly, PAHs in the wastewater were extracted using n-hexane with a liquid-liquid extraction method, followed by separation of the organic phase after stratification. Subsequently, the organic phase was concentrated to 1.0 mL using a rotary evaporator, cleaned up with a silica solid-phase extraction column, and quantified by GC-MS. The above details, the quality control, as well as the results including recoveries, the limit of detection, and blank correction are described elsewhere[25-27].

Sorbed amounts (Q_e, mg kg^{-1}) and the solid-liquid partitioning coefficient (K_d, L kg^{-1}) of PAHs on hydrogels were calculated by the following formula:

$$Q_e = \frac{(C_0 - C_e) \times V_l}{m} \tag{S5}$$

$$K_d = Q_e / C_e \tag{S6}$$

where C_0 and C_e (mg L^{-1}) are concentrations of PAHs initially added and at equilibrium, respectively. The liquid phase volume and weight of hydrogels are represented by V_l (L) and m (kg), respectively.

Removal efficiency (%) of PAHs by free laccase (degradation) and laccase-assembled hydrogels (a sum of sorption and degradation), net degradation efficiency (%) of PAHs by assembled laccase, and degradation rate (μg h^{-1}) of PAHs by free- and assembled laccase are expressed as follows:

$$\text{Removal efficiency} = \frac{C_0 - C_s}{C_0} \times 100\% \quad \text{(S7)}$$

$$\text{Degradation efficiency} = \left(\frac{C_0 - C_s}{C_0} - \frac{C_1 - C_{s1}}{C_1}\right) \times 100\% \quad \text{(S8)}$$

$$\text{Degradation rate}_{free-laccase} = \frac{(C_0 - C_s) \times V_s}{t} \quad \text{(S9)}$$

$$\text{Degradation rate}_{assembled-laccase} = \frac{(C_0 - C_s) - (C_1 - C_{s1})}{t} \times V_s \quad \text{(S10)}$$

where C_0 and C_s (mg L^{-1}) are concentrations of PAHs in the aqueous phase initially added and after removal by free laccase or laccase-assembled hydrogels, respectively. C_1 and C_{s1} (mg L^{-1}) are aqueous-phase concentrations of PAHs in their removal systems initially added and after removal by hydrogels with inactivated laccase (only sorption), respectively. V_s (L) and t (h) refer to the suspension volume and degradation time, respectively.

To investigate the removal and degradation performance of other organic pollutants that are of regulatory or emerging concern by laccase-assembled Cellulose-CD-MMT hydrogels, antibiotics (sulfamethoxazole, and ciprofloxacin) and PFAS (perfluorooctanoic acid, and perfluorooctanesulfonic acid) were selected as representative analytes. The removal procedures of these contaminants were same as those for PAHs, and the redox mediator (10 μmol 1-hydroxybenzotriazole) was additionally added when the laccase-assembled hydrogels or free laccase was added; the specific details and results can be found in Supplementary Fig. 31. All the above experiments were repeated three times (n = 3).

Supplementary Note 7: Concentration determination of PAHs.

After centrifugation, Nap, Phe, and Pyr in the supernatant were quantified by ultra-high performance liquid chromatography (UHPLC, LC-20A, Shimadzu, Japan) equipped with a 2.1×100 mm C18 column (3 μm, Shimadzu). Isocratic elution was performed with a UV detector under the following conditions: 80:20 (v/v) methanol/water at 272 nm for Nap, 90:10 (v/v) methanol/water at 254 nm for Phe. Isocratic elution was performed with a fluorescence detector under the following conditions: 90:10 (v/v) methanol/water with excitation/emission wavelength of 334/391 nm for Pyr. The operating temperature of the instrument was 30 °C, the flow rate was 0.4 mL min^{-1}, and the injection volume was 10 μL. A standard curve using the concentration of PAHs and the corresponding peak area was established for quantification.

Supplementary Note 8: Analytical procedures for PAHs metabolites.

The intermediates of PAHs degraded by free- and assembled laccase were analyzed by gas chromatography-mass spectrometry (GC-MS, 7890A-5975C, Agilent, USA). After centrifugation, the intermediates in 1.0 mL of supernatant were mixed and extracted with 2.0 mL n-hexane, and n-hexane was separated after stratification for further detection. The capillary column used was an HP-5MS capillary column (30 m× 0.25 mm×0.25 μm). High purity helium was used as the carrier gas at a constant flow rate of 1.0 mL min^{-1} and the injected sample volume was 1.0 μL. The initial temperature was programmed to start at 60 °C (1.0 min), increased to 300 °C at 15 °C min^{-1}, and held at 300 °C for 10 min. The mass spectrometer conditions were as follows: ion source 230 °C; electron energy 70 eV; and scan range m/z 20-550 amu. The product peaks were tentatively identified according to standard spectra in a National Institute of Standards and Technology (NIST) mass spectral library and other studies.

Supplementary Note 9: MD simulation details.

Molecular dynamics (MD) simulation was performed with the assistance of the GROMACS 2020.6 software package[28,29]. The Cellulose-CD-MMT hydrogels model comprised a cellulose chain consisting of 5 anhydroglucose units (AGU) connected to a β-cyclodextrin (CD) by the cross-linker (BDE), with an overall chemical formula of $C_{82}H_{138}O_{65}$ (285 atoms) and a total charge of -2. This is because they were in the deprotonated state (the point of zero charge, PZC = 3.74, Supplementary Fig. 17a) in the experiment at pH 5.0. MMT was not considered in the hydrogels model because: (1) MMT did not significantly impact the assembled amount and enzymatic activity of laccase on the hydrogels (Supplementary Fig. 49), only improved their mechanical strength (Fig. 1b); (2) the CAHB interaction between hydrogels and laccase was determined by the PZC difference (ΔPZC) of these participants; the addition of MMT did not significantly change PZC value of the Cellulose-CD hydrogels (3.68, Supplementary Fig. 17b); (3) considering the high accuracy and cost of the subsequent DFT calculation of the representative H-bond conformations obtained by MD simulation, the atomic number (285) of the hydrogels model ($C_{82}H_{138}O_{65}$) was sufficient[30-32]. Hence, it was appropriate to use the $C_{82}H_{138}O_{65}$ model to represent the Cellulose-CD-MMT hydrogels. Meanwhile, the $C_{82}H_{138}O_{65}$ model could also represent the Cellulose-CD hydrogels to calculate the sorption energy of Phe on them and the interaction (e.g., H-bonding) between Cellulose-CD hydrogels and laccase. Geometric optimization of the hydrogels model (Supplementary Fig. 48a) was performed at the quantum chemistry level of B3LYP functional with the 6-311+G** basis set by Gaussian 16[33]. The crystalline structure of laccase (PDB ID: 1GYC, Supplementary Fig. 48b) was obtained from the Protein Data Bank (http://www.pdb.org/pdb/), and laccase protonated at the experimental pH 5.0 using the PROPKA on the PDB2PQR server (https://server.poissonboltzmann.org/). The laccase and hydrogel models were parameterized by the AMBER14SB_parmbsc1 force field[34] and the generalized AMBER force field (GAFF)[35], respectively, and an extended simple point charge (SPC/E) water model was used. The

neutralization of the simulation system was conducted by adding Na^+ or Cl^- counter ions. Atomic charges of the hydrogels were derived on the basis of the restrained electrostatic potential (RESP) that was obtained by Multifwn 3.8 program[36,37]. The acquired RESP atomic charges of the hydrogels model were used in MD simulation. The system containing hydrogels and laccase (Supplementary Fig. 48c) was dissolved in a cubic water box of 10×10×10 nm, and the simulation cells were repeated in three dimensions abiding by the periodic boundary conditions.

Before simulation, 5000 steps of energy minimization using the steepest descent algorithm were carried out for the system that contained hydrogels and laccase with a force tolerance of 100 kJ mol^{-1} nm^{-1}) and allowed water to move freely. Then, the system was equilibrated to 298.15 K through a stepwise heating protocol in the 500 ps canonical ensemble (NVT), followed by 500 ps equilibration in the isothermal-isobaric ensemble (NPT). The pressure was controlled at 1 atm and the temperature was set at 298.15 K using Parrinello-Rahman and V-rescale thermostats, respectively. The formal production simulation duration for the system containing hydrogels and laccase in water was 100 ns (1 atm, 298.15 K) using a time step of 2 fs. The root-mean-square deviation (RMSD) was used to evaluate the stability of the system with GROMACS tools[28,38]. The snapshot rendering, H-bond occupancy, contact and distance analyses were performed by VMD 1.9.4[39].

Supplementary Note 10: DFT calculation details.

Density functional theory (DFT) calculations were performed using Gaussian 16 software package[33] to quantitatively evaluate the strength and stability of different H-bonds between Cellulose-CD-MMT hydrogels and different amino acids (from laccase). The representative H-bond conformations between Cellulose-CD-MMT hydrogels and amino acids in laccase were obtained from MD simulation, which were used in the subsequent DFT calculations. Geometric optimizations and energy calculations were performed using B3LYP functional with the basis sets of 6-311+G** and def2-TZVP, respectively. An implicit solvent using the solvation model based on density (SMD) was used, with water as solvent. Moreover, DFT-D3 (BJ) dispersion correction was used to interpret the dispersion interactions, which is very useful for DFT calculation of non-covalent and covalent interactions[40,41]. No imaginary frequency was found in the frequency calculations of all structures at the same level of theory. The binding energy ($E_{\text{H-bond}}$, kJ mol^{-1}) and energy gap (E_{gap}, eV) of different H-bonds were used to evaluate their strength and stability, respectively[6], and they were calculated as follows:

$$E_{\text{H-bond}} = E_{\text{Hydrogels+AAs}} - E_{\text{Hydrogels}} - E_{\text{AAs}} \tag{S11}$$

$$E_{\text{gap}} = E_{\text{LUMO}} - E_{\text{HOMO}} \tag{S12}$$

where $E_{\text{Hydrogels+AAs}}$, $E_{\text{Hydrogels}}$, and E_{AAs} represent the total energy (kJ mol^{-1}) of Cellulose-CD-MMT hydrogels binding with amino acids (from laccase), Cellulose-CD-MMT hydrogels, and amino acids (from laccase), respectively. E_{HOMO} and E_{LUMO} are the energy (eV) of the highest occupied molecular orbital (HOMO) and the lowest unoccupied molecular orbital (LUMO), respectively. E_{gap} is an important stability index in chemical reactions, and a larger E_{gap} indicates higher molecular stability and lower reactivity[42,43]. E_{gap} visualization image was the output from VMD 1.9.4[39].

In addition, sorption energy (E_{sorp}, kJ mol^{-1}) of Phe on Cellulose- and Cellulose-CD hydrogels, the binding energy (E_{bind}, kJ mol^{-1}) between cellulose and cellulose, and cellulose and MMT

was calculated at the same level as mentioned above. MMT conformation was represented by a cluster model. The feasibility of employing a cluster model to represent MMT for DFT calculation has been demonstrated in previous studies[44-46]. Calculations of E_{sorp} and E_{bind} are as follows:

$$E_{sorp} = E_{Hydrogels+Phe} - E_{Hydrogels} - E_{Phe} \quad \text{(S13)}$$

$$E_{bind} = E_{Cellulose+Cellulose\ or\ MMT} - E_{Cellulose} - E_{Cellulose\ or\ MMT} \quad \text{(S14)}$$

where E_{Phe}, $E_{Hydrogels}$, and $E_{Hydrogels+Phe}$ represent the total energy (kJ mol^{-1}) of Phe, hydrogels (Cellulose or Cellulose-CD), and Phe on hydrogels (Cellulose or Cellulose-CD), respectively. $E_{Cellulose+Cellulose\ or\ MMT}$ represents the total energy (kJ mol^{-1}) of cellulose and cellulose or cellulose and MMT. $E_{Cellulose}$ and $E_{Cellulose\ or\ MMT}$ represent the total energy (kJ mol^{-1}) of cellulose, and cellulose or MMT, respectively.

To predict the reaction sites of PAHs during degradation, the HOMO and the condensed Fukui function (CFF) for three PAHs was calculated at the same DFT calculation level as mentioned above. The calculation of CFF is described as follows[47-49]:

Electrophilic attack: $$f_A^- = q_{N-1}^A - q_N^A \quad \text{(S15)}$$

where q_N^A is the atomic charge of atom A at the corresponding state (N represents neutral, N-1 represents a positive charge). f_A^- is a measure of electrophilic reaction. A larger f_A^- value and the more HOMO distribution indicate a greater likelihood of losing electrons[48,50,51].

Supplementary Table 1. Sorption strength (K_d) of Phe and mechanical strength of the Cellulose-CD-MMT hydrogels and other relevant materials reported in the literature.

Materials	K_d (L kg^{-1})	References
Graphene wool	0.02×10^4	52
Quercus suber cork	0.68×10^4	53
Organo/Layered double hydroxides nanocomposite	0.76×10^4	54
Hexadecylamine functionalised graphene quantum dots	1.01×10^4	55
Cellulose-CD-MMT hydrogels	1.52×10^4	**This work**
Magnetic rice husk-derived biochars	2.50×10^4	56

Materials	Compressive strength (MPa)	References
Cellulose nanofibrils/Hyaluronic acid nanocomposite hydrogels	0.20	57
Hemicellulose-g-polydopamine composite hydrogels	0.30	58
Polyacrylamide/bacterial cellulose nanofibers composite hydrogels	1.60	59
Cellulose nanofiber/polyvinyl alcohol hydrogels	1.70	60
Cellulose-CD-MMT hydrogels	2.19	**This work**
Cellulose/epichlorohydrin hydrogels	2.80	61
Carboxylic-cellulose nanocrystals/acrylic-based hydrogels	3.02	62
Self-reinforced double-crosslinked bacterial cellulose hydrogels	3.17	63
Cellulose/bentonite hydrogels	3.20	64
Cellulose nanofibrils-gelatin composite hydrogels	3.40	65
Double network microcrystalline cellulose hydrogels	4.53	66
Cellulose nanocrystals/polydopamine/poly(vinyl alcohol) composite hydrogels	5.00	67
Cellulose-polyacrylamide interpenetrating network hydrogels	5.62	68

Note: The mechanical strength of hydrogels plays a pivotal role in environmental remediation, significantly influencing their reusability and possible secondary pollution[26,69,70]. In this work, the Cellulose-based hydrogels achieve an optimal balance between mechanical strength (2.19 MPa) and pollutant remediation performance (e.g., high affinity of POPs by the Cellulose-based hydrogels, Fig. 2b), thereby ensuring their excellent applicability and reusability (Fig. 4c).

Supplementary Table 2. Assembly capacity (mg g^{-1}) of laccase on Cellulose-CD-MMT hydrogels and other relevant materials reported in the literature.

Materials	Conditions	Assembly capacity (mg g^{-1})	References
Functionalized cellulose nanofiber/alginate composite hydrogel	pH 6.0, 35 °C, 4.0 mg mL^{-1}	8.50	71
Polytetrafluoroethylene capillary	pH 5.0, 60 °C, 1.5 mg mL^{-1}	32.70	72
Polyethylene terephthalate/amino-functionalized UiO-66(Zr)	pH 4.0, 30 °C, 0.4 mg mL^{-1}	40.97	73
Amino-functionalized ionic liquid-modified magnetic chitosan nanoparticles	pH 3.5, 30 °C, 0.4 mg mL^{-1}	47.00	74
Glycopolymer microspheres	pH 7.0, 40 °C, 2.0 mg mL^{-1}	49.00	75
Biomass-derived functional bacterial cellulose aerogel	pH 4.5, 4 °C, 3.0 mg mL^{-1}	130.4	76
Mesoporous ZIF-8	pH 5.0, 25 °C, 4.0 mg mL^{-1}	400.0	77
Hollow covalent organic framework microsphere	pH 4.5, 30 °C, 1.0 mg mL^{-1}	567.0	78
Cellulose-CD-MMT hydrogels	pH 5.0, 25 °C, 2.0 mg mL^{-1}	754.5	**This work**
Hollow mesoporous carbon nanospheres	pH 4.5, 30 °C, 1.0 mg mL^{-1}	835.0	79

Supplementary Table 3. All characteristic peaks on ^{1}H NMR spectra of laccase before and after assembled (including deuteration) on Cellulose-CD-MMT hydrogels.

Samples	Characteristic peaks (δ, ppm)		
	Polysaccharide/Aliphatic H[80-83]	**Aromatic H**[81,83]	**Strong H-bonds**[6,84]
Cellulose-CD-MMT hydrogels	1.11, 3.56, 3.62, 4.48, 4.83	-	-
Laccase	1.50, 2.20, 3.81	7.22	-
Cellulose-CD-MMT hydrogels + laccase	1.50, 2.20, 3.56, 3.62, 3.81, 4.47, 4.83	7.22	17.62
Cellulose-CD-MMT hydrogels + laccase (deuteration)	1.50, 2.21, 3.56, 3.64, 3.81, 4.83	7.22	-

The peaks at 3.35 and 2.50 ppm belonging to H_2O and DMSO-d_6,[6] respectively, occurred on the ^{1}H NMR spectra of all samples.

Supplementary Table 4. Absolute activity of free- and assembled laccase as shown in Fig. 2.

Fig. 2b	**Absolute enzymatic activity (U g^{-1})**		**Fig. 2c**	**Absolute enzymatic activity (U g^{-1})**	
pH	Free laccase	Assembled laccase	Temperature (°C)	Free laccase	Assembled laccase
2	69.82	147.26	15	100.06	172.49
3	132.94	186.68	25	124.14	206.51
4	138.19	191.44	35	135.73	200.10
5	109.33	194.22	45	144.44	196.64
6	66.91	185.57	55	112.07	189.02
7	36.48	173.60	65	95.41	164.67
8	29.31	143.68			
Fig. 2d	**Absolute enzymatic activity (U g^{-1})**		**Fig. 2e**	**Absolute enzymatic activity (U g^{-1})**	
Storage time (day)	Free laccase	Assembled laccase	Cycles	Free laccase[a]	Assembled laccase
0	143.62	204.21	1	-	204.12
5	127.59	203.29	2	-	200.55
10	107.33	200.72	3	-	197.94
15	94.41	198.51	4	-	197.01
20	83.41	197.36	5	-	195.83
25	83.81	196.33	6	-	194.91
30	81.90	195.79	7	-	194.24

[a] The enzymatic activity of free laccase cannot be determined due to its non-recyclability. The laccase was from *Trametes versicolor*.

Supplementary Table 5. Comprehensive comparison between the assembly strategy of laccase on Cellulose-CD-MMT hydrogels in this work and the immobilization methods of laccase on various carriers including those presented in Fig. 2g (nano or porous materials) and Supplementary Fig. 16 (hydrogel carriers) in previous reports in terms of pH and operational range of temperature (maintaining in excess of 80% of enzymatic activity), suitable pH and temperature for environmental remediation, storage stability, and reusability (7 cycles).

Immobilization/assembly methods	Carriers (nano or porous materials)	pH range	Suitable pH for environmental remediation	Temperature range (°C)	Suitable temperature for environmental remediation (°C)	Storage stability (%)	Reusability (%)
Emulsion-interfacial strategy[78]	Hollow covalent organic framework microsphere	3.5-6.5	5.0	40-55	40	71.0	90.0
Covalent binding[79]	Hollow mesoporous carbon nanospheres	2.5-7.5	4.5	60	60	79.0	70.0
Covalent binding[85]	Chitosan/poly (vinyl alcohol) composite nanofibrous membranes	3.0-5.0	4.0	30-45	40	18.0	20.0
One-Pot encapsulation[86]	Cu (PABA)-MOF nanoarchitectonics	3.0-6.0	5.0	30-50	45	88.0	79.0
Physical sorption[74]	Amino-functionalized ionic liquid-modified magnetic chitosan nanoparticles	3.0-4.5	3.5	45-65	55	95.0	93.2
Immobilization/assembly methods	**Carriers (hydrogel materials)**	**pH range**	**Suitable pH for environmental remediation**	**Temperature range (°C)**	**Suitable temperature for environmental remediation (°C)**	**Storage stability (%)**	**Reusability (%)**
Covalent binding[87]	3D Graphene/polymer composite hydrogels	4.5	4.5	25	25	-	-
Encapsulation[88]	Bimetallic Cu/ZIFs/poly (vinyl alcohol) hydrogels	3.0-5.0	3.0	45-65	55	90.0	70.0
Encapsulation[89]	Zwitterionic poly-carboxybetaine hydrogels	1.0-2.0	1.0	60-70	60	95.0	55.0

Physical sorption[71]	Functionalized cellulose nanofiber/alginate composite hydrogel	4.0-5.5	4.0	45-65	50	91.8	91.5
Ion coordination[76]	Biomass-derived functional bacterial cellulose aerogel	3.5-5.0	4.5	45-50	50	60.0	57.5
Entrapment/adsorption[90]	Agarose hydrogel	6.0-8.0	7.0	60-70	60	95.0	85.0
Covalent binding[91]	Silica colloidal hydrogel crystal beads	4.0-8.0	5.0	15-55	55	65.0	73.7
3D bioprinting[92]	Sodium alginate/acrylamide/ hydroxyapatite hydrogels	4.5-6.0	5.5	50-55	50	80.0	61.0
Charged-assisted H-bonding (**This work**)	Cellulose-CD-MMT hydrogels	3.0-7.0	5.0	15-55	25	95.9	95.2

Supplementary Table 6. Absolute activity of free- and assembled enzymes (catalase, lipase, and laccase from *Aspergillus*) in Supplementary Figs. 18-20.

Supplementary Fig. 18a	**Absolute enzymatic activity (U g^{-1})**		**Supplementary Fig. 18b**	**Absolute enzymatic activity (U g^{-1})**	
pH	Free catalase	Assembled catalase	Temperature (°C)	Free catalase	Assembled catalase
2	322.3	1506.5	15	1378.1	2256.0
3	660.6	1921.9	25	1565.0	2422.5
4	993.9	2168.7	35	1618.4	2433.5
5	1226.2	2276.3	45	1463.6	2336.6
6	1475.5	2410.0	55	1247.8	2263.5
7	1570.6	2436.9	65	835.8	1926.5
8	1481.3	2420.4			
Supplementary Fig. 19a	**Absolute enzymatic activity (U g^{-1})**		**Supplementary Fig. 19b**	**Absolute enzymatic activity (U g^{-1})**	
pH	Free lipase	Assembled lipase	Temperature (°C)	Free lipase	Assembled lipase
2	4.91	14.74	15	11.51	22.65
3	5.56	17.60	25	14.81	25.54
4	7.91	22.55	35	15.94	25.20
5	11.79	24.11	45	15.00	24.94
6	15.22	25.08	55	12.24	23.60
7	16.22	26.04	65	10.49	20.28
8	15.85	25.80			
Supplementary Fig. 20a	**Absolute enzymatic activity (U g^{-1})**		**Supplementary Fig. 20b**	**Absolute enzymatic activity (U g^{-1})**	
pH	Free laccase[a]	Assembled laccase[a]	Temperature (°C)	Free laccase[a]	Assembled laccase[a]
2	104.12	190.71	15	98.77	200.56
3	110.02	233.15	25	129.70	237.89
4	167.46	238.67	35	167.77	230.57
5	130.81	242.00	45	154.12	224.02
6	100.93	221.37	55	123.12	206.26
7	63.23	200.36	65	94.39	187.48
8	38.17	147.01			

[a] The laccase was from *Aspergillus*. **Note:** Sorption of substrate was considered in enzymatic activity calculation of these enzymes.

Supplementary Table 7. The electron energy changes ($E_{H\text{-}bond}$, kJ mol^{-1}), bond length (Å), and bond angle (º) of different H-bond configurations obtained by MD simulation.

H-bond configurations	|ΔPZC|	H-bond types	$E_{H\text{-}bond}$ (kJ mol^{-1})	Bond length (Å)	Bond angle (º)
Cellulose-CD-MMT hydrogels + Asp	1.37	CAHB	-124.01	2.473	179.18
Cellulose-CD-MMT hydrogels + Arg	8.67	Ordinary H-bond	-13.57	2.828	167.98
Cellulose-CD-MMT hydrogels + His	9.36	Ordinary H-bond	-14.82	2.787	169.28

Supplementary Table 8. Literature review on degradation of PAHs by free laccase without mediators in the aqueous phase.

PAHs	Initial concentration (mg L^{-1})	Time (h)	Degradation efficiency (%)	Mediators	References
Naphthalene	0.010	24	51.2	No	93
Phenanthrene	0.010	24	41.6	No	
Anthracene	0.010	24	60.2	No	
Benzo(*a*)anthracene	0.010	24	51.6	No	
Chrysene	0.010	24	39.4	No	
Benzo(*b*)fluoranthene	0.010	24	39.9	No	
Benzo(*a*)pyrene	0.010	24	39.1	No	
Naphthalene	0.050	24	~38.0	No	94
Phenanthrene	0.050	24	~62.0	No	
Benzo(*a*)anthracene	0.050	24	~43.0	No	
Phenanthrene	0.411	24	49.0	No	95
Acenaphthene	0.007	48	61.9	No	96
Fluorene	0.017	48	52.0	No	
Phenanthrene	0.098	48	44.0	No	
Anthracene	1.000	48	81.9	No	97
Benzo(*a*)pyrene	1.000	48	69.2	No	
Anthracene	350.0	240	75.0	No	98

Benzo(*b*)fluoranthene	0.131	120	~53.0	No	99
Chrysene	0.165	120	~65.0	No	
Benzo(*a*)anthracene	0.150	120	~56.0	No	
Pyrene	0.144	120	~55.0	No	
Fluoranthene	0.162	120	~57.0	No	
Phenanthrene	1.000	120	~84.0	No	
Fluorene	0.084	120	~43.0	No	
Naphthalene	1.000	120	~99.0	No	
Phenanthrene	100.0	24	98.0	No	100
Anthracene	10.00	24	43.6	No	101
Fluorene	10.00	24	41.7	No	
Benzo(*a*)pyrene	6.308	24	~24.0	No	102
Naphthalene	43.00	48	94.0	No	103
Phenanthrene	27.00	48	88.0	No	
Anthracene	19.00	48	63.0	No	
Acenaphthylene	3.805	72	37.0	No	104
Pyrene	2.022	48	40.0	No	105
Fluorene	1.662	48	95.0	No	
Fluoranthene	2.022	240	47.0	No	
Anthracene	1.782	48	91.0	No	

Phenanthrene	100.0	36	46.0	No	106
Naphthalene Phenanthrene	15.00 0.645	336 336	46.3 39.1	No No	107
Benzo(*a*)pyrene	60.00	72	~27.0	No	108
Benzo(*a*)pyrene Anthracene	1.000 1.000	24 24	~25.0 ~30.0	No No	109
Benzo(*a*)pyrene	1.000	48	69.1	No	110
Naphthalene	0.256	5	70.0	No	111
Phenanthrene	0.500	24	~50.0	No	112
Naphthalene Phenanthrene Pyrene	0.120 0.120 0.120	48 48 48	39.3 36.6 20.6	No No No	**Our work**

Note: The degradation efficiency presented in the table reflects the efficiency at which PAHs are degraded by free laccase without mediator. In these specific examples, the degradation efficiency was enhanced through various optimization strategies, such as improving substrate diffusion/mass transfer (e.g., by adding organic solvents), increasing redox potential/electron transfer rates (e.g., by introducing mediators), and enhancing enzymatic activity/stability (e.g., through immobilization). This indicates that the redox potential of free laccase may be not the sole factor limiting PAHs degradation.

Supplementary Table 9. Measured concentrations of 16 USEPA priority PAHs in a Coal Chemical Plant wastewater collected from Ningxia, China, including Nap, Phe and Pyr studied in the lab-scale trials. The table also includes the structures and n-octanol/water partitioning coefficient (LogK_{ow}) of 16 USEPA priority PAHs.

Chemicals	**Molecular formula**	**Molecular structure**	**LogK_{ow}[a]**	**Real wastewater[b] (μg L^{-1})**	**LOD[c] (μg L^{-1})**
Naphthalene (Nap)	$C_{10}H_8$	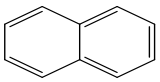	3.30	452.30	0.657
Acenaphthylene (Acy)	$C_{12}H_8$	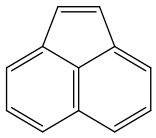	3.93	152.96	0.563
Acenaphthene (Ace)	$C_{12}H_{10}$	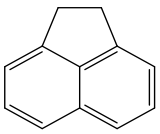	3.92	21.58	0.184
Fluorene (Flu)	$C_{13}H_{10}$	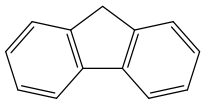	4.18	71.08	0.327
Phenanthrene (Phe)	$C_{14}H_{10}$	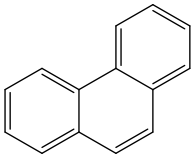	4.46	124.50	0.503
Anthracene (Ant)	$C_{14}H_{10}$	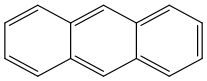	4.45	37.33	0.258
Fluoranthene (Fluh)	$C_{16}H_{10}$	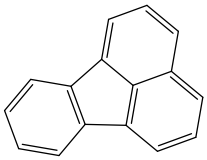	5.16	77.78	0.248
Pyrene (Pyr)	$C_{16}H_{10}$	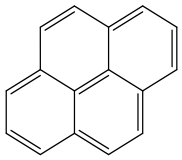	4.88	55.24	0.643
Benzo(*a*)anthracene (B*a*A)	$C_{18}H_{12}$	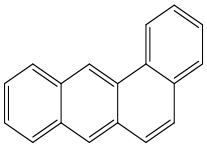	5.76	24.47	0.200
Chrysene (Chy)	$C_{18}H_{12}$	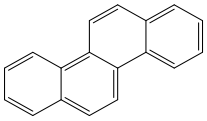	5.73	17.99	0.354

Chemicals	Molecular formula	Molecular structure	LogK_{ow}[a]	Real wastewater[b] (μg L^{-1})	LOD[c] (μg L^{-1})
Benzo(*b*)fluoranthene (B*b*F)	$C_{20}H_{12}$	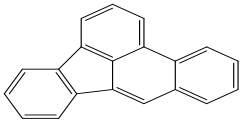	5.78	23.13	0.548
Benzo(*k*)fluoranthene (B*k*F)	$C_{20}H_{12}$	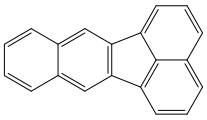	6.11	12.81	0.691
Benzo(*a*)pyrene (B*a*P)	$C_{20}H_{12}$	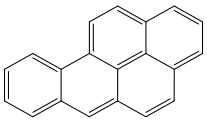	6.13	16.82	0.628
Dibenzo(*a,h*)anthracene (DBA)	$C_{22}H_{14}$	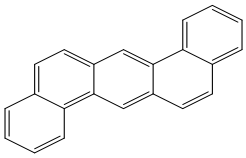	6.50	5.39	0.748
Indeno(*1,2,3-cd*)pyrene (IDP)	$C_{22}H_{12}$	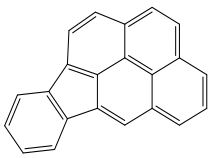	6.58	6.27	0.690
Benzo(*g,h,i*)perylene (B*g*P)	$C_{22}H_{12}$	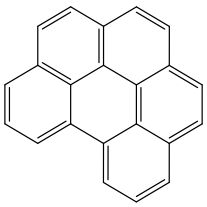	6.63	7.34	0.655

[a] N-octanol/water partitioning coefficient. A higher LogK_{ow} value means the compound is more hydrophobic. The data were obtained from website of https://pubchem.ncbi.nlm.nih.gov/ (accessed Nov 12, 2023). [b] Concentrations of PAHs in a Coal Chemical Plant wastewater collected from Ningxia, China, determined following previous reports[25-27] [c] The limit of detection[25,26].

Supplementary Table 10. Main water quality parameters of wastewater from a Coal Chemical Plant collected from Ningxia, China.

Parameters	Value	Parameters	Value
pH	6.43	Ca^{2+} (mg L^{-1})	26.9
Total organic carbon (mg L^{-1})	835	Na^{+} (mg L^{-1})	933
Electrical conductivity (ms cm^{-1})	3.51	Mg^{2+} (mg L^{-1})	20.5
Turbidity (NTU)	38.5	Cl^{-} (mg L^{-1})	475
Redox potential (mV)	237.3	HCO_3^{-} (mg L^{-1})	345
Total hardness (mg L^{-1})	153.3	SO_4^{2-} (mg L^{-1})	169
K^{+} (mg L^{-1})	4.90	NO_3^{-} (mg L^{-1})	123

Supplementary Table 11. Removal performance of 16 USEPA PAHs in real wastewater/sludge, PFAS (e.g., PFOS) and antibiotics (e.g., SMX) by the advanced laccase-assembled Cellulose-CD-MMT hydrogels (sorption and degradation) in this work and the other materials or approaches in previous reports.

Materials or approaches	Removal efficiency (%) of 16 USEPA PAHs; Time (h); Initial concentration (mg L^{-1})	References
CuO decorated montmorillonite; Synergistic sorption/photo-Fenton	66.0; 4.0; 0.14	113
Immobilized degrading bacteria in PVA-SA hydrogel beads; Sorption and degradation	77.0; 96; 1.05	26
Electrochemical Fe^{2+}-activated peroxymonosulfate oxidation	80.8; 1.0; 1.36	114
Ultrasound-Fenton process	84.4; 0.7; 5.73	115
PAH-degrading rhizobacteria of Lepironia	89.0; 120; 5.40	116
Advanced laccase-assembled Cellulose-CD-MMT hydrogels; Sorption and degradation	89.3; 24; 1.12	**This work**
Materials or approaches	**Removal efficiency (%) of PFOS; Time (h); Initial concentration (μg L^{-1})**	**References**
Fe/Al-Filings-based Green Environmental Media; Sorption	46.0; 30; 2.50	117
Laccase-Mediator System; Degradation	59.0; 3888; 500	118
Low and highly boron-doped diamond electrodes; Electrochemical oxidation	78.0; 8.0; 3.28	119
Combining electrochemistry and ultraviolet radiation	85.0; 4.0; 30.0	120
Advanced laccase-assembled Cellulose-CD-MMT hydrogels; Sorption and degradation	90.9; 48; 1.00	**This work**
Peroxydisulfate activation mediated by boron modified Fe/C catalysts	94.0; 1.0; 1000	121
Materials or approaches	**Removal efficiency (%) of SMX; Time (h); Initial concentration (mg L^{-1})**	**References**
Bacterial laccase immobilized on chitin; Degradation	38.7; 48; 50.0	122
Electrolysis-integrated tidal flow constructed wetland system	81.9; 48; 1.00	123
Ball milled biochar; Sorption	83.3; 24; 10.0	124
$BiVO_4/SrTiO_3$ composite; Photocatalytic degradation	91.0; 1.0; 10.0	125
Advanced laccase-assembled Cellulose-CD-MMT hydrogels; Sorption and degradation	93.6; 48; 0.001	**This work**
Nitrogen-doped nanocarbon derived from candle soot for persulfate activation	95.5; 2.0; 10.0	126

Supplementary Table 12. Values of f_A^- for each atom in Phe molecule.

No.(Atom)	q_N^A	q_{N+1}^A	q_{N-1}^A	f_A^-	No.(Atom)	q_N^A	q_{N+1}^A	q_{N-1}^A	f_A^-
1 (C)	-0.0099	-0.0442	0.0233	0.0332	**13 (C)**	-0.0481	-0.0817	-0.0163	0.0318
2 (C)	-0.0099	-0.0442	0.0233	0.0332	**14 (C)**	-0.0481	-0.0817	-0.0163	0.0318
3 (C)	-0.0117	-0.0475	0.0224	0.0342	**15 (H)**	0.0520	0.0109	0.0878	0.0358
4 (C)	-0.0117	-0.0475	0.0224	0.0342	**16 (H)**	0.0520	0.0109	0.0878	0.0358
5 (C)	-0.0467	-0.1443	0.0510	0.0977	**17 (H)**	0.0506	0.0319	0.0713	0.0207
6 (C)	-0.0467	-0.1443	0.0510	0.0977	**18 (H)**	0.0506	0.0319	0.0713	0.0207
7 (C)	-0.0459	-0.0884	0.0022	0.0481	**19 (H)**	0.0511	0.0267	0.0753	0.0242
8 (C)	-0.0459	-0.0884	0.0022	0.0481	**20 (H)**	0.0511	0.0267	0.0753	0.0242
9 (C)	-0.0452	-0.0983	0.0155	0.0607	**21 (H)**	0.0502	0.0187	0.0766	0.0264
10 (C)	-0.0452	-0.0983	0.0155	0.0607	**22 (H)**	0.0502	0.0187	0.0766	0.0264
11 (C)	-0.0470	-0.1163	0.0228	0.0698	**23 (H)**	0.0507	0.0331	0.0680	0.0173
12 (C)	-0.0470	-0.1163	0.0228	0.0698	**24 (H)**	0.0507	0.0331	0.0680	0.0173

Supplementary Table 13. Values of f_A^- for each atom in Nap molecule.

No.(Atom)	q_N^A	q_{N+1}^A	q_{N-1}^A	f_A^-	No.(Atom)	q_N^A	q_{N+1}^A	q_{N-1}^A	f_A^-
1 (C)	-0.0111	-0.0410	0.0160	0.0271	**10 (C)**	-0.0487	-0.1217	0.0221	0.0708
2 (C)	-0.0111	-0.0410	0.0160	0.0271	**11 (H)**	0.0507	0.0130	0.0867	0.0360
3 (C)	-0.0462	-0.1356	0.0529	0.0991	**12 (H)**	0.0507	0.0130	0.0867	0.0360
4 (C)	-0.0462	-0.1356	0.0529	0.0991	**13 (H)**	0.0507	0.0130	0.0867	0.0360
5 (C)	-0.0462	-0.1356	0.0529	0.0991	**14 (H)**	0.0507	0.0130	0.0867	0.0360
6 (C)	-0.0462	-0.1356	0.0529	0.0991	**15 (H)**	0.0498	0.0151	0.0804	0.0306
7 (C)	-0.0487	-0.1217	0.0221	0.0708	**16 (H)**	0.0498	0.0151	0.0804	0.0306
8 (C)	-0.0487	-0.1217	0.0221	0.0708	**17 (H)**	0.0498	0.0151	0.0804	0.0306
9 (C)	-0.0487	-0.1217	0.0221	0.0708	**18((H)**	0.0498	0.0151	0.0804	0.0306

Supplementary Table 14. Values of f_A^- for each atom in Pyr molecule.

No.(Atom)	q_N^A	q_{N+1}^A	q_{N-1}^A	f_A^-	No.(Atom)	q_N^A	q_{N+1}^A	q_{N-1}^A	f_A^-
1 (C)	-0.0087	-0.0240	0.0067	0.0153	**14 (C)**	-0.0459	-0.1179	0.0292	0.0751
2 (C)	-0.0087	-0.0240	0.0067	0.0153	**15 (C)**	-0.0478	-0.0834	-0.0154	0.0324
3 (C)	-0.0109	-0.0442	0.0224	0.0333	**16 (C)**	-0.0478	-0.0834	-0.0154	0.0324
4 (C)	-0.0109	-0.0442	0.0224	0.0333	**17 (H)**	0.0527	0.0285	0.0762	0.0235
5 (C)	-0.0109	-0.0442	0.0224	0.0333	**18 (H)**	0.0527	0.0285	0.0762	0.0235
6 (C)	-0.0109	-0.0442	0.0224	0.0333	**19 (H)**	0.0527	0.0285	0.0762	0.0235
7 (C)	-0.0444	-0.0996	0.0134	0.0578	**20 (H)**	0.0527	0.0285	0.0762	0.0235
8 (C)	-0.0444	-0.0996	0.0134	0.0578	**21 (H)**	0.0513	0.0208	0.0787	0.0274
9 (C)	-0.0444	-0.0996	0.0134	0.0578	**22 (H)**	0.0513	0.0208	0.0787	0.0274
10 (C)	-0.0444	-0.0996	0.0134	0.0578	**23 (H)**	0.0512	0.0208	0.0787	0.0275
11 (C)	-0.0459	-0.1179	0.0292	0.0751	**24 (H)**	0.0512	0.0208	0.0787	0.0275
12 (C)	-0.0459	-0.1179	0.0292	0.0751	**25 (H)**	0.0510	0.0324	0.0689	0.0179
13 (C)	-0.0459	-0.1179	0.0292	0.0751	**26 (H)**	0.0510	0.0324	0.0689	0.0179

Supplementary Table 15. Solid-to-liquid ratio tested results for partitioning coefficient (K_d, L kg^{-1}) of PAHs (e.g., Phe) on hydrogels.

Hydrogel dose (mg)	Solution volume (mL)	Phe concentration (μg L^{-1})	Partitioning coefficient (K_d, L kg^{-1})	Optimal solid-to-liquid ratio (g mL^{-1})
18 mg	15.0	10	0.51×10^4	
18 mg	15.0	80	0.65×10^4	
18 mg	15.0	120	0.66×10^4	
54 mg	15.0	10	0.76×10^4	
54 mg	15.0	80	0.85×10^4	
54 mg	15.0	120	1.12×10^4	
90 mg	**15.0**	**10**	**0.99×10^4**	3:500
90 mg	**15.0**	**80**	**1.04×10^4**	
90 mg	**15.0**	**120**	**1.53×10^4**	
144 mg	15.0	10	0.61×10^4	
144 mg	15.0	80	0.84×10^4	
144 mg	15.0	120	0.94×10^4	

Note: When the dose of hydrogels was 90 mg, the optimal solid-liquid ratio (3:500, g mL^{-1}) for removal of PAHs was achieved. Therefore, the dose of hydrogels used for the subsequent enzyme assembly experiments was also set as 90 mg.

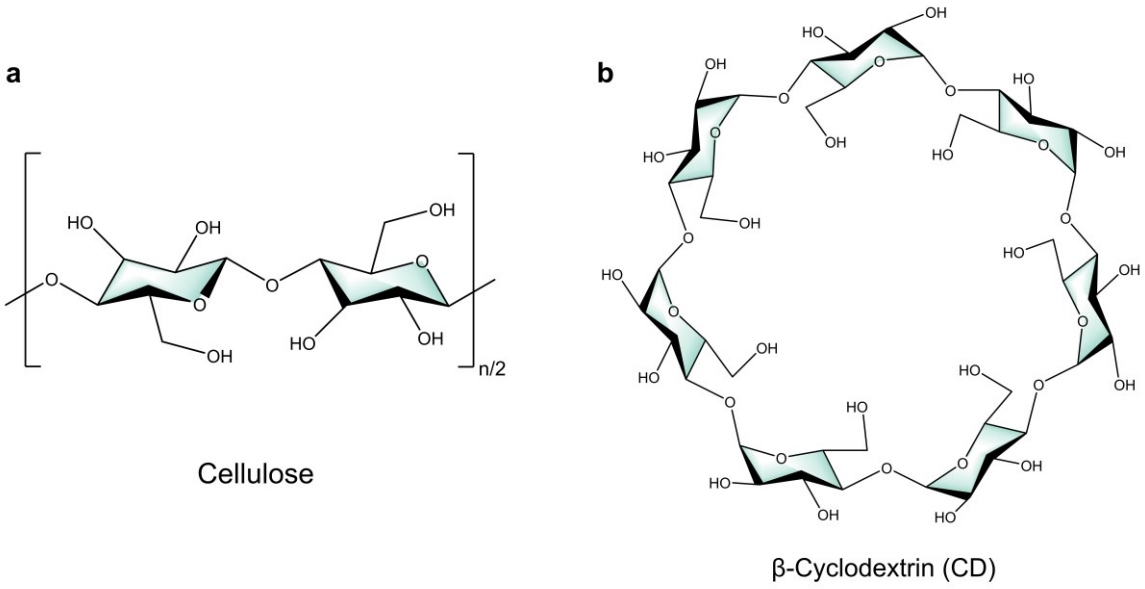

Supplementary Fig. 1. Structure of cellulose (a) and β-cyclodextrin (b).

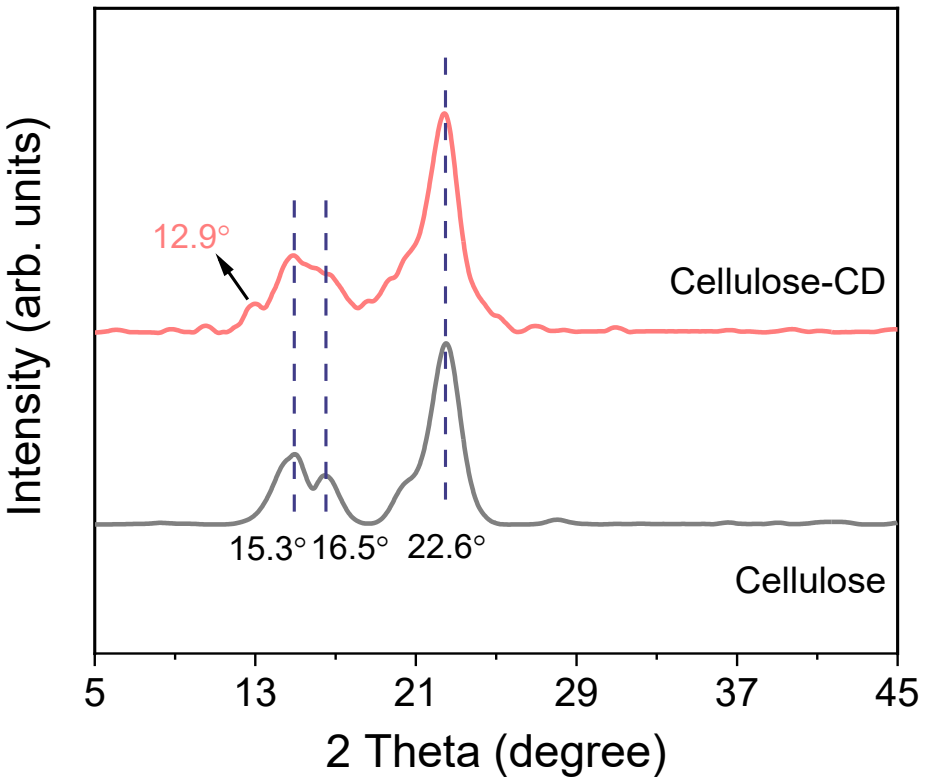

Supplementary Fig. 2. X-ray diffraction (XRD) patterns of Cellulose- and Cellulose-CD hydrogels. The XRD results showed the successful doping of CD on the cellulose backbone indicated by a new characteristic peak at 12.9 ° (belonging to CD) on XRD spectra of the Cellulose-CD hydrogels[127]. The characteristic peaks with 2θ angles at 15.3° ($1\bar{1}0$), 16.5° (110) and 22.6° (200) were contributed from cellulose[64,128].

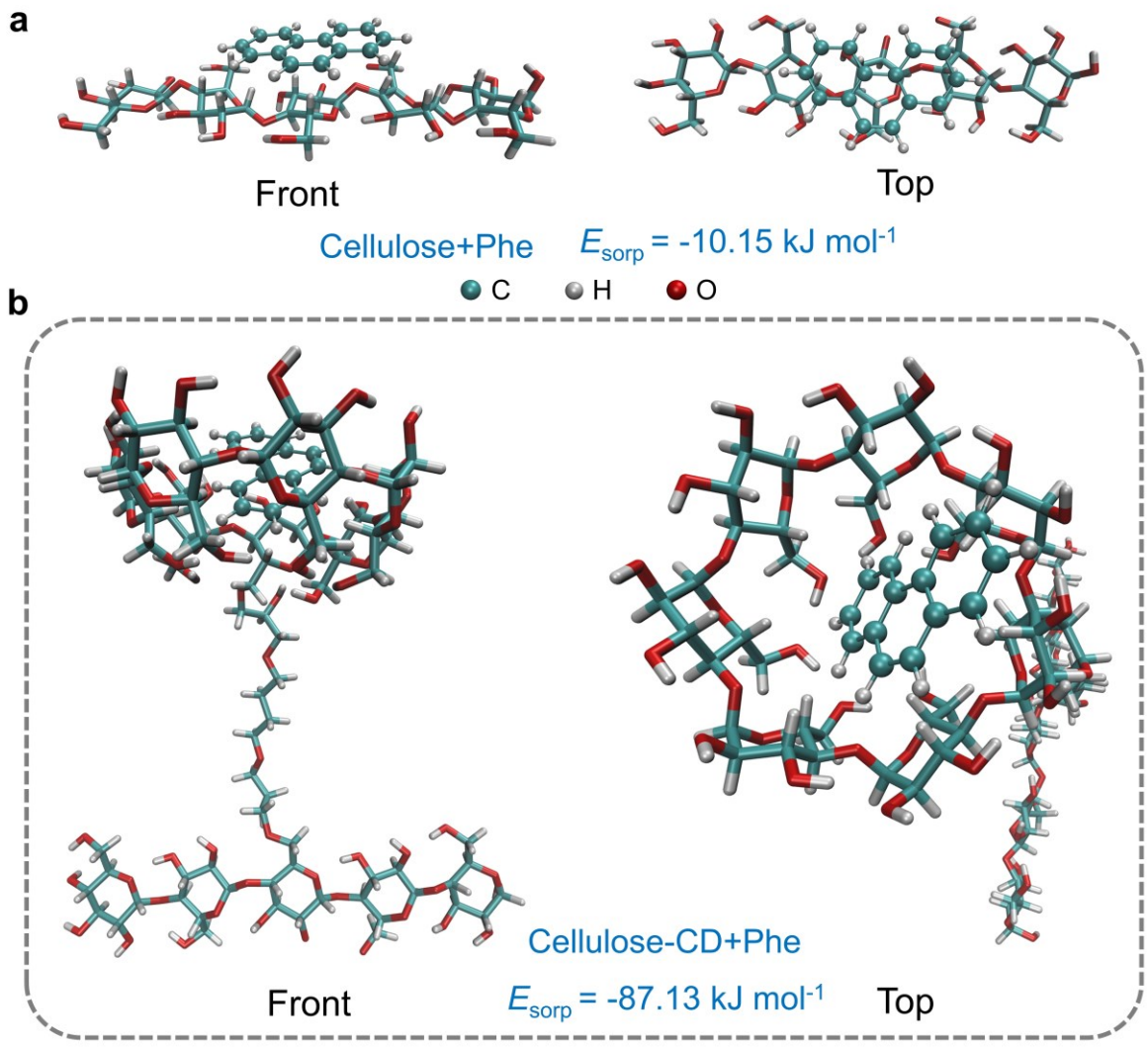

Supplementary Fig. 3. A diagram showing the simulated configurations from DFT calculation for sorption energy (E_{sorp}) of Phe on Cellulose (a) and Cellulose-CD (b) hydrogels. A higher sorption energy of Phe on Cellulose-CD hydrogels (-87.13 kJ mol^{-1}, host-guest interaction) than that on Cellulose hydrogels (-10.15 kJ mol^{-1}) indicates that CD doping to the cellulose backbone would promote Phe sorption on hydrogels. The model construction for Cellulose-CD hydrogels can be found in Supplementary Note 9.

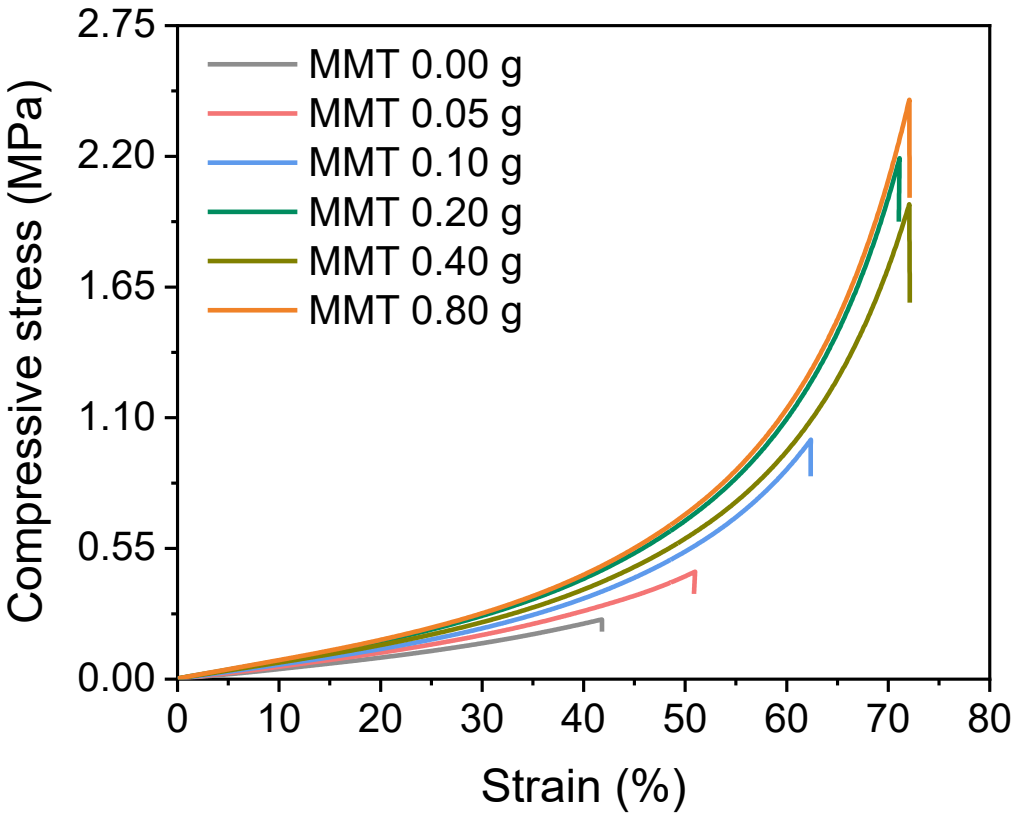

Supplementary Fig. 4. Compressive stress-strain curves of Cellulose-CD-MMT hydrogels with different amounts of MMT doped.

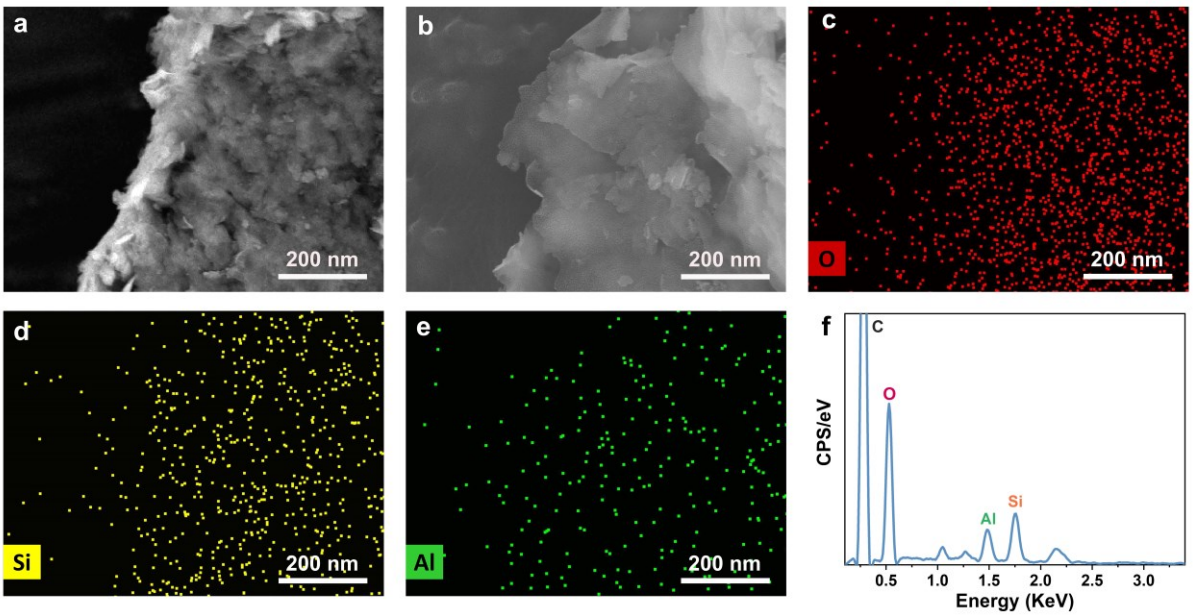

Supplementary Fig. 5. Structure characterization of MMT. a SEM image of the original MMT. **b** SEM image, **c-e** EDS mapping, and **f** Element distribution of MMT mechanically stripped. Compared to the MMT not mechanically stripped, the mechanically stripped MMT has an obvious layered structure, and O, Si, Al elements are uniformly distributed on its surface.

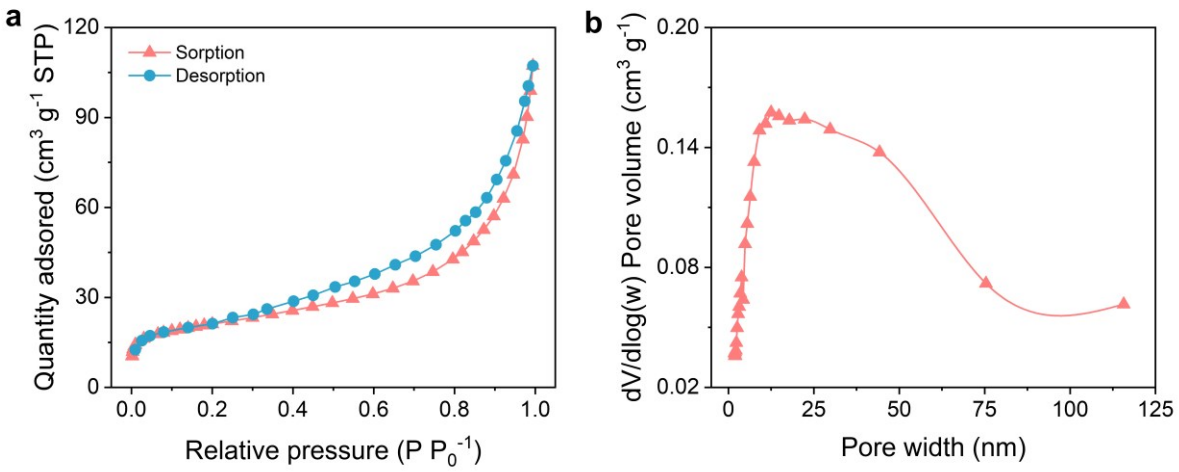

Supplementary Fig. 6. N_2 sorption-desorption isotherms at 77 K (a) and pore diameter distribution (b) of Cellulose-CD-MMT hydrogels. The N_2 sorption-desorption isotherms of Cellulose-CD-MMT hydrogels exhibit typical type IV curves (BET surface area: 56.32 m^2 g^{-1}), indicating the mesopore-rich structure in Cellulose-CD-MMT hydrogels, supported by pore size distribution (average pore diameter: 10.78 nm, pore volume: 0.261 cm^3 g^{-1}).

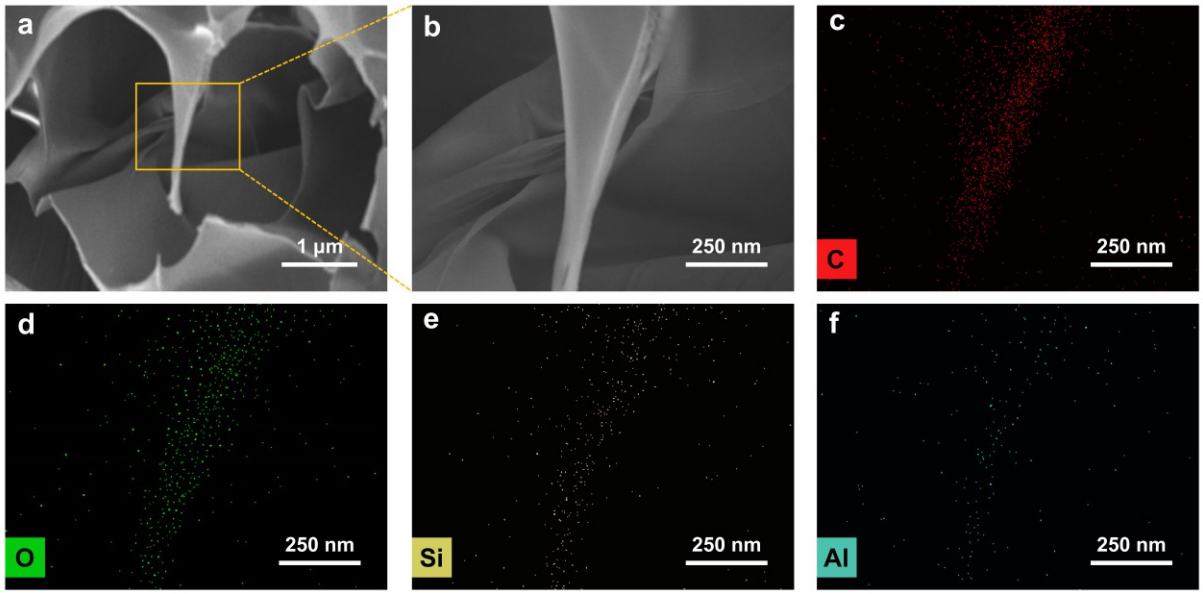

Supplementary Fig. 7. FESEM image of the Cellulose-CD-MMT hydrogels (a,b), and EDS mappings of C (c), O (d), Si (e), and Al (f) on the Cellulose-CD-MMT hydrogels. FESEM-EDS images of the Cellulose-CD-MMT hydrogels reveal a well-defined 3-dimensional porous network with homogeneous distribution of C, O, Si, and Al on the surface, indicating a uniform entanglement between MMT and cellulose or CD.

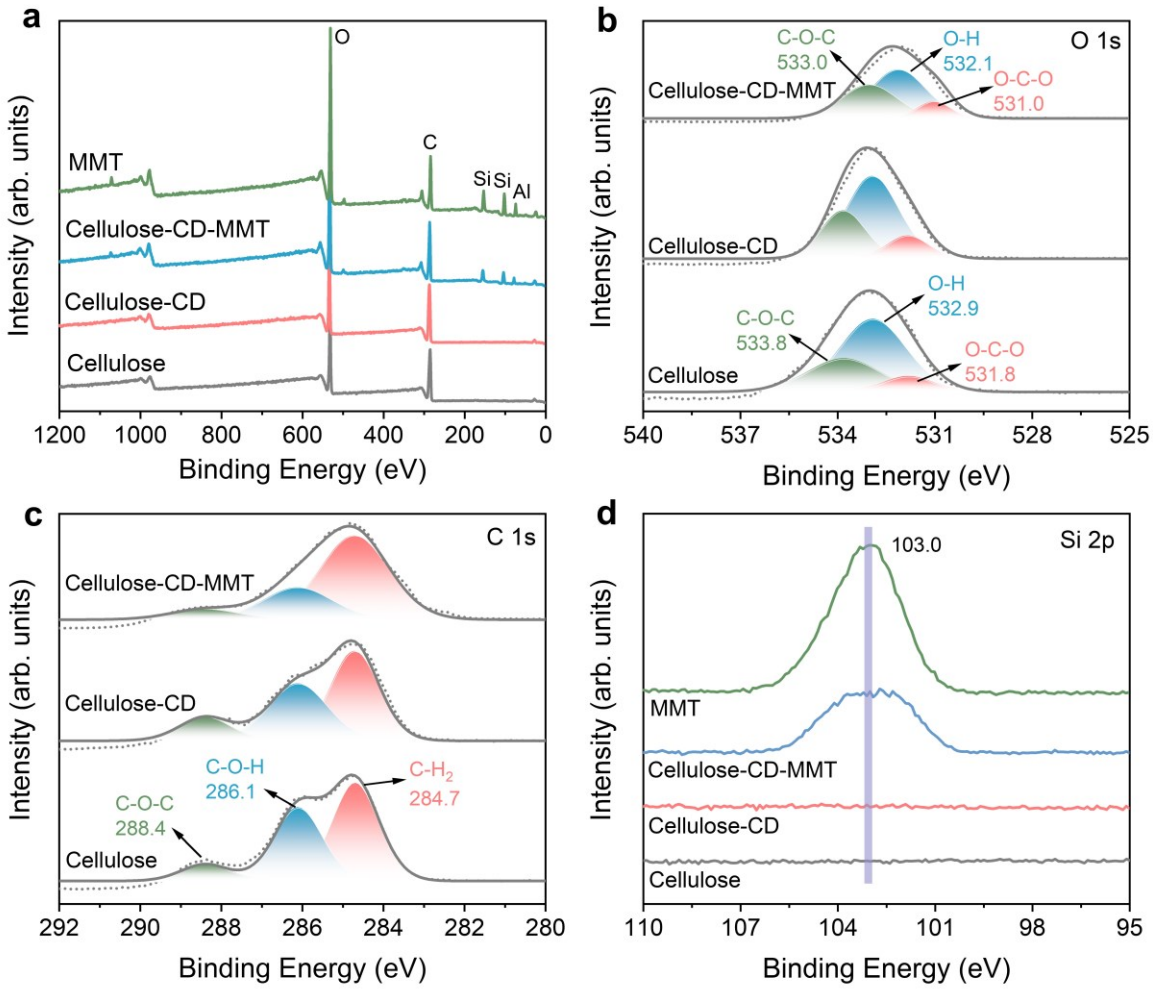

Supplementary Fig. 8. XPS spectra of Cellulose-, Cellulose-CD-, and Cellulose-CD-MMT hydrogels, and MMT. a Fully-scanned survey XPS spectra from 0 to 1200 eV. **b-d** High-resolution O 1s, C 1s and Si 2p spectra of these materials.

Note: After doping MMT on Cellulose-CD hydrogels, distinct peaks corresponding to Si and Al contributed from MMT are observed (Supplementary Fig. 8a), indicating the successful doping of MMT. The binding energies for C-O-C, O-H, and O-C-O groups on the O 1s XPS spectra of Cellulose hydrogels are at 533.8, 532.9, and 531.8 eV, respectively (Supplementary Fig. 8b)[129-132]. As for Cellulose-CD-MMT hydrogels, the binding energies for C-O-C, O-H, and O-C-O groups on their O 1s spectra shift down by 0.8 eV compared to those on the Cellulose and Cellulose-CD hydrogels due to disruption of the H-bonds of cellulose caused by MMT doping[64]. The peaks at 288.4, 286.1, and 284.7 eV on the C 1s spectra of all hydrogels corresponded to C-O-C, C-O-H, and C-H_2 groups (Supplementary Fig. 8c), respectively[129].

Notably, the peak intensity for C-O-H group on the XPS spectra of Cellulose-CD-MMT hydrogels significantly decreased relative to that on the spectra of Cellulose- and Cellulose-CD hydrogels, indicating the disruption of H-bonds of cellulose[133], which is consistent with the results from the O 1s XPS spectra. The binding energy position of Si 2p on the XPS spectra of Cellulose-CD-MMT hydrogels and MMT was identical (103.0 eV)[134,135], suggesting that disruption of H-bonds in cellulose resulting from MMT doping is unrelated to Si (Supplementary Fig. 8d). These findings are in line with the FTIR, XRD, and Al 2p XPS results.

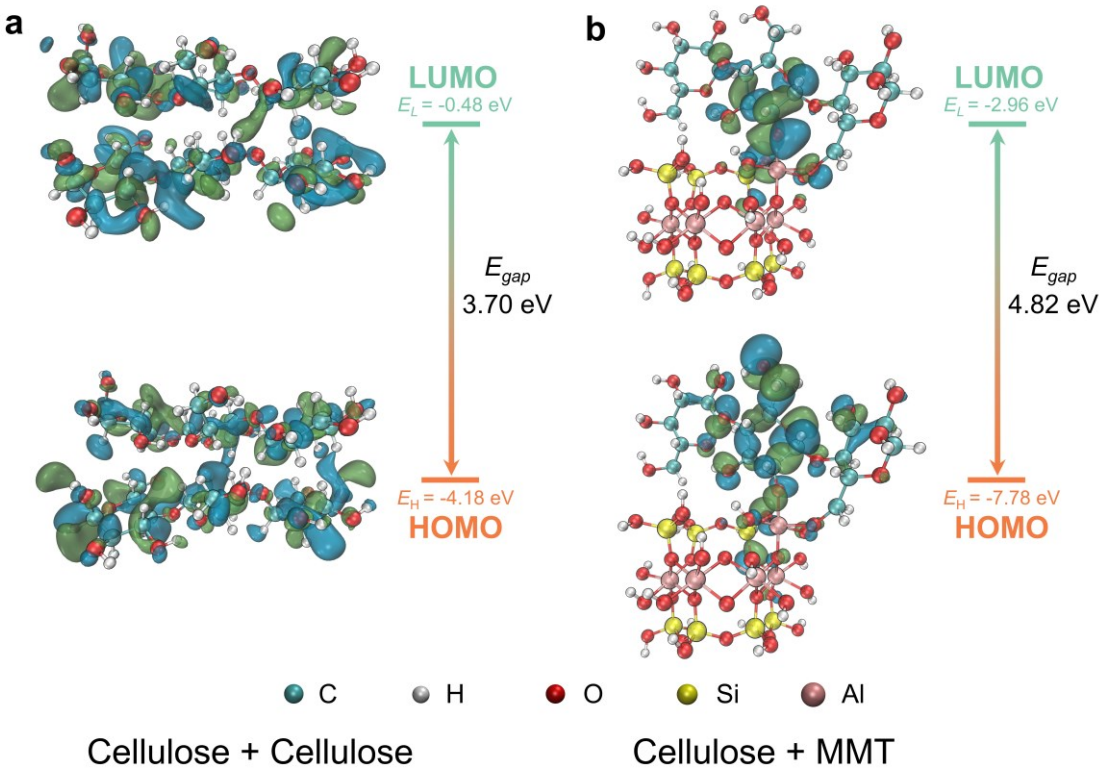

Supplementary Fig. 9. The HOMO and LUMO of cellulose-cellulose and cellulose-MMT. **a** and **b** the energy gap values ($E_{gap} = E_{LUMO} - E_{HOMO}$, Supplementary Note 10) of celluloses-cellulose and cellulose-MMT, respectively. A greater E_{gap} value means higher molecular stability and lower reactivity in chemical reactions, and the coordination (C-O-Al bonds, AlO_6) between cellulose and MMT is more stable than the H-bonds in cellulose.

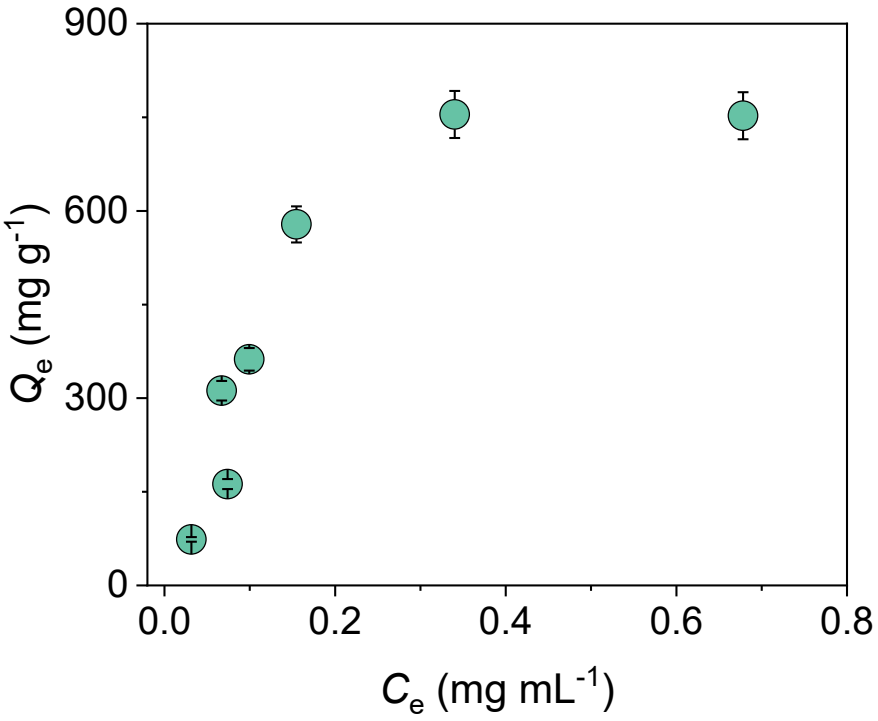

Supplementary Fig. 10. The sorption isotherms of laccase on Cellulose-CD-MMT hydrogels. Data are presented as mean ± S.D. from three replicates (n = 3).

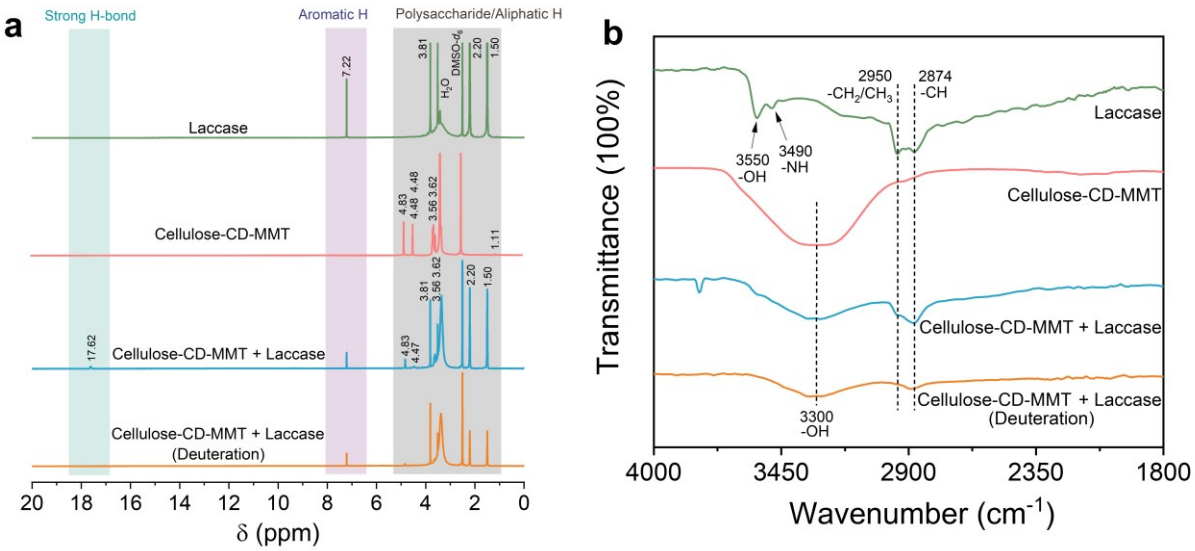

Supplementary Fig. 11. ^{1}H NMR (a) and FTIR (b) spectra of laccase before and after assembled (including deuteration) on Cellulose-CD-MMT hydrogels. The ^{1}H NMR characteristic peaks in the aliphatic H/aromatic H regions and the FTIR characteristic peaks (-CH_3 and -CH_2) derived from laccase were detected from the laccase-assembled hydrogels (Supplementary Table 3)[81,83], indicating successful laccase assembly. Specifically, two characteristic peaks including a peak at 2950 cm^{-1} and a shoulder at 2874 cm^{-1} were detected from FTIR spectra of the laccase-assembled Cellulose-CD-MMT hydrogels. They were contributed from stretching vibration of -CH_3 and -CH_2 groups on the laccase, respectively (Supplementary Fig. 11a)[136,137]. A peak at 7.22 ppm along with multiple peaks at 1.50, 2.20, and 3.81 ppm on ^{1}H NMR spectra of the laccase-assembled Cellulose-CD-MMT hydrogels also indicated the assembled aromatic- and aliphatic H from laccase, respectively (Supplementary Fig. 11b and Supplementary Table 3)[81,83]. The peaks at 2.50 and 3.35 ppm belonging to DMSO-d_6 and H_2O[6], respectively, were observed from ^{1}H NMR spectra of all samples.

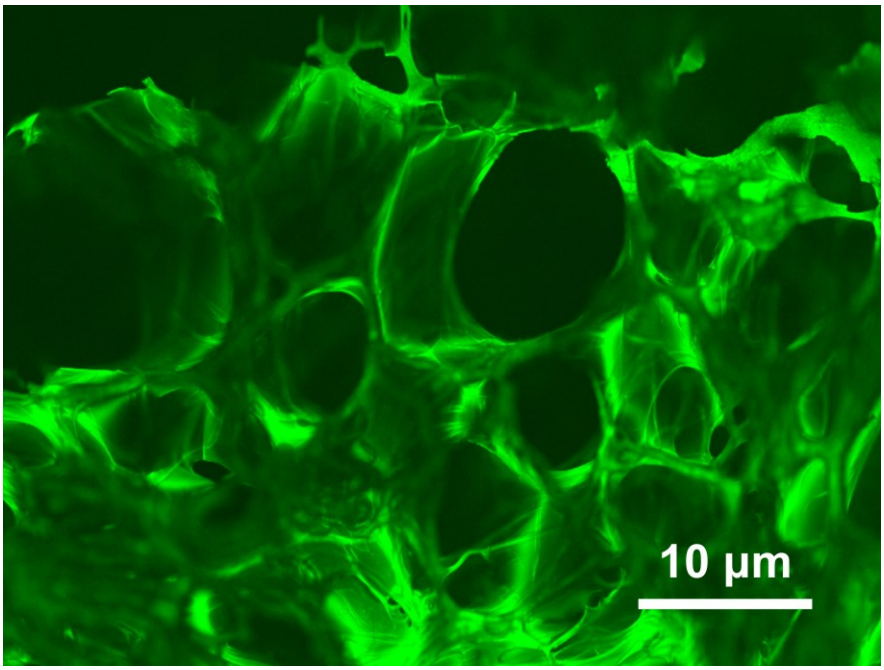

Supplementary Fig. 12. Confocal laser scanning micrograph of laccase-labeled with FITC assembly on Cellulose-CD-MMT hydrogels. The excitation and emission wavelengths are 488 and 525 nm, respectively. FITC: Fluorescein isothiocyanate. Laccase-labeled with green fluorescence (i.e., FITC) is evenly and abundantly distributed on Cellulose-CD-MMT hydrogels.

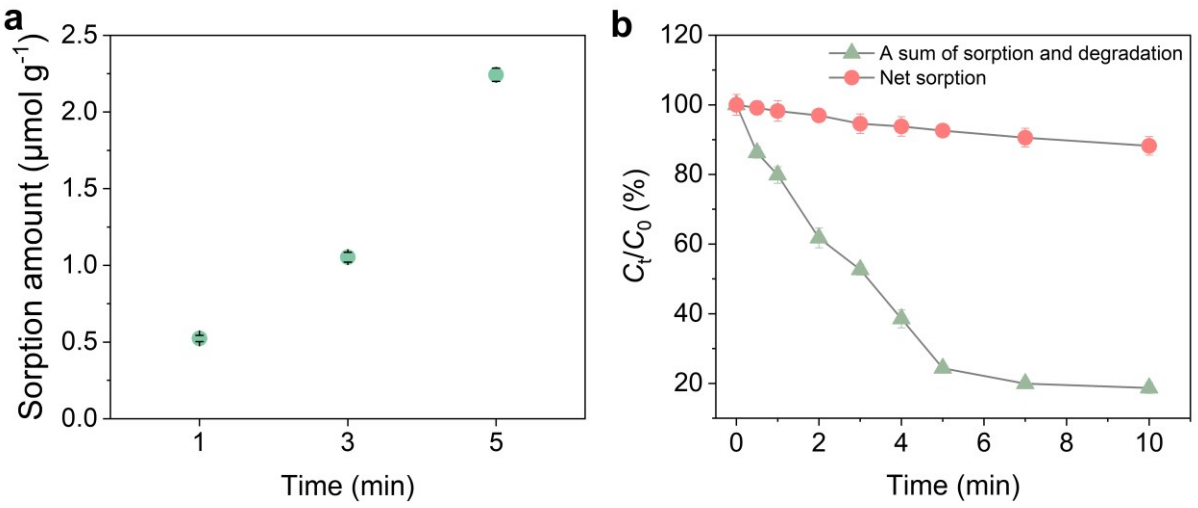

Supplementary Fig. 13. Sorption and oxidation rate-limiting steps of ABTS on laccase-assembled Cellulose-CD-MMT hydrogels. a Sorption of substrate ABTS by the inactivated laccase-assembled Cellulose-CD-MMT hydrogels. ABTS concentration: 1.0 mmol L^{-1}. **b** Elimination kinetics of ABTS by laccase-assembled Cellulose-CD-MMT hydrogels (a sum of sorption and oxidation) and inactivated laccase-assembled Cellulose-CD-MMT hydrogels (net sorption). ABTS concentration: 1.0 mmol. For (**a-b**), data are presented as mean ± S.D. from three replicates (n = 3).

Note: The sorption amount of ABTS on the laccase-assembled Cellulose-CD-MMT hydrogels can reach 2.24 μmol g^{-1} within 5 min (the determination time of laccase activity by the ABTS method), potentially leading to incomplete release of $ABTS^{\bullet+}$ (Supplementary Fig. 13a). This situation could potentially lead to an underestimation of the laccase activity. In addition, the elimination rate (49.85 μmol h^{-1}, a sum of sorption and oxidation) of ABTS by the laccase-assembled hydrogels in 5 min is far greater than its sorption rate (4.46 μmol h^{-1}) by the inactivated laccase-assembled hydrogels (Supplementary Fig. 13b). This phenomenon could result from substrate diffusion (or sorption/capture) serving as the rate-limiting step in enzymatic process, as ABTS sorption by CD could enhance substrate accessibility to the enzyme's active site and thus improve its activity. The observed sorption efficiency of approximately 10% resulted in a 40% increase in absolute enzymatic activity. This is reasonable, as it reflects not only an increase in substrate concentration but also enhanced mass transfer and substrate affinity during the sorption process. Since sorption, substrate binding,

and mass transfer are dynamic and simultaneous, they are difficult to completely separate. The enhanced substrate capture/affinity and mass transfer jointly overcame the limitation of substrate diffusion of free laccase. Moreover, the factors contributing to approximately 10% of sorption efficiency of ABTS could be the use of inactivated immobilized laccase in our experiments, where conformational changes due to inactivation may have obscured the true sorption sites on the laccase-assembled hydrogels. Sorption of ABTS by hydrogel is primarily achieved through the host-guest interaction between β-cyclodextrin and the compound[138-140].

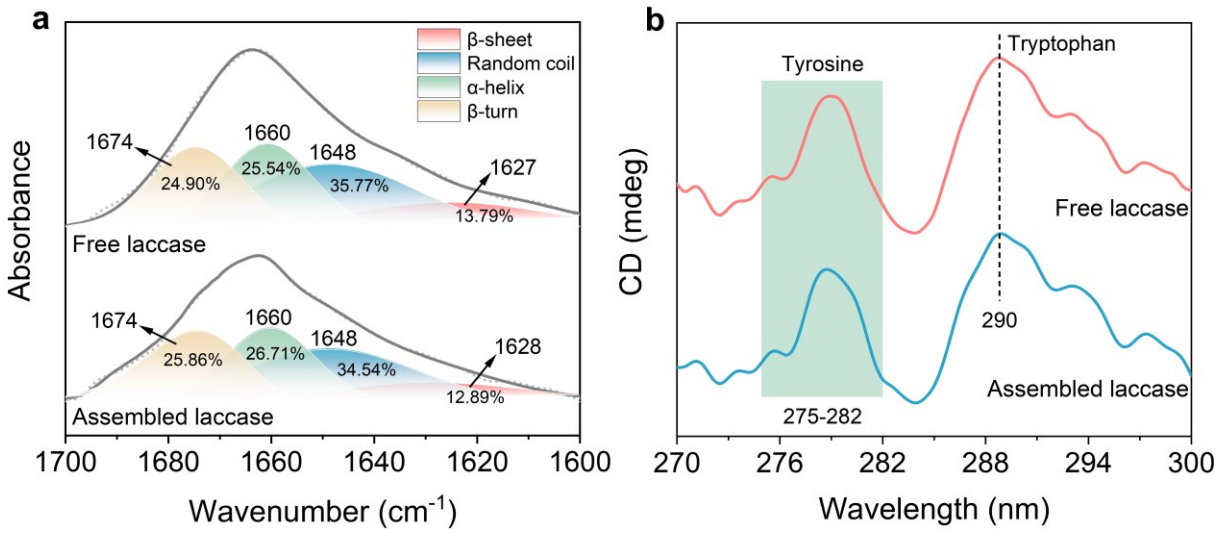

Supplementary Fig. 14. Protection of 3D conformation of laccase in laccase-assembled Cellulose-CD-MMT hydrogels. a FTIR spectra of free laccase and laccase-assembled Cellulose-CD-MMT hydrogels in the range of 1600-1700 cm^{-1}. **b** Near-UV circular dichroism spectra of free laccase and laccase-assembled Cellulose-CD-MMT hydrogels in the range of 270-300 nm.

Note: FTIR and near-UV circular dichroism spectra are commonly employed to characterize enzyme conformation[141-143]. The FTIR spectra reveal that free laccase consists of 13.79% β-sheet, 35.77% random coil, 25.54% α-helix, and 24.90% β-turn structures. In comparison, the assembled laccase comprises 12.89% β-sheet, 34.54% random coil, 26.71% α-helix, and 25.86% β-turn structures. These results indicate no significant differences in the above conformation (β-sheet, random coil, α-helix, and β-turn) between the free- and assembled laccase. Additionally, positions of the peaks on the near-UV circular dichroism spectra corresponding to tyrosine (275-282 nm) and tryptophan (290 nm) of the assembled laccase do not shift significantly compared to those of free laccase. These findings demonstrate that the 3-dimensional conformation of laccase is well-preserved upon its assembly on Cellulose-CD-MMT hydrogels.

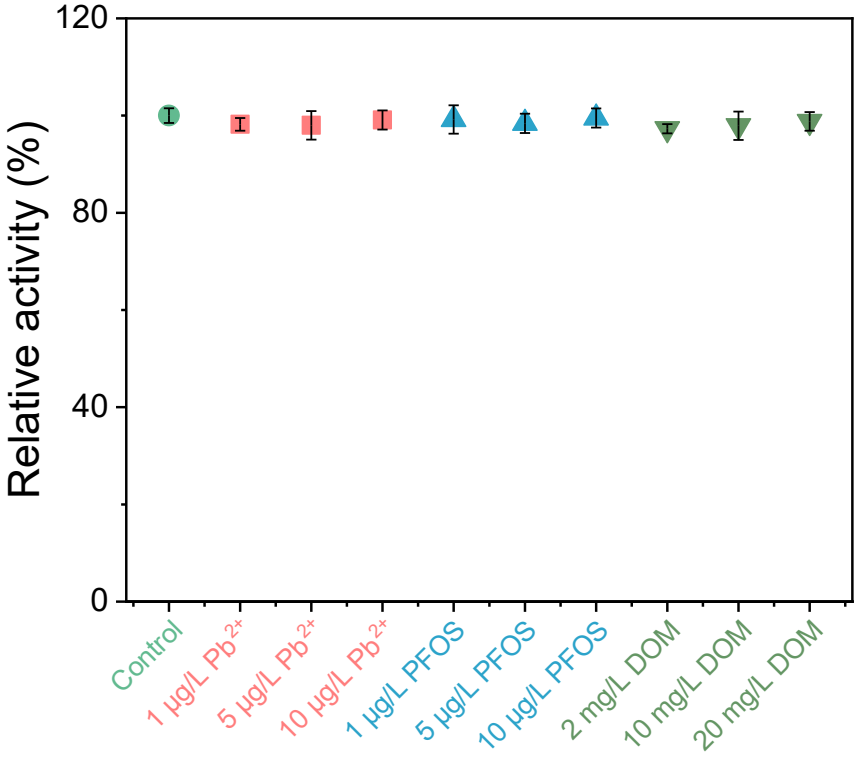

Supplementary Fig. 15. Effects of the coexisting heavy metals (Pb^{2+}, 1-10 μg L^{-1}), organic contaminants (perfluorooctanesulfonic acid, PFOS, 1-10 μg L^{-1}) and dissolved organic matter (DOM, 2-20 mg L^{-1}) (humic acid) on enzymatic activity of the laccase-assembled Cellulose-CD-MMT hydrogels. Data are presented as mean ± S.D. from three replicates (n = 3). Pb^{2+}, PFOS and humic acid were chosen as representatives of heavy metals, organic contaminant and DOM, respectively, which are widely detected in the water environment, and their experimental concentrations were set according to that in the real water[144-148]. These substances do not significantly reduce enzymatic activity of the laccase-assembled hydrogels, mainly due to the following interacting factors and mechanisms: (1) The Cellulose-CD-MMT hydrogels provide a physical barrier around the laccase, reducing the probability of direct interaction between these interfering substances and the laccase's active site; this shielding effect ensures the enzyme retains its catalytic activity in the complex environments; (2) The CAHB strategy stabilizes the enzyme's conformation, preventing structural distortion or denaturation caused by these interfering substances; this structural integrity is crucial for maintaining enzymatic activity; (3) These interfering substances can be effectively isolated by the unique components of the hydrogel system, such as the host-guest interactions between the interfering substances and CD or interactions with cellulose hydroxyl groups (e.g., Pb^{2+} chelated), reducing their availability to interact with and inhibit the enzyme.

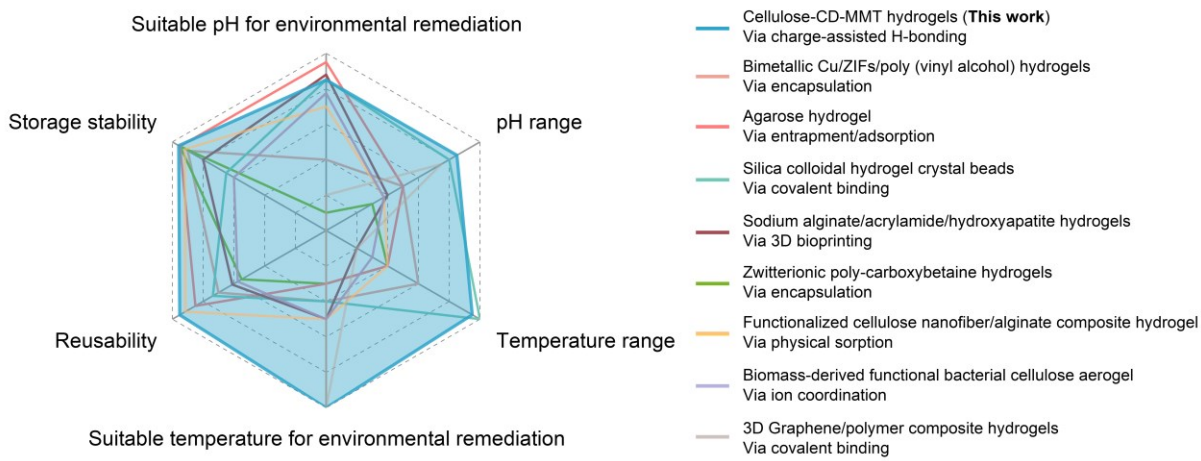

Supplementary Fig. 16. A comprehensive comparison between assembly strategy of laccase on Cellulose-CD-MMT hydrogels in this work and the immobilization methods of laccase on various hydrogel carriers in previous reports in terms of operational range of pH and temperature (maintaining in excess of 80% of enzymatic activity), suitable pH and temperature for environmental remediation, storage stability, and reusability.

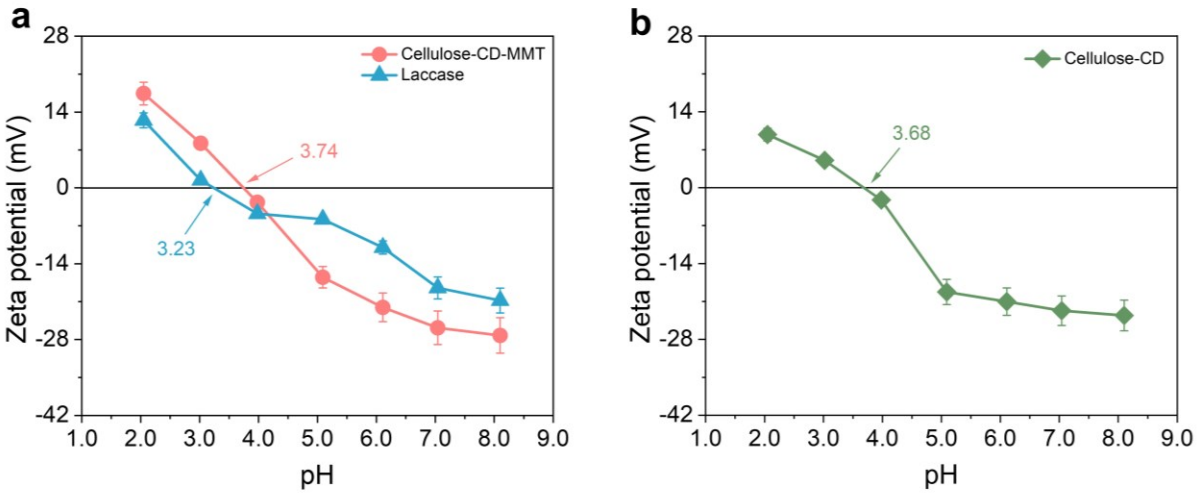

Supplementary Fig. 17. The point of zero charge (PZC) of Cellulose-CD-MMT hydrogels, laccase (a) and Cellulose-CD hydrogels (b). For (a-b), data are presented as mean ± S.D. from three replicates (n = 3). The difference in PZC values ($|\Delta PZC|$ = 0.51) between Cellulose-CD-MMT hydrogels and laccase is less than 5.0, providing a foundation for CAHB formation. The MMT doping did not significantly change PZC value of Cellulose-CD hydrogels.

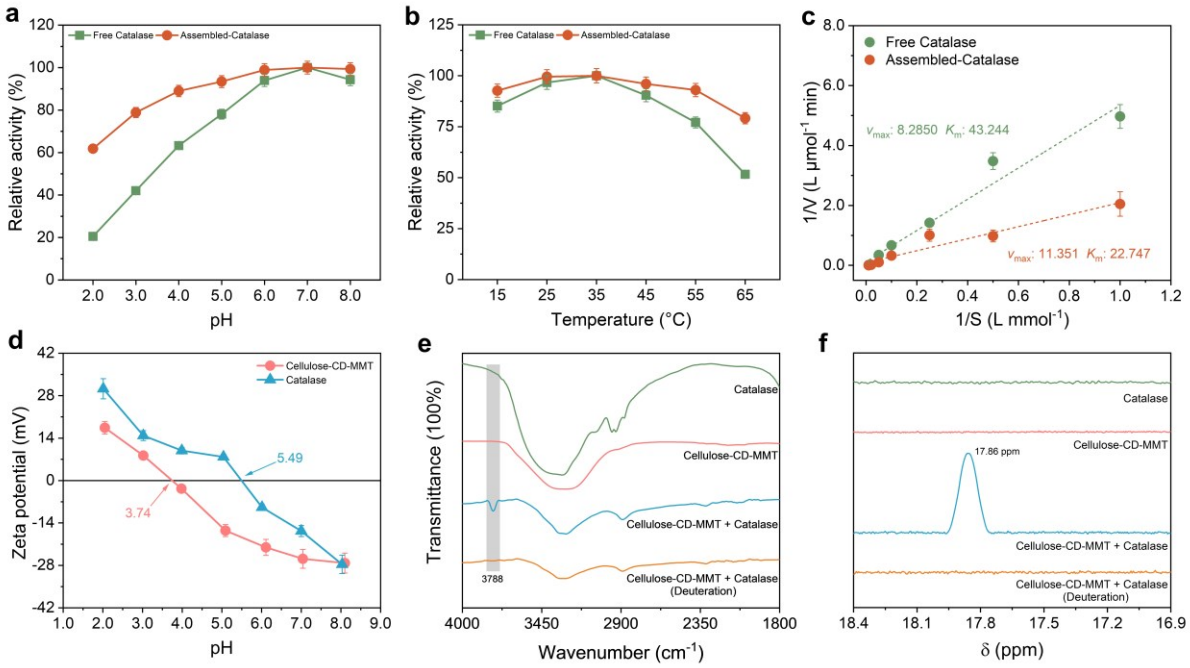

Supplementary Fig. 18. CAHB formation between catalase and Cellulose-CD-MMT hydrogels, performance level and enzymatic activity stability of the assembled catalase. a and **b** The pH and temperature stability of free- and assembled catalase. Catalase activity (1.0 U) is defined as the amount of catalase required to catalyze 1.0 μmol substrate (H_2O_2) per minute[149]. **c** The Lineweaver-Burk plots of free- and assembled catalase. The kinetics studies of free- and assembled catalase were conducted in the H_2O_2 concentration range of 1.0-100 mmol L^{-1}. The kinetics parameters were obtained by measuring the initial reaction rate of the catalase with H_2O_2. **d** The PZC of Cellulose-CD-MMT hydrogels and catalase. **e** FTIR spectra of catalase before and after assembled (including deuteration) on hydrogels. **f** ^{1}H NMR spectra of catalase before and after assembled (including deuteration) on hydrogels. For (**a-d**), data are presented as mean ± S.D. from three replicates (n = 3).

Note: Catalase has been widely utilized in textile industry, cosmetic therapy, etc[149,150]. The assembled catalase exhibited a broader operational range (pH 4-8, 15-55 °C) compared to free catalase (pH 6-8, 15-45 °C) in terms of sustaining more than 80% of enzymatic activity. Compared with the kinetics parameters of free-catalase (K_m: 43.244, v_{max}: 8.2580), the assembled catalase showed a lower K_m value (22.747) and a higher v_{max} value (11.351), indicating that the assembled catalase has a higher affinity for substrate (H_2O_2) and reaction rate compared to the free catalase. The difference in PZC values (|ΔPZC| = 1.75) between

Cellulose-CD-MMT hydrogels and catalase is less than 5.0. The new peaks appeared at 3788 cm^{-1} on FTIR spectra and 17.86 ppm on ^{1}H NMR spectra of catalase-assembled hydrogels, which indicated the formation of strong H-bonds (CAHB)[6,84,151]. Interestingly, the peaks belonging to CAHB vanished after the solvent (H_2O) was replaced with D_2O (deuteration). These results provide direct evidence for CAHB formation between catalase and Cellulose-CD-MMT hydrogels.

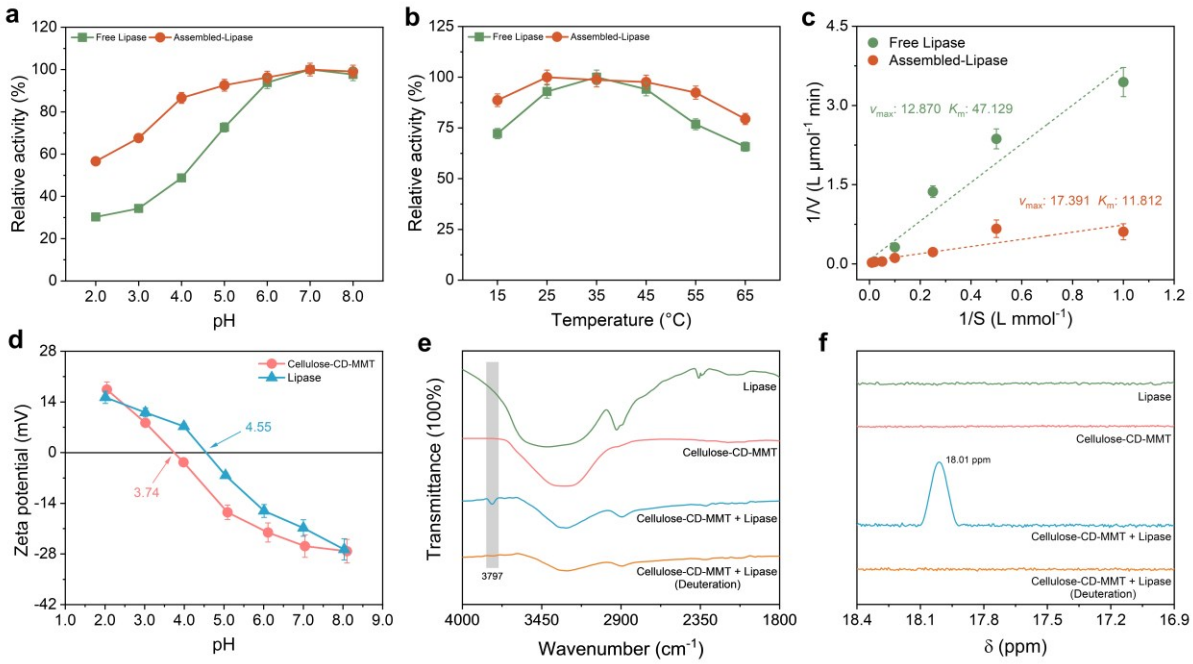

Supplementary Fig. 19. CAHB formation between lipase and Cellulose-CD-MMT hydrogels, performance level and enzymatic activity stability of the assembled lipase. a and **b** The pH and temperature stability of free- and assembled lipase. Lipase activity (1.0 U) is defined as the amount of lipase required to produce 1.0 μmol *p*-nitrophenol produced by catalyzing *p*-nitrophenylbutyrate per minute[152]. **c** The Lineweaver-Burk plots of free- and assembled lipase. The kinetics studies of free- and assembled lipase were conducted in the *p*-nitrophenylbutyrate concentration range of 1.0-100 mmol L^{-1}. The kinetics parameters were obtained by measuring the initial reaction rate of lipase with *p*-nitrophenylbutyrate. **d** The PZC of Cellulose-CD-MMT hydrogels and lipase. **e** FTIR spectra of lipase before and after assembled (including deuteration) on hydrogels. **f** ^{1}H NMR spectra of lipase before and after assembled (including deuteration) on hydrogels. For (**a-d**), data are presented as mean ± S.D. from three replicates (n = 3).

Note: Lipase has been widely utilized in plastic degradation, food manufacture, etc[152,153]. The assembled lipase exhibited a broader operational range (pH 4-8, 15-55 °C) compared to the free lipase (pH 6-8, 25-45 °C) in terms of sustaining more than 80% enzymatic activity. Compared to the kinetics parameters of free lipase (K_m: 47.129, v_{max}: 12.870), the assembled lipase showed a lower K_m value (11.812) and a higher v_{max} value (17.391), indicating that the assembled lipase has a higher affinity for the substrate (*p*-nitrophenylbutyrate) and reaction rate compared to the free lipase. The difference in PZC values (|ΔPZC| = 0.81) between

hydrogels and lipase is less than 5.0. New peaks appeared at 3797 cm^{-1} on the FTIR spectra and at 18.01 ppm on the ^{1}H NMR spectra of lipase-assembled hydrogels, indicating the formation of CAHB[6,84,151]. Interestingly, the peaks belonging to CAHB disappeared after the solvent (H_2O) was replaced with D_2O (deuteration). These results provide direct evidence for CAHB formation between lipase and Cellulose-CD-MMT hydrogels.

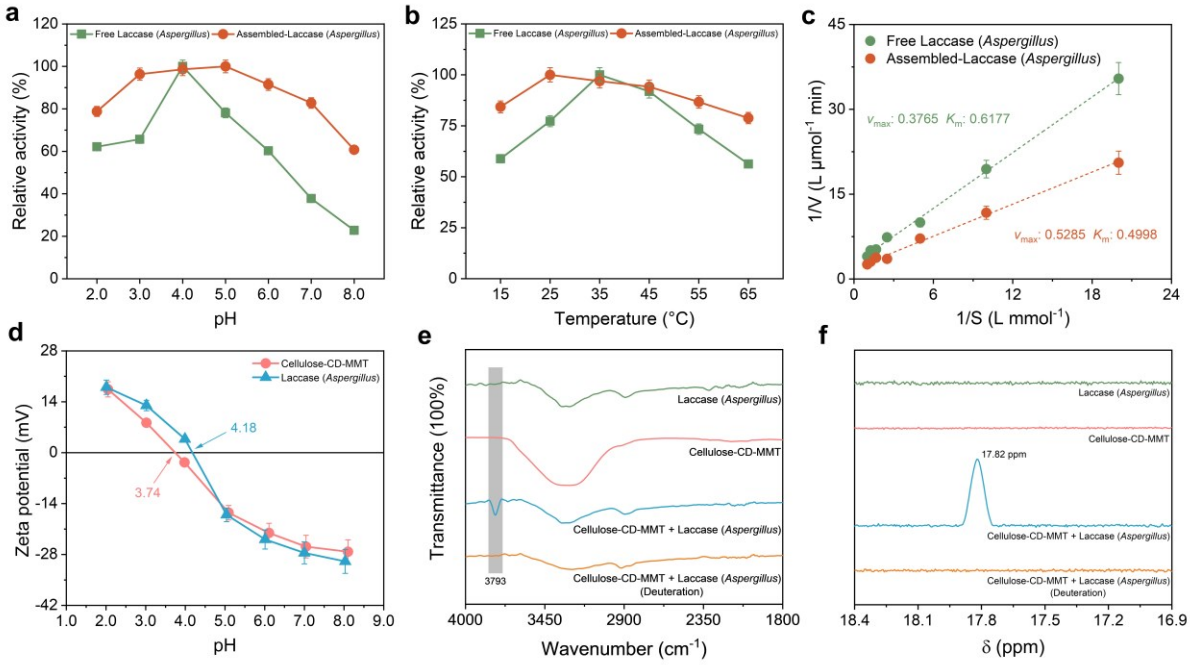

Supplementary Fig. 20. CAHB formation between laccase (from *Aspergillus*) and Cellulose-CD-MMT hydrogels, performance level and enzymatic activity stability of the assembled laccase (from *Aspergillus*). a and **b** The pH and temperature stability of free- and assembled laccase (from *Aspergillus*). **c** The Lineweaver-Burk plots of free- and assembled laccase. **d** The PZC of Cellulose-CD-MMT hydrogels and laccase. **e** FTIR spectra of laccase before and after assembled (including deuteration) on hydrogels. **f** ^{1}H NMR spectra of laccase before and after assembled (including deuteration) on hydrogels. For (**a-d**), data are presented as mean ± S.D. from three replicates (n = 3).

Note: The kinetics and activity determination procedures for laccase (from *Aspergillus*) are consistent with those for laccase (from *Trametes versicolor*) in this study. Assembled laccase (from *Aspergillus*) also exhibited a broader operational range (pH 2-6, 15-55 °C) compared to the free laccase (from *Aspergillus*) (pH 4, 35-45 °C) in terms of sustaining more than 80% of enzymatic activity. Compared to the kinetics parameters of free laccase (from *Aspergillus*, K_m: 0.6177, v_{max}: 0.3765), the assembled laccase (from *Aspergillus*) showed a lower K_m value (0.4998) and a higher v_{max} value (0.5285). The difference in PZC values (|ΔPZC| = 0.44) between hydrogels and laccase (from *Aspergillus*) was less than 5.0. The new peaks appeared at 3793 cm^{-1} on FTIR spectra and at 17.82 ppm on ^{1}H NMR spectra of laccase-assembled hydrogels, indicating the formation of CAHB[6,84,151]. Interestingly, the peaks belonging to CAHB were gone after the solvent (H_2O) was replaced with D_2O (deuteration). These results provide direct evidence for CAHB formation between laccase (from *Aspergillus*) and Cellulose-CD-MMT hydrogels.

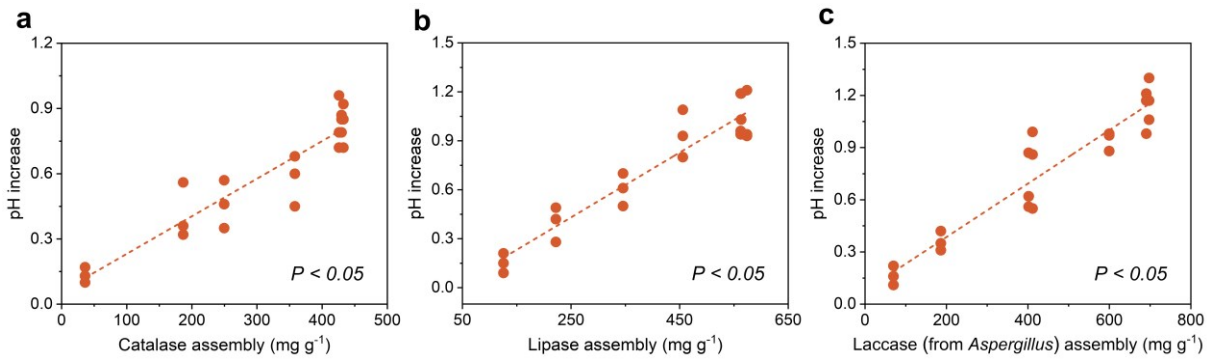

Supplementary Fig. 21. The relationship between assembled amount of catalase (a), lipase (b) and laccase (from *Aspergillus*, c) on Cellulose-CD-MMT hydrogels and solution pH. A positive correlation exists between the pH change and the assembled amount of these enzymes, aligning with the assembly of laccase (from *Trametes versicolor*) and potentially indicating CAHB formation.

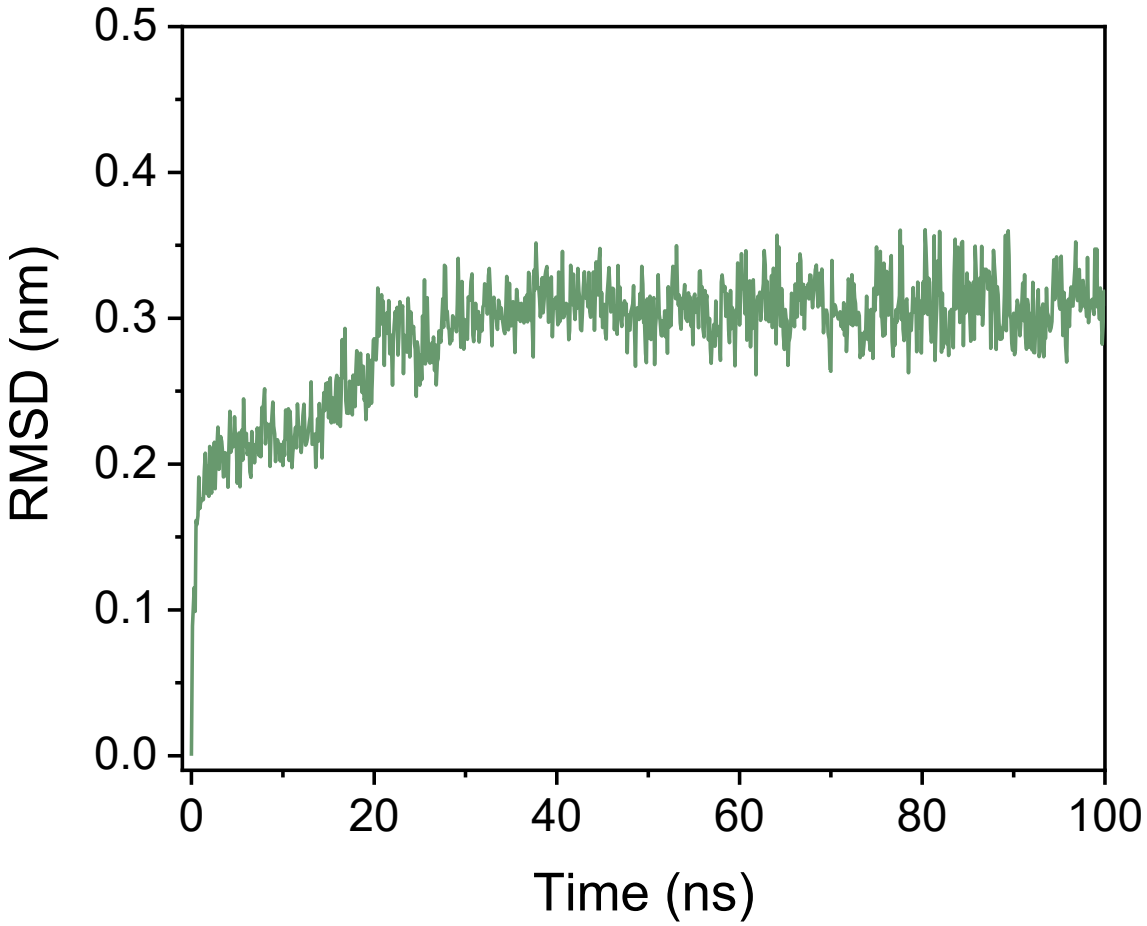

Supplementary Fig. 22. The root-mean-square deviation (RMSD) values of the system containing Cellulose-CD-MMT hydrogels and laccase. The fluctuation of RMSD after 50 ns is very low, indicating that the system has reached equilibrium[154]. The MD simulation was conducted for 100 ns, which is sufficient to ensure the interaction between laccase and Cellulose-CD-MMT hydrogels has reached equilibrium.

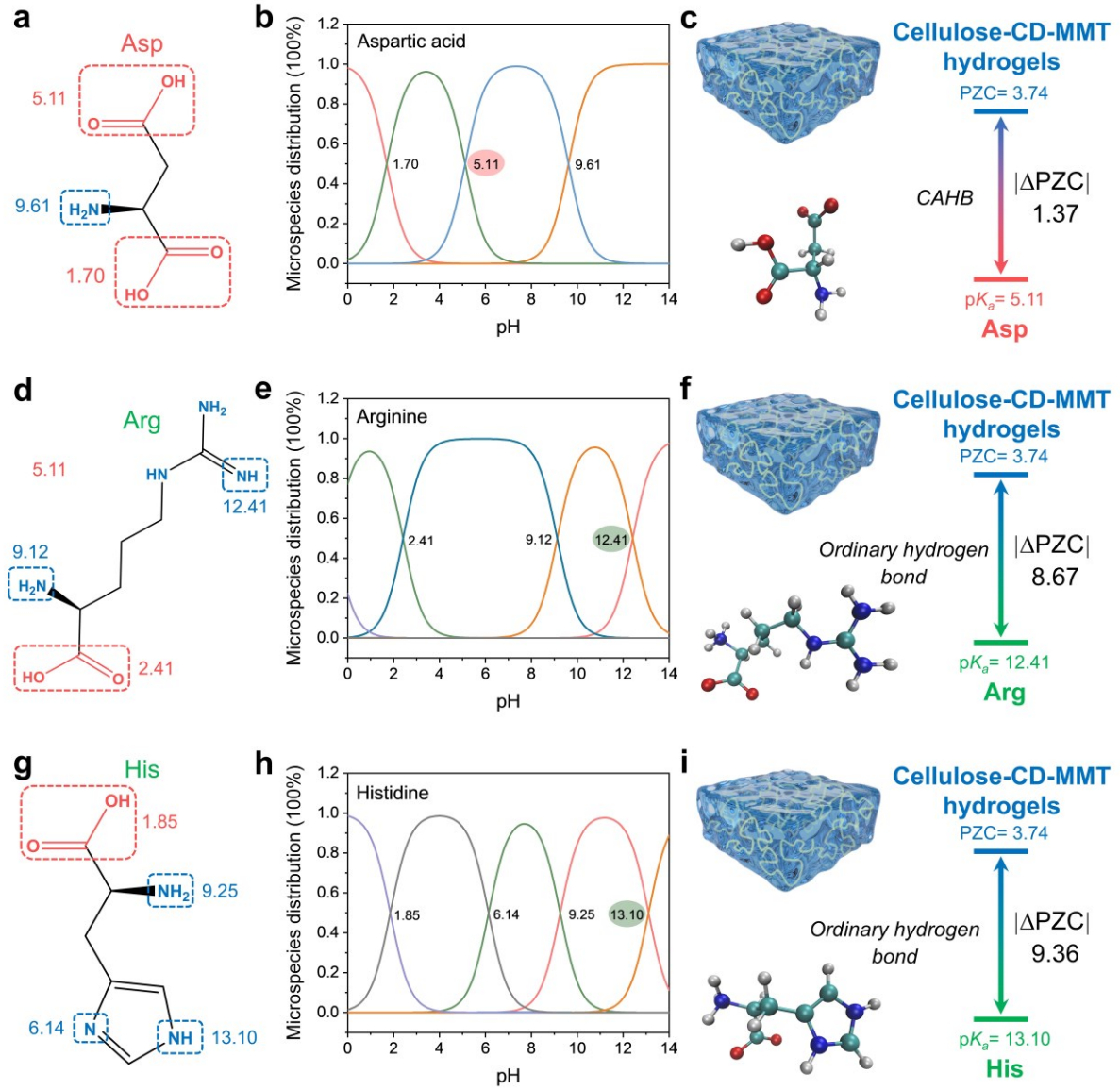

Supplementary Fig. 23. Diagrams showing formation of various H-bonds between Cellulose-CD-MMT hydrogels and functional groups (–COOH, –NH) on various amino acids on laccase surface via MD simulation. a, d and **g** Chemical structures of Asp, Arg and His, respectively. **b, e** and **h** Speciation distribution of Asp, Arg and His as a function of pH values, respectively. The data were obtained from website of http://www.chemicalize.org/ (accessed Aug 12, 2023). **c, f** and **i** The |ΔPZC| values between Cellulose-CD-MMT hydrogels and functional groups (–COOH, –NH) on Asp, Arg and His, respectively (Supplementary Note 1). MD simulation shows that the hydrogels formed CAHB (|ΔPZC| = 1.37) with –COOH group on Asp (at pK_a 5.11). The Cellulose-CD-MMT hydrogels formed ordinary H-bonds with –NH group on Arg (at pK_a 12.41, |ΔPZC| = 8.67) or His (at pK_a 13.10, |ΔPZC| = 9.36).

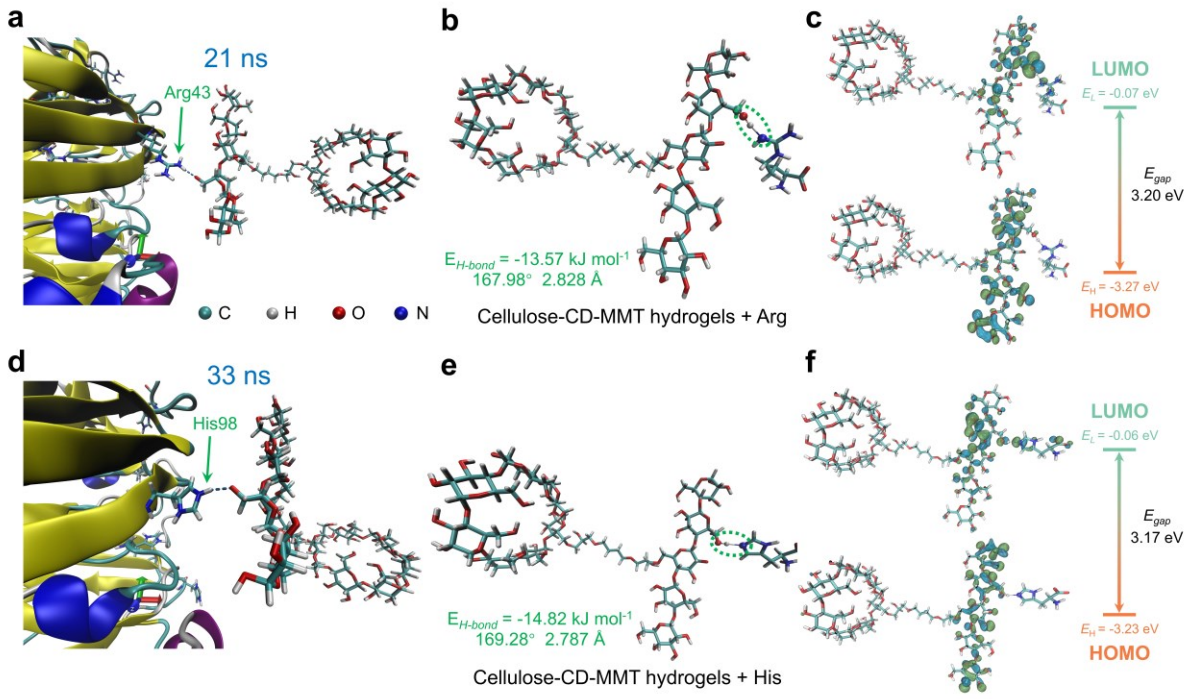

Supplementary Fig. 24. The strength and stability of ordinary H-bond configurations obtained by MD simulation. a and **d** Ordinary H-bond configurations between Cellulose-CD-MMT hydrogels and Arg43 (21 ns) or His98 (33 ns) obtained by MD simulation. **b** and **d** Strength of the ordinary H-bond formed between Cellulose-CD-MMT hydrogels and Arg or His. **c** and **f** Stability of the ordinary H-bond formed between Cellulose-CD-MMT hydrogels and Arg or His.

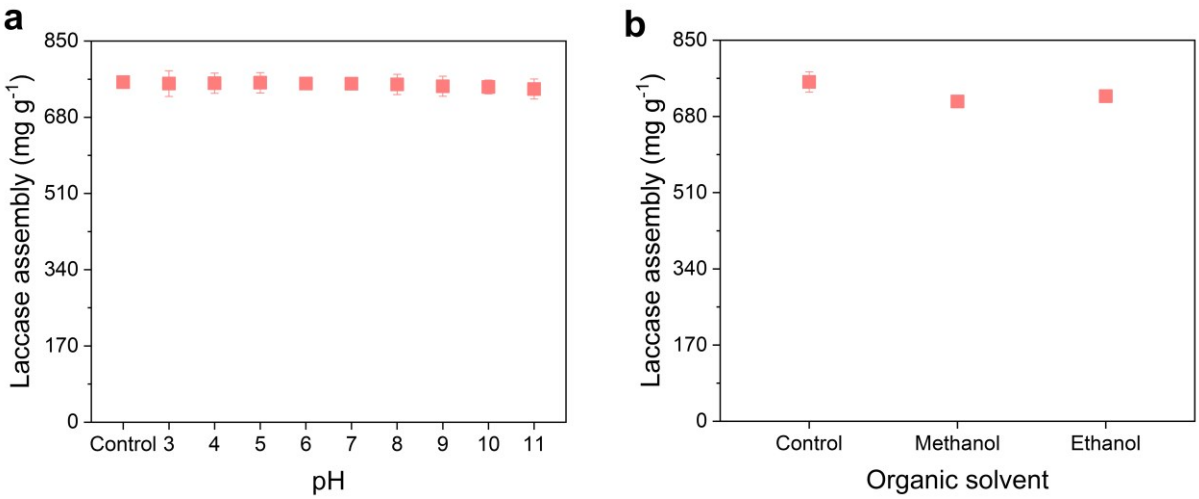

Supplementary Fig. 25. Influence of pH (3-11, a) and common organic solvents (methanol and ethanol, b) on assembly amount of laccase on Cellulose-CD-MMT hydrogels via CAHB. Time: 48 h. For (**a-b**), data are presented as mean ± S.D. from three replicates (n = 3). It appears that the laccase-assembled Cellulose-CD-MMT hydrogels exposed to solution at different pHs (≤ 2.0%) or organic solvents (≤ 5.7%**)** for 48 h did not result in a significant reduction in amount of laccase assembly, indicating stable assembly of laccase on hydrogels via CAHB.

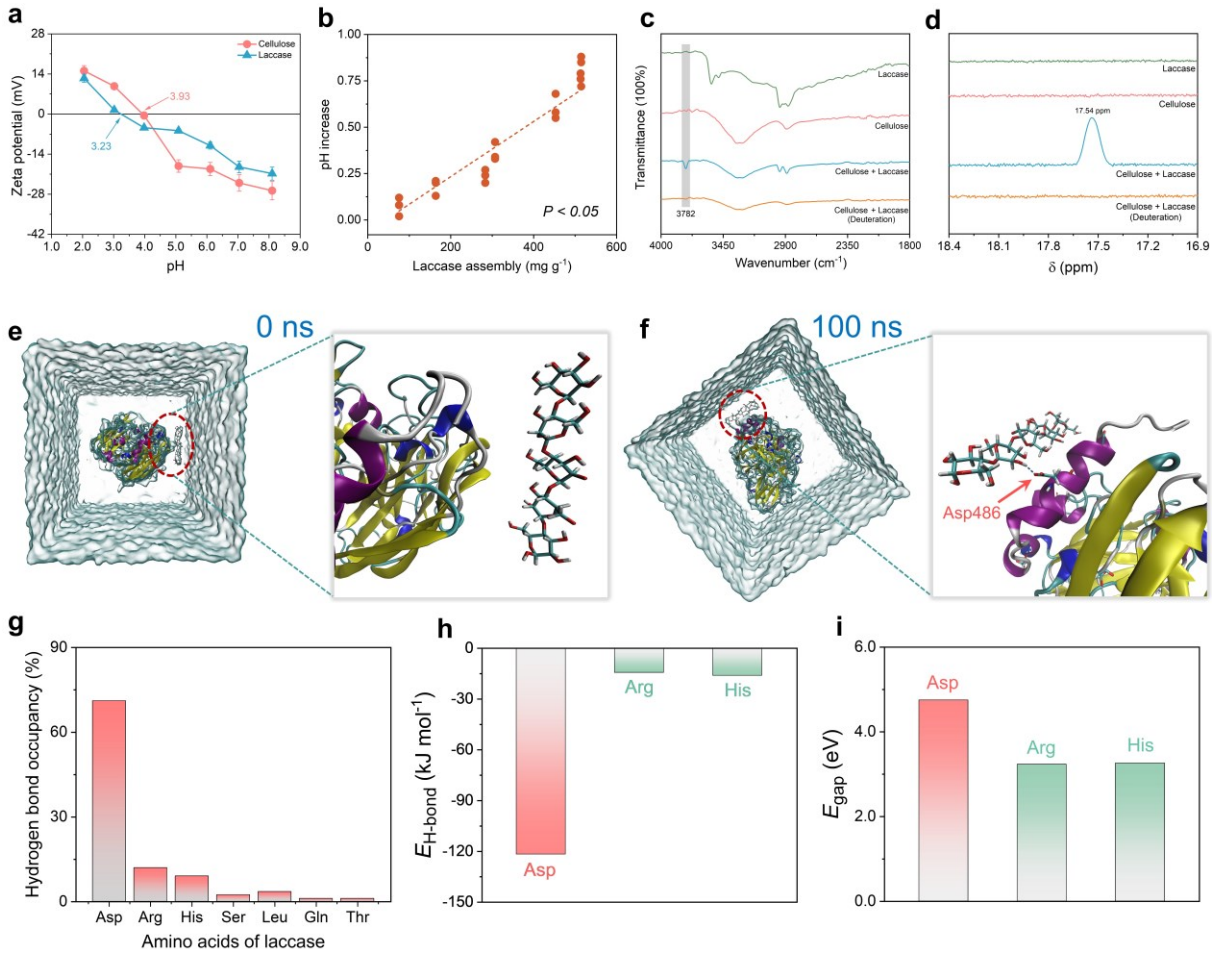

Supplementary Fig. 26. Assembly mechanism of laccase on Cellulose hydrogels by CAHB. **a** The PZC of Cellulose hydrogels and laccase. **b** The relationship between assembled amount of laccase on Cellulose hydrogels and solution pH. **c, d** FTIR (**c**) and ^{1}H NMR (**d**) spectra of laccase before and after assembly (including deuteration) on Cellulose hydrogels. **e, f** Initial state (e, 0 ns) and equilibrium state (f, 100 ns) of the interaction between Cellulose hydrogels and laccase by molecular dynamics (MD) simulation. The cyan box is a cube water box of 10×10×10 nm. **g** Contribution of different amino acids to H-bond formation between laccase and Cellulose hydrogels within 100 ns MD simulation. Aspartic acid: Asp (71.13%), Arginine: Arg (11.94%), Histidine: His (9.01%), Serine: Ser (2.37%), Leucine: Leu (3.46%), Glutamine: Gln (1.04%), Threonine: Thr (1.05%). **h, i** Strength (**h**, $E_{\text{H-bond}}$, kJ mol^{-1}) and stability (**i**, E_{gap}, eV) of the H-bond between Asp/Arg/His from laccase and Cellulose hydrogels quantified through DFT calculations. For (**a**), data are presented as mean ± S.D. from three replicates (n = 3).

Note: The formation of CAHB between Cellulose hydrogels and laccase is supported by their |ΔPZC| (0.70, Supplementary Fig. 26a) being less than 5.0, indicating a basis for potential CAHB interaction. Moreover, the analysis of solution pH before and after laccase assembly

demonstrates a significant and linear increase with increasing assembled amount of laccase ($p < 0.05$) (Supplementary Fig. 26b). This can be attributed to the release of OH^- during CAHB formation, as H^+ from the solvent H_2O is involved in this process. Additionally, new peaks were observed on the FTIR spectra of Cellulose hydrogels at high frequencies (3782 cm^{-1}, Supplementary Fig. 26c) and in the extremely low-field region of their ^1H NMR spectra (17.54 ppm, Supplementary Fig. 26d), indicating CAHB formation upon laccase assembly. Interestingly, these peaks associated with CAHB disappeared when D_2O was used as a solvent instead of H_2O (deuteration), strongly indicating H_2O was involved in CAHB formation. To investigate the binding sites on laccase and gain a deeper understanding of the molecular-level mechanisms involved in CAHB formation, we performed MD simulations and DFT calculations. At 100 ns equilibrium, H-bonds were established between –OH groups on cellulose chains of Cellulose hydrogels and –COOH groups on Asp486 in laccase (Supplementary Fig. 26e-f). Further analysis revealed that Asp contributed to the largest fraction (71.13%) in H-bond formation within the laccase-assembled Cellulose hydrogels (Supplementary Fig. 26g). The significant contribution of Asp can be attributed to the formation of strong CAHB between its –COOH groups and the –OH groups on the Cellulose hydrogels (-121.99 kJ mol^{-1}, Supplementary Fig. 26h), supported by their $|\Delta PZC| < 5.0$ (1.18). In contrast, weaker ordinary H-bonds were formed between the Cellulose hydrogels and –NH groups on Arg (-14.41 kJ mol^{-1}) or His (-16.16 kJ mol^{-1}), as their $|\Delta PZC|$ were as high as 8.48 or 9.17, respectively, contributing only a small fraction to laccase assembly. Furthermore, CAHB exhibited a greater E_{gap} value (4.75 eV) compared to the ordinary H-bonds ($\leq$ 3.26 eV), indicating its higher stability (Supplementary Fig. 26i). These findings collectively provide compelling evidence for facilitated laccase assembly on Cellulose hydrogels by CAHB.

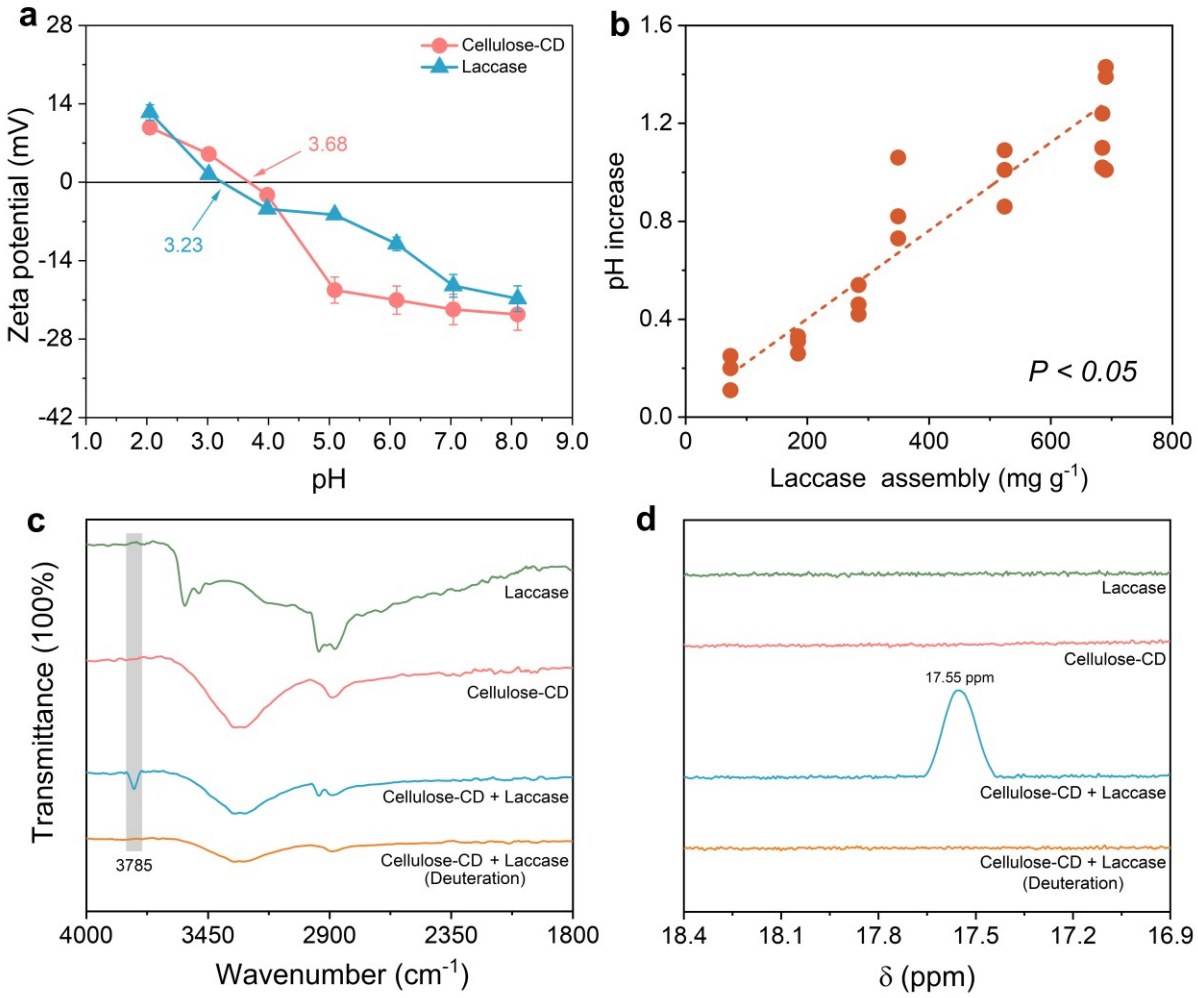

Supplementary Fig. 27. Assembly mechanism of laccase on Cellulose-CD hydrogels by CAHB. a The PZC of Cellulose-CD hydrogels and laccase. **b** The relationship between assembled amount of laccase on Cellulose-CD hydrogels and solution pH. **c, d** FTIR (**c**) and ^{1}H NMR (**d**) spectra of laccase before and after assembly (including deuteration) on Cellulose-CD hydrogels. Since the MD and DFT models for both Cellulose-CD hydrogels and Cellulose-CD-MMT hydrogels can be represented by the same model ($C_{82}H_{138}O_{65}$, see Supplementary Note 9 for details), the MD/DFT results for the interaction (H-bonding) between laccase and Cellulose-CD-MMT hydrogels (e.g., Fig. 3) can also indicate the interaction between laccase and Cellulose-CD hydrogels. For (**a**), data are presented as mean ± S.D. from three replicates (n = 3).

Note: The formation of CAHB between Cellulose-CD hydrogels and laccase is supported by their |ΔPZC| (0.45, Supplementary Fig. 27a) being less than 5.0, indicating a basis for potential CAHB interaction. Moreover, the analysis of solution pH before and after laccase assembly demonstrated a significant and linear increase with increasing assembled amount of laccase (p

< 0.05) (Supplementary Fig. 27b), which is consistent with the laccase assembly on Cellulose-CD hydrogels. The results of FTIR (3785 cm^{-1}, Supplementary Fig. 27c) and ^{1}H NMR (17.55 ppm, Supplementary Fig. 27d) of laccase assembly on Cellulose-CD hydrogels further verified CAHB formation between them.

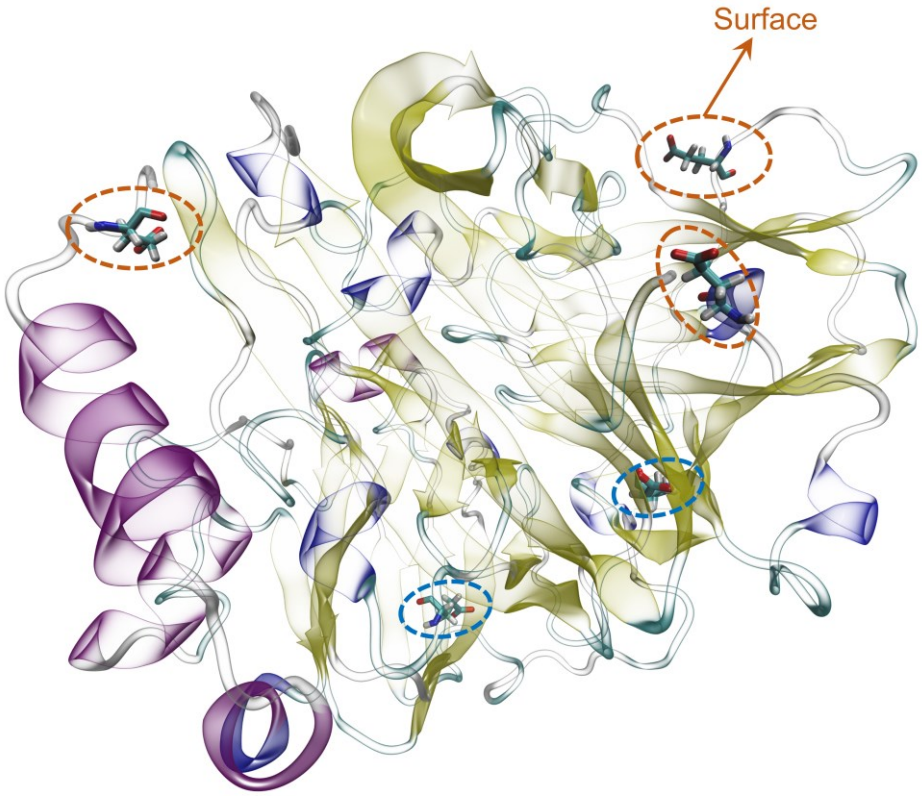

Supplementary Fig. 28. Schematic diagram of the distribution of glutamic acid on the surface of laccase. Yellow dashed circles: surface of laccase, blue dashed circles: inside of laccase.

Note: Glutamic acid (Glu) theoretically could form CAHB with the hydrogels since their |ΔPZC| is also less than 5.0. However, our study did not observe significant CAHB formation between them by MD simulation (Fig. 3g and Supplementary Fig. 26g) due to several potential factors: (1) the amount of Glu present in laccase was limited; for example, only five Glus were found in laccase, and only three of them were exposed on its surface (Supplementary Fig. 28), resulting in a low opportunity to form CAHB with the hydrogels; (2) steric hindrance within enzyme may prevent optimal orientation of the carboxylic groups on Glu to interact with the hydroxyl groups of hydrogels via CAHB; (3) other amino acids such as Asp may compete for CAHB interactions with hydrogels, thus overshadowing the potential contribution from Glu.

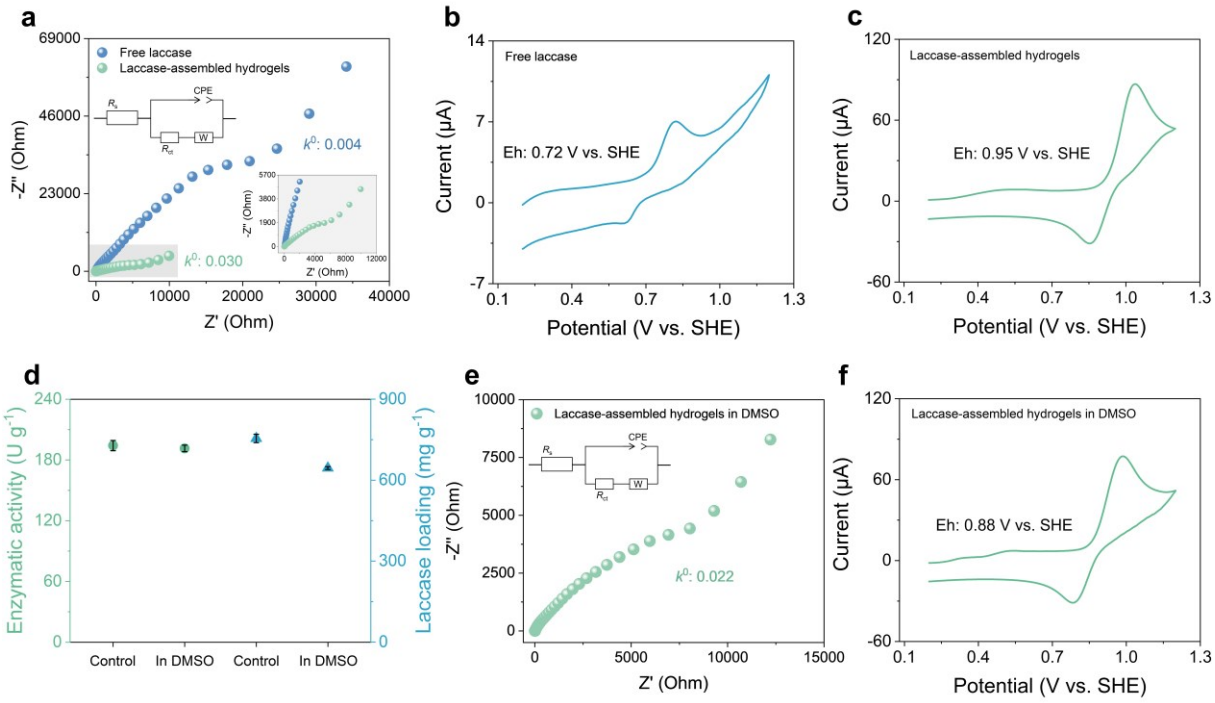

Supplementary Fig. 29. Redox potential and electron transfer rate of free- and laccase-assembled Cellulose-CD-MMT hydrogels. a Electrochemical impedance spectroscopy (EIS) of free- and laccase-assembled Cellulose-CD-MMT hydrogels. k^0: Electron transfer rate constant (cm s^{-1}). The resulting Nyquist plots were fitted with a Randles equivalent circuit model. The resulting equivalent circuit involves four elements; solution resistance (R_s), charge transfer resistance (R_{ct}), Warburg element (W, related to the diffusion resistance of double layer at electrolyte/electrode interface) and constant phase element (CPE) related to the double layer capacitance[155-157]. **b-c** Cyclic voltammograms (CV) for free laccase (**b**) and laccase-assembled Cellulose-CD-MMT hydrogels (**c**). Redox potential: Eh (V). A glassy carbon working electrode, a Ag/AgCl reference electrode, and a platinum plate as the auxiliary electrode. The redox potential measured for the laccase-assembled hydrogels represents apparent redox potential of the entire heterogeneous catalyst system, which includes both the immobilized laccase and the Cellulose-CD-MMT hydrogels. The inherent redox potential of laccase itself likely remains unchanged, as altering its intrinsic redox potential would generally cause significant changes in its three-dimensional structure; no noticeable conformational changes were observed in the immobilized laccase in this study. The increase in apparent redox potential of the laccase-assembled hydrogels allows for more effective pollutant degradation without mediators. **d** Enzymatic activity (U g^{-1}) and laccase loading (mg g^{-1}) of the laccase-assembled hydrogels both before and after immersion in 10 vol% DMSO for 24 h. **e-f** EIS (**e**) and CV (**f**) of the laccase-assembled hydrogels after immersion in 10 vol% DMSO for 24 h. For (**d**), data are presented as mean ± S.D. from three replicates (n = 3).

Note (Supplementary Fig. 29): Theoretically, the preferred substrate of laccase is phenolic compounds, but it is widely used in pollution remediation due to its broad substrate spectrum, which extends to various aromatic compounds (e.g., PAHs). The degradation of PAHs is often limited by several factors, including low redox potential, poor substrate affinity/concentration/mass-transfer, and restricted electron transfer rate/activity/stability, which results in low pollutant removal efficiency. Regarding the shortcomings of redox potential and electron transfer rate, the use of mediators can effectively address them. However, free laccases have been shown to degrade PAHs without mediators to nearly 20.6%-99.0% (Supplementary Table 8). This indicates that the redox potential of free laccase may be not the sole factor limiting PAHs degradation. Other factors that inhibit PAHs degradation by laccase could include: (1) low substrate concentration and electron transfer rate constant; (2) limited substrate affinity and poor mass transfer; and (3) reduced enzymatic activity and stability during degradation process. Therefore, our study focuses on addressing these specific knowledge gaps, as well as how to improve the redox potential and electron transfer rate constant without using mediators. This is particularly important as mediators can sometimes reduce or fail to enhance PAHs degradation efficiency due to their toxicity to laccases, which can impair enzymatic activity. For example, Ike et al.[101] reported that application of the mediator ABTS decreased the anthracene biodegradation by laccase by 14% (from 44% to 30%), and Zeng et al.[109] found no significant increase in degradation efficiency of anthracene with the addition of ABTS. Furthermore, the use of mediators also increases complexity of the remediation process and thus poses potential environmental risks.

The laccase-assembled hydrogels effectively address these limitations, particularly improving electron transfer rate (k^0, Supplementary Fig. 29a) and redox potential (Eh, Supplementary Fig. 29b-c). This improvement can be attributed to the combined effects of several factors: substrate capture by the hydrogel increases its affinity/concentration and mass-transfer, potentially promoting electron transfer and redox reactions. Specifically, the hydrogel

maintains or concentrates substrates near the enzyme's active site, reducing the high energy required for long-range reactions and making the electron transfer pathway more efficient; (2) the hydrogel protects the immobilized laccase without inactivating it, ensuring effective electron transfer and redox; (3) CAHB, as low-barrier hydrogen bonds with symmetrical hydrogen bonding donor-acceptor pairs[5,11,12], likely facilitates rapid electron transmission, long-range communication, and optimized redox behavior[158-161]; this has been demonstrated in previous studies[158-161], such as Dai et al.[158], who found that low-barrier hydrogen bonds enhance long-range communication and electron transmission in enzymatic catalytic process. Similarly, Yang et al.[160] and Peng et al.[161] reported that low-barrier hydrogen bonds can regulate redox balance, thereby optimizing the redox behavior during the reaction process. These factors jointly lead to a higher electron transfer rate (0.030 cm s^{-1}) and apparent redox potential (0.95 V vs. SHE) for the laccase-assembled hydrogels, compared to free laccase (0.72 V vs. SHE; 0.004 cm s^{-1}) (Supplementary Fig. 29a-c). In addition, the above three factors theoretically occur simultaneously and synergistically, thus making it exceptionally challenging to isolate or quantify their individual contributions.

Additionally, to validate the roles of CAHB in changing the redox potential and electron transfer rate, control experiments were conducted using DMSO (a known hydrogen bond breaker) to disrupt the CAHB between the enzyme and the hydrogels. The results showed that, in the presence of DMSO, the laccase loading on hydrogels decreased from 754.5 mg g^{-1} to 644.6 mg g^{-1}, indicating disruption of the CAHB, but without significant impact on the enzymatic activity of the laccase-assembled hydrogels (Supplementary Fig. 29d). In such case, DMSO reduced the redox potential (V vs. SHE) and electron transfer rate (cm s^{-1}) from values of “0.95 and 0.030” to “0.88 and 0.022”, respectively (Supplementary Fig. 29e-f). These observations provide evidence that CAHB plays a facilitating role in optimizing redox potential and electron transfer rate.

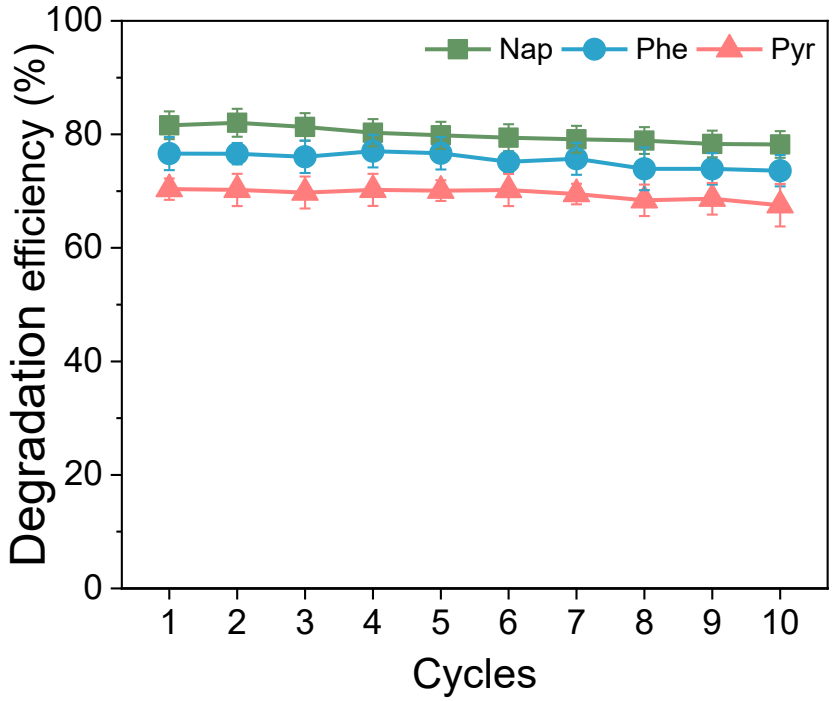

Supplementary Fig. 30. Reusability of the laccase-assembled hydrogels for removal (net degradation) of PAHs (80 μg L^{-1}), and recycling was repeated 10 times. Data are presented as mean ± S.D. from three replicates (n = 3). After undergoing 10 cycles, the assembled laccase exhibited a remarkable net degradation efficiency (Nap: 78.2%, Phe: 73.6%, Pyr: 67.5%).

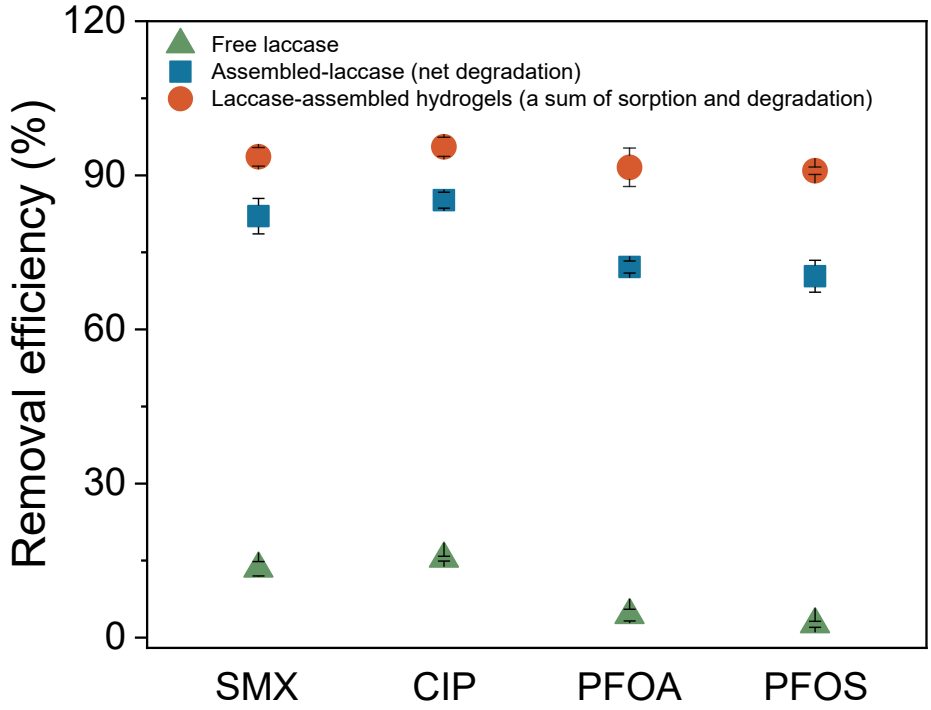

Supplementary Fig. 31. Removal efficiency of other organic pollutants of regulatory or popular concerns by the laccase-assembled Cellulose-CD-MMT hydrogels (a sum of sorption and degradation), assembled laccase (net degradation), and free laccase. Data are presented as mean ± S.D. from three replicates (n = 3). Time: 48 h; Concentration: 1.0 μg L^{-1}. Sulfamethoxazole: SMX; Ciprofloxacin: CIP; Perfluorooctanoic acid: PFOA; and Perfluorooctanesulfonic acid: PFOS. The concentration of these contaminants in supernatant was determined with the methods in previous reports[162-164].

Note: The total removal efficiencies of SMX, CIP, PFOA, and PFOS by the laccase-assembled Cellulose-CD-MMT hydrogels were 93.6%, 95.5%, 91.54%, 90.9%, respectively, which were significantly higher than that of free laccase (< 15.4%). The net degradation efficiency (> 70.4%) of these compounds by assembled laccase was 5.54 (CIP)-27.2 (PFOS) times that of free laccase. These results indicated that the laccase-assembled Cellulose-CD-MMT hydrogels have a great potential in environmental remediation of diverse organic pollutants. The degradation of these pollutants is achieved through a 1-hydroxybenzotriazole-mediated catalytic oxidation process.

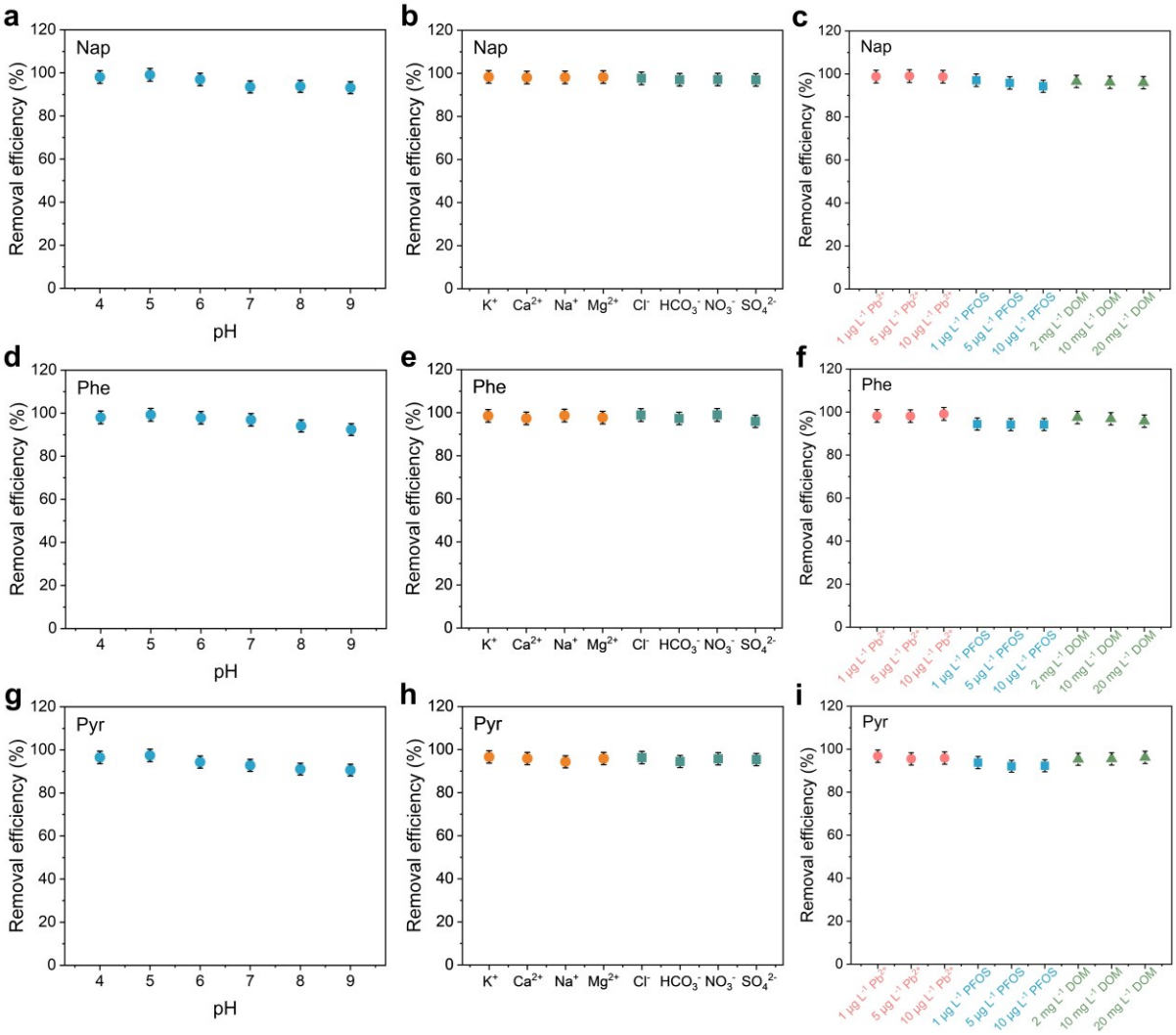

Supplementary Fig. 32. Effects of diverse and complex water conditions on removal performance (a sum of sorption and degradation) of PAHs (80 μg L^{-1}) by the laccase-assembled Cellulose-CD-MMT hydrogels. a, d and g Effects of pH variation (from 4 to 9) on the removal performance of Nap (**a**), Phe (**d**) and Pyr (**g**) by the laccase-assembled hydrogels at 25 °C. The pH range in natural water is generally within 5-9[165-167]. **b, e and h** Effects of various coexisting cations (K^+, Ca^{2+}, Na^+, and Mg^{2+}) and anions on removal performance of Nap (**b**), Phe (**e**) and Pyr (**h**) by the laccase-assembled hydrogels. The experimental concentration of these ions was set as 10 mg L^{-1}, which is close to that in real water[165,166]. Temperature: 25 °C, pH: 5.0 (unless otherwise specified, the same condition was used in the subsequent experiments). **c, f and i** Effects of the coexisting heavy metals (Pb^{2+}, 1-10 μg L^{-1}), organic contaminants (perfluorooctanesulfonic acid, PFOS, 1-10 μg L^{-1}) and dissolved organic matter (DOM, 2-20 mg L^{-1}) (humic acid) on removal performance of Nap (**c**), Phe (**f**) and Pyr (**i**) by the laccase-assembled hydrogels. Pb^{2+}, PFOS and humic acid were chosen as representatives of heavy metals, organic contaminant and DOM, respectively, which are widely detected in the water environment, and their experimental concentrations were set according to

that in the real water[144-148]. For (**a-i**), data are presented as mean ± S.D. from three replicates (*n* = 3).

Note: The total removal efficiency (Supplementary Fig. 32) of PAHs by the laccase-assembled Cellulose-CD-MMT hydrogels in the presence of K^+, Ca^{2+}, Na^+, Mg^{2+}, Cl^-, HCO_3^-, NO_3^-, and SO_4^{2-} was over 97.0% for Nap, 96.0% for Phe, and 95.8% for Pyr, and net degradation efficiency (Supplementary Fig. 33) of PAHs in the presence of these anions or cations was over 81.8% for Nap, 73.7% for Phe, and 70.7% for Pyr. Moreover, the total removal and net degradation efficiency of PAHs at pH 4-9 exceeded 90.6% (Nap > 93.1%, Phe > 92.3%, and Pyr > 90.6%) and 68.5% (Nap > 79.6%, Phe > 74.2%, and Pyr > 68.5%), respectively. Similarly, the co-presence of Pb^{2+}, PFOS and DOM did not significantly decrease the removal efficiency of these three PAHs ($\leqslant$ 5.39% inhibition for all cases).

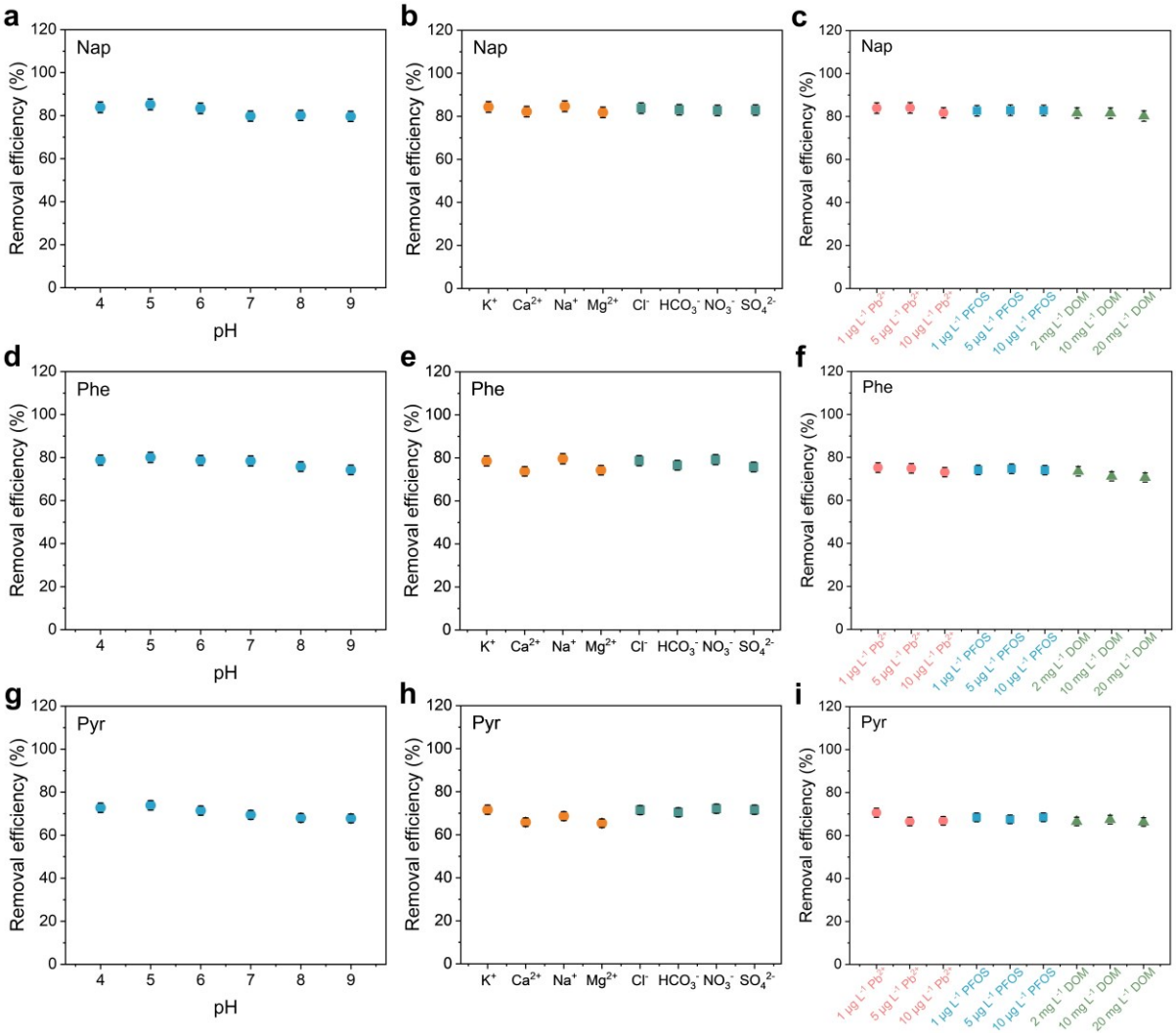

Supplementary Fig. 33. Effects of diverse and complex water conditions on net degradation performance of PAHs (80 μg L^{-1}) by the assembled laccase. a, d and **g** Effects of pH variation (from 4 to 9) on degraded percentage of Nap (**a**), Phe (**d**) and Pyr (**g**) by the assembled laccase at 25 °C. The pH range in natural water is generally within 5-9. **b, e** and **h** Effects of various coexisting cations (K^+, Ca^{2+}, Na^+, and Mg^{2+}) and anions (Cl^-, HCO_3^-, NO_3^-, and SO_4^{2-}) on degraded percentage of Nap (**b**), Phe (**e**) and Pyr (**h**) by the assembled laccase. The experimental concentration of these ions was set as 10 mg L^{-1}, which is close to that in the real water. Temperature: 25 °C, pH: 5.0 (unless otherwise specified, the same condition was used in the subsequent experiments). **c, f** and **i** Effects of the coexisting heavy metals (Pb^{2+}, 1-10 μg L^{-1}), organic contaminants (perfluorooctanesulfonic acid, PFOS, 1-10 μg L^{-1}) and dissolved organic matter (DOM, 2-20 mg L^{-1}) (humic acid) on degraded percentage of Nap (**c**), Phe (**f**) and Pyr (**i**) by the assembled laccase. Pb^{2+}, PFOS and humic acid were chosen as representatives of heavy metals, organic contaminant and DOM, respectively, which are widely detected in the water environment, and their experimental concentrations were set according to that in the real water. For (**a-i**), data are presented as mean ± S.D. from three replicates (n = 3).

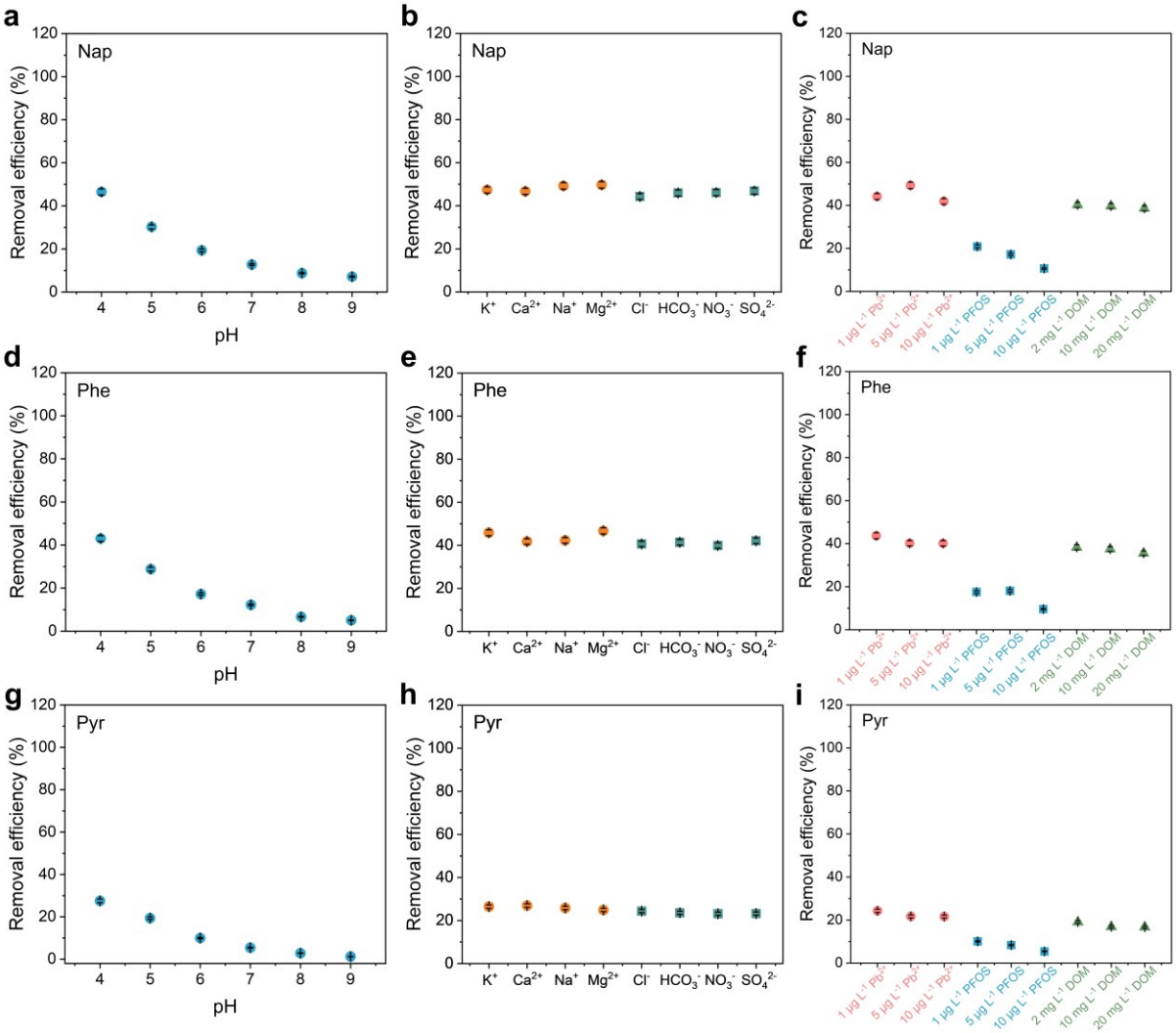

Supplementary Fig. 34. Effects of diverse and complex water conditions on degradation performance of PAHs (80 μg L^{-1}) by free laccase. a, d and **g** Effects of pH variation (from 4 to 9) on the degraded percentage of Nap (**a**), Phe (**d**) and Pyr (**g**) by the free laccase at 45 °C. The pH range in natural water is generally within 5-9. **b, e** and **h** Effects of various coexisting cations (K^+, Ca^{2+}, Na^+, and Mg^{2+}) and anions (Cl^-, HCO_3^-, NO_3^-, SO_4^{2-}) on degraded percentage of Nap (**b**), Phe (**e**) and Pyr (**h**) by free laccase. The experimental concentration of these ions was set as 10 mg L^{-1}, which is close to that in the real water. Temperature: 45 °C, pH: 4.0 (unless otherwise specified, the same condition was used in the subsequent experiments). **c, f** and **i** Effects of the coexisting heavy metals (Pb^{2+}, 1-10 μg L^{-1}), organic contaminants (perfluorooctanesulfonic acid, PFOS, 1-10 μg L^{-1}) and dissolved organic matter (DOM, 2-20 mg L^{-1}) (humic acid) on degraded percentage of Nap (**c**), Phe (**f**) and Pyr (**i**) by free laccase. Pb^{2+}, PFOS and humic acid were chosen as representatives of heavy metals, organic contaminant and DOM, respectively, which are widely detected in the water environment, and their experimental concentrations were set according to that in the real water. For (**a-i**), data are presented as mean ± S.D. from three replicates (n = 3).

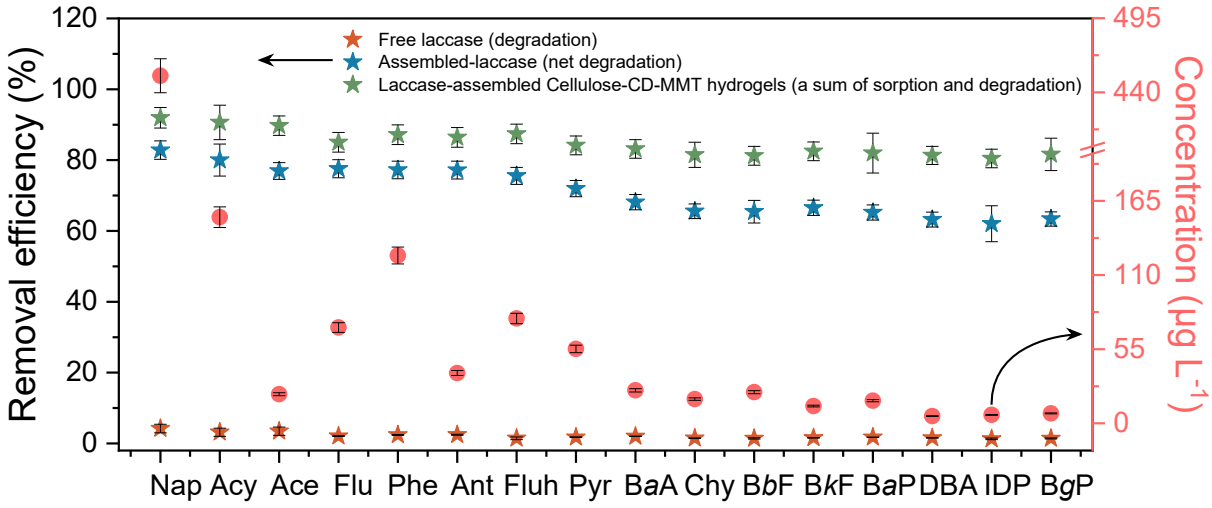

Supplementary Fig. 35. Removal efficiency of 16 USEPA priority PAHs in a Coal Chemical Plant wastewater collected from Ningxia, China, by the laccase-assembled Cellulose-CD-MMT hydrogels (a sum of sorption and degradation), assembled laccase (net degradation), and free laccase, as well as the measured concentrations of 16 USEPA priority PAHs. Data are presented as mean ± S.D. from three replicates (n = 3). Time: 24 h (Supplementary Fig. 36). 16 USEPA priority PAHs: Naphthalene (Nap), acenaphthylene (Acy), acenaphthene (Ace), fluorene (Flu), Phenanthrene (Phe), anthracene (Ant), fluoranthene (Fluh), Pyrene (Pyr), benzo(*a*)anthracene (B*a*A), chrysene (Chy), benzo(*b*)fluoranthene (B*b*F), benzo(*k*)fluoranthene (B*k*F), benzo(*a*)pyrene (B*a*P), dibenzo(*a,h*)anthracene (DBA), indeno(*1,2,3-cd*)pyrene (IDP) and benzo(*g,h,i*)perylene (B*g*P).

Note: The removal efficiency of 16 USEPA priority PAHs by the free laccase was below 4.23%, which can be attributed to the susceptibility of free laccase to inactivation in the complex environment of the real wastewater (Supplementary Table 10). In contrast, the total removal efficiency of 16 USEPA priority PAHs by the laccase-assembled Cellulose-CD-MMT hydrogels ranged from 80.4% to 91.9% (net degradation efficiency of 62.0%-82.8%), which was 21.77 times (Nap) - 62.28 times (indeno(*1,2,3-cd*)pyrene) that by the free laccase. Notably, sorption efficiency of 16 USEPA priority PAHs by the laccase-assembled Cellulose-CD-MMT hydrogels increased with increasing hydrophobicity (Supplementary Table 9), because CD doped on the hydrogels tended to capture PAHs with strong hydrophobicity. Although PAHs with high benzene ring numbers and persistence are difficult to be degraded by laccase, and the net degradation efficiency of PAHs by the assembled laccase decreased as the benzene ring numbers of PAHs increased, it was still 19.61 (Nap)-52.34 (fluoranthene) times (62.0%-82.8%) that by the free laccase.

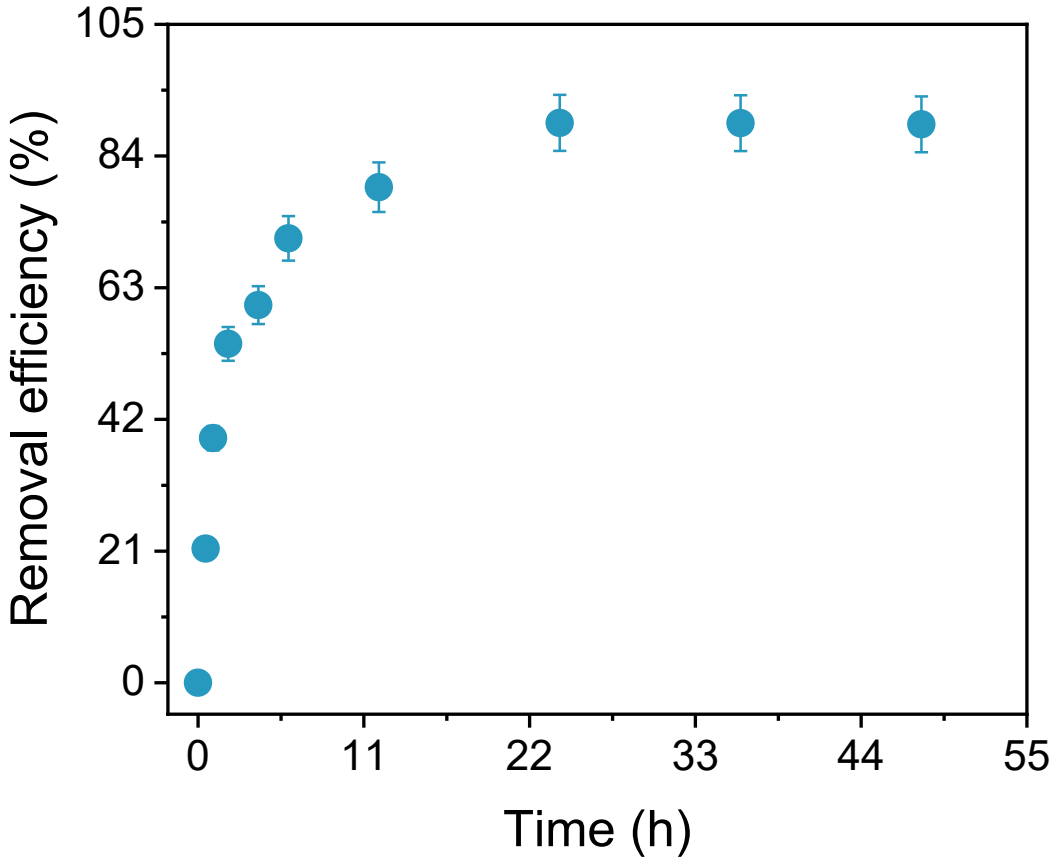

Supplementary Fig. 36. Removal equilibrium time of ∑16PAHs in a Coal Chemical Plant wastewater collected from Ningxia, China, by the laccase-assembled Cellulose-CD-MMT hydrogels. Data are presented as mean ± S.D. from three replicates (n = 3). The removal equilibrium was reached at 24 h.

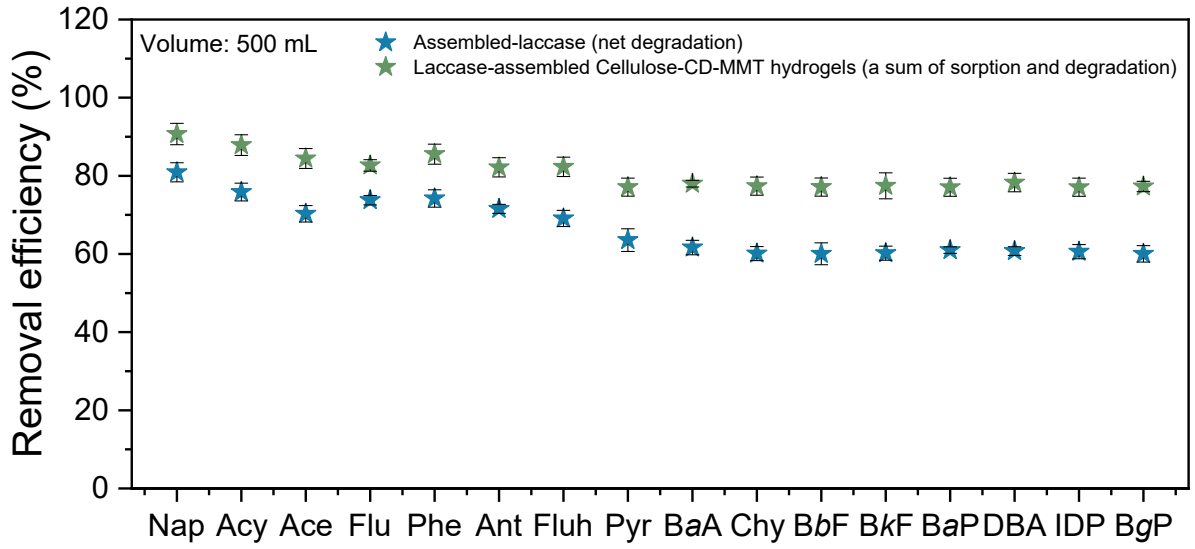

Supplementary Fig. 37. Removal efficiency of 16 USEPA priority PAHs in a Coal Chemical Plant wastewater (large reaction system: 500 mL) collected from Ningxia, China, by the laccase-assembled Cellulose-CD-MMT hydrogels (a sum of sorption and degradation), assembled laccase (net degradation), and free laccase. Data are presented as mean ± S.D. from three replicates (n = 3). Time: 24 h. Their total removal efficiency (a sum of sorption and degradation) and net degradation efficiency by the laccase-assembled Cellulose-CD-MMT hydrogels ranged from 77.1%-90.7% and 60.0%-80.9%, respectively, with insignificant change compared to that in the 15 mL reaction system, demonstrating significant potential for practical application.

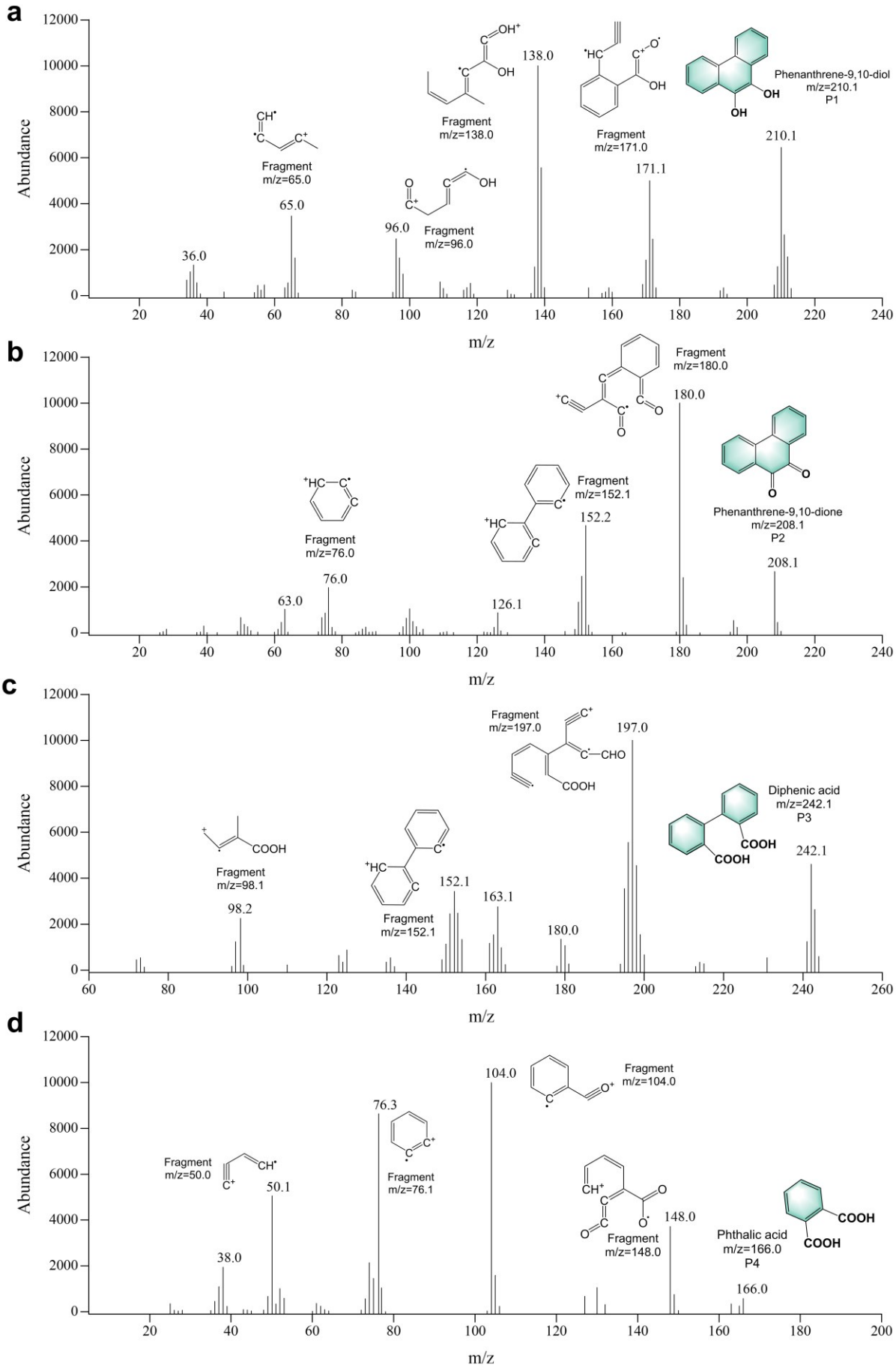
a
Abundance
m/z
Fragment m/z=65.0
Fragment m/z=138.0
Fragment m/z=96.0
Fragment m/z=171.0
Phenanthrene-9,10-diol m/z=210.1 P1
36.0
65.0
96.0
138.0
171.1
210.1
b
Fragment m/z=180.0
Fragment m/z=152.1
Fragment m/z=76.0
Phenanthrene-9,10-dione m/z=208.1 P2
63.0
76.0
126.1
152.2
180.0
208.1
c
Fragment m/z=197.0
Fragment m/z=98.1
Fragment m/z=152.1
Diphenic acid m/z=242.1 P3
98.2
152.1
163.1
180.0
197.0
242.1
d
Fragment m/z=104.0
Fragment m/z=50.0
Fragment m/z=76.1
Fragment m/z=148.0
Phthalic acid m/z=166.0 P4
38.0
50.1
76.3
104.0
148.0
166.0

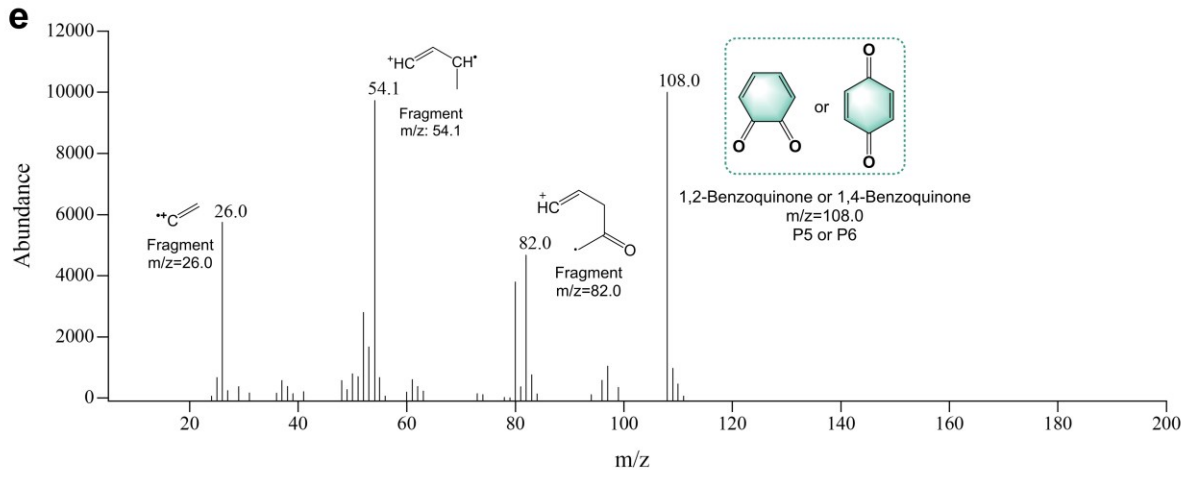

Supplementary Fig. 38. Mass spectra of the intermediate products generated during Phe degradation by the assembled laccase as identified by GC-MS, as well as that of their possible fragment ions. a Phenanthrene-9,10-diol (P1, m/z 210.1). **b** Phenanthrene-9,10-dione (P2, m/z 208.1). **c** Diphenic acid (P3, m/z 242.1). **d** Phthalic acid (P4, m/z 166.0). **e** 1,2-benzoquinone or 1,4-benzoquinone (P5 or P6, m/z 108.0).

Note: The peaks for the intermediate product fragments on some mass spectra are higher than those of the intermediate products themselves (Supplementary Figs. 36, 38, 40). This phenomenon can be attributed to structural instability of the high-energy intermediate product ions generated by electron ionization (EI, 70eV) in GC-MS, leading to further fragmentation and abundant fragment ions[168-170].

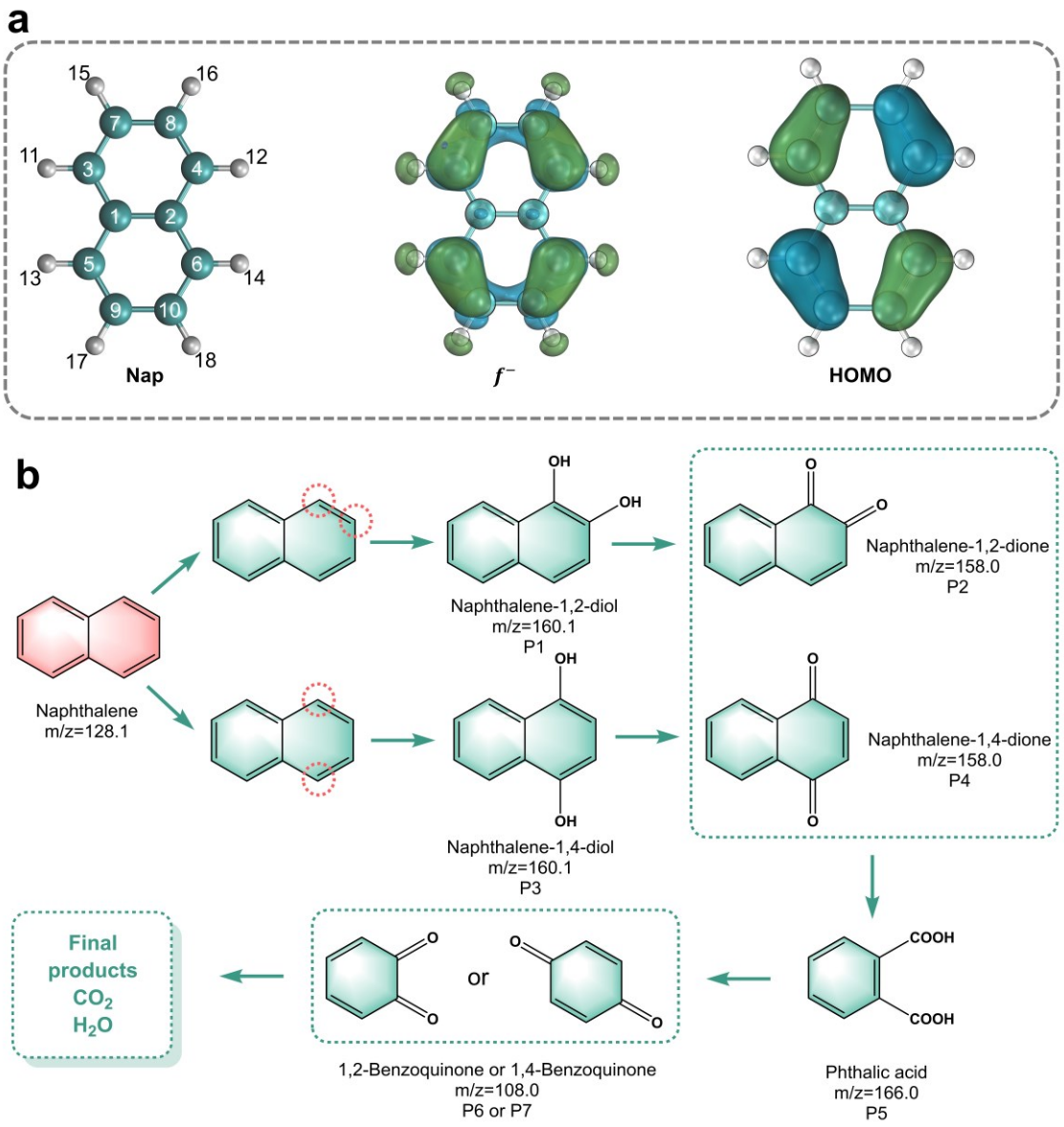

Supplementary Fig. 39. Degradation mechanism and pathway of Nap by the assembled laccase. a Nap molecular structure with labeled atomic positions, the HOMO of Nap, and the distribution of electrophilic (f_A^-) attacking sites based on compressed Fukui function (CFF). **b** Proposed degradation pathways of Nap by the assembled laccase.

Note: The sites with high f_A^- values (Supplementary Table 13) and plenty of HOMO on the Nap molecule are at C3-C6 (0.0991) and C7-C10 (0.0708). After undergoing attack by the assembled laccase, Nap was converted to naphthalene-1,2-diol or naphthalene-1,4-diol (P1 or P3, m/z 160.1), then to naphthalene-1,2-dione or naphthalene-1,4-dione (P2 or P4, m/z 158.0) by tautomerization. The intermediate product P2 or P4 was then converted to phthalic acid (P5, m/z 166), followed by oxidation to 1,2-benzoquinone (P6) or 1,4-benzoquinone (P7). It was finally mineralized to CO_2 and H_2O, similar to that for Phe.

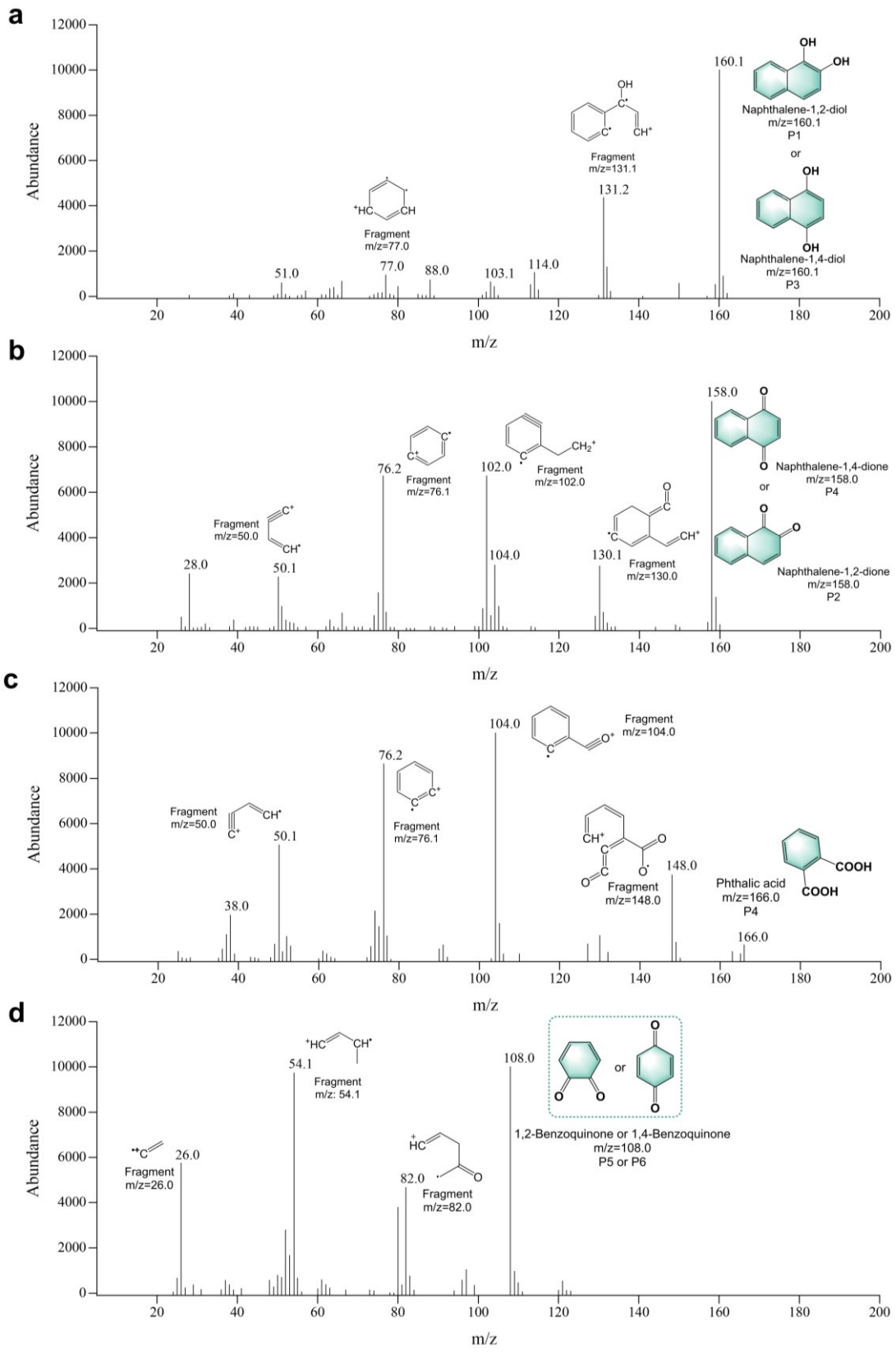

Supplementary Fig. 40. The intermediate products generated during Nap degradation by the assembled laccase as identified by GC-MS, as well as that of their possible fragment ions. a Naphthalene-1,2-diol or naphthalene-1,4-diol (P1 or P3, m/z=160.1). **b** Naphthalene-1,2-dione or naphthalene-1,4-dione (P2 or P4, m/z=158.0). **c** Phthalic acid (P5, m/z 166.0). **d** 1,2-benzoquinone or 1,4-benzoquinone (P6 or P7, m/z 108.0).

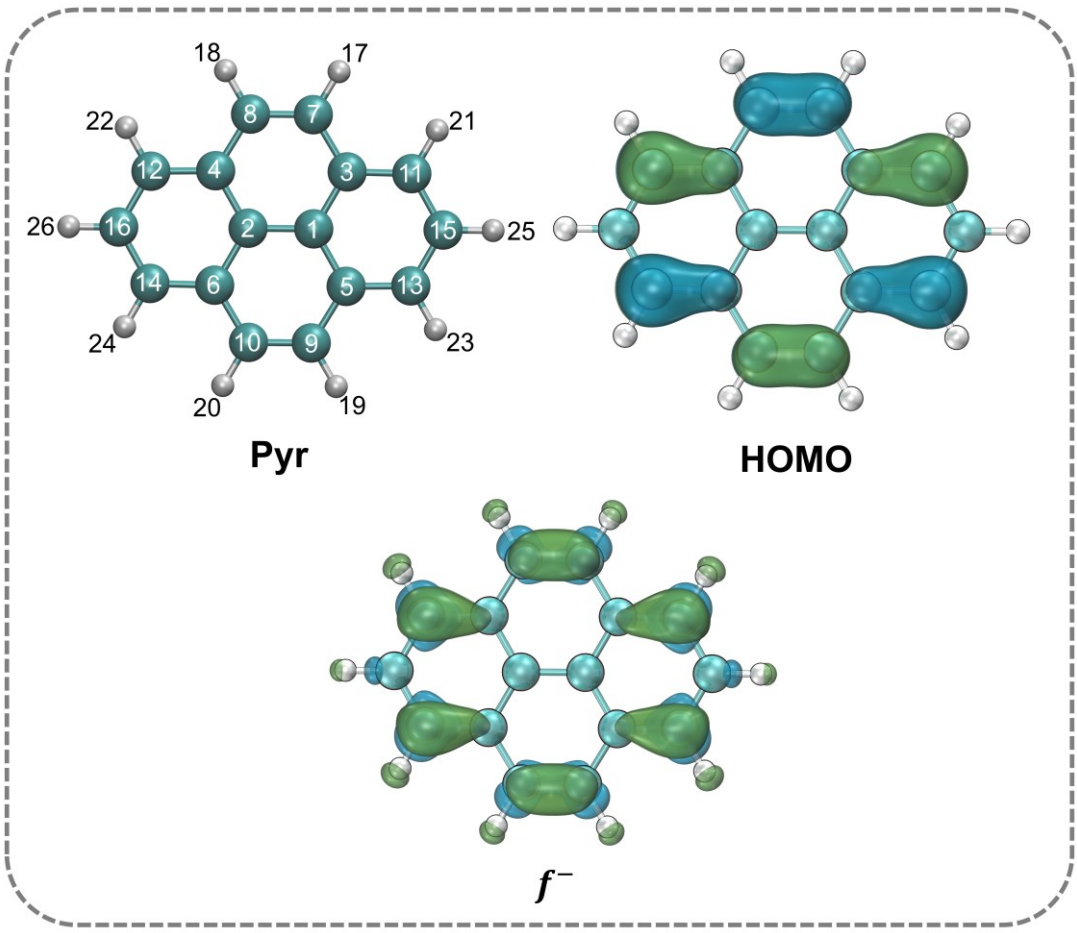

Supplementary Fig. 41. Pyr molecular structure with labeled atomic positions, the HOMO of Pyr, and the distribution of electrophilic (f_A^-) attacking sites based on compressed Fukui function (CFF).

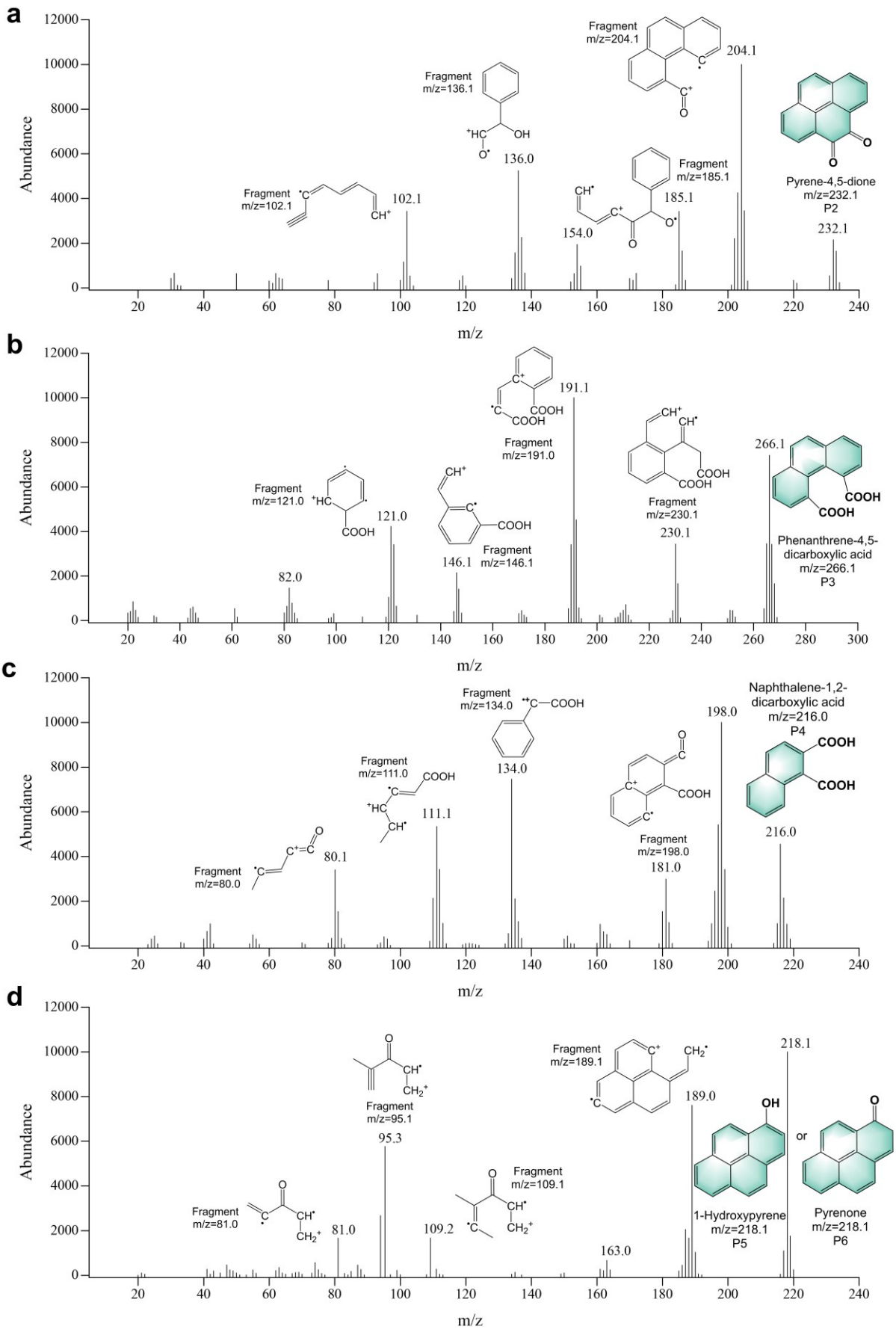
a
Abundance
m/z
Fragment m/z=204.1
204.1
Fragment m/z=136.1
136.0
Fragment m/z=185.1
185.1
Fragment m/z=102.1
102.1
154.0
Pyrene-4,5-dione
m/z=232.1
P2
232.1
b
Abundance
m/z
191.1
Fragment m/z=191.0
266.1
Fragment m/z=121.0
121.0
Fragment m/z=146.1
146.1
Fragment m/z=230.1
230.1
82.0
Phenanthrene-4,5-dicarboxylic acid
m/z=266.1
P3
c
Abundance
m/z
Fragment m/z=134.0
134.0
Naphthalene-1,2-dicarboxylic acid
m/z=216.0
P4
198.0
Fragment m/z=111.0
111.1
Fragment m/z=198.0
181.0
216.0
Fragment m/z=80.0
80.1
d
Abundance
m/z
Fragment m/z=189.1
218.1
189.0
Fragment m/z=95.1
95.3
Fragment m/z=109.1
Fragment m/z=81.0
81.0
109.2
163.0
or
1-Hydroxypyrene
m/z=218.1
P5
Pyrenone
m/z=218.1
P6

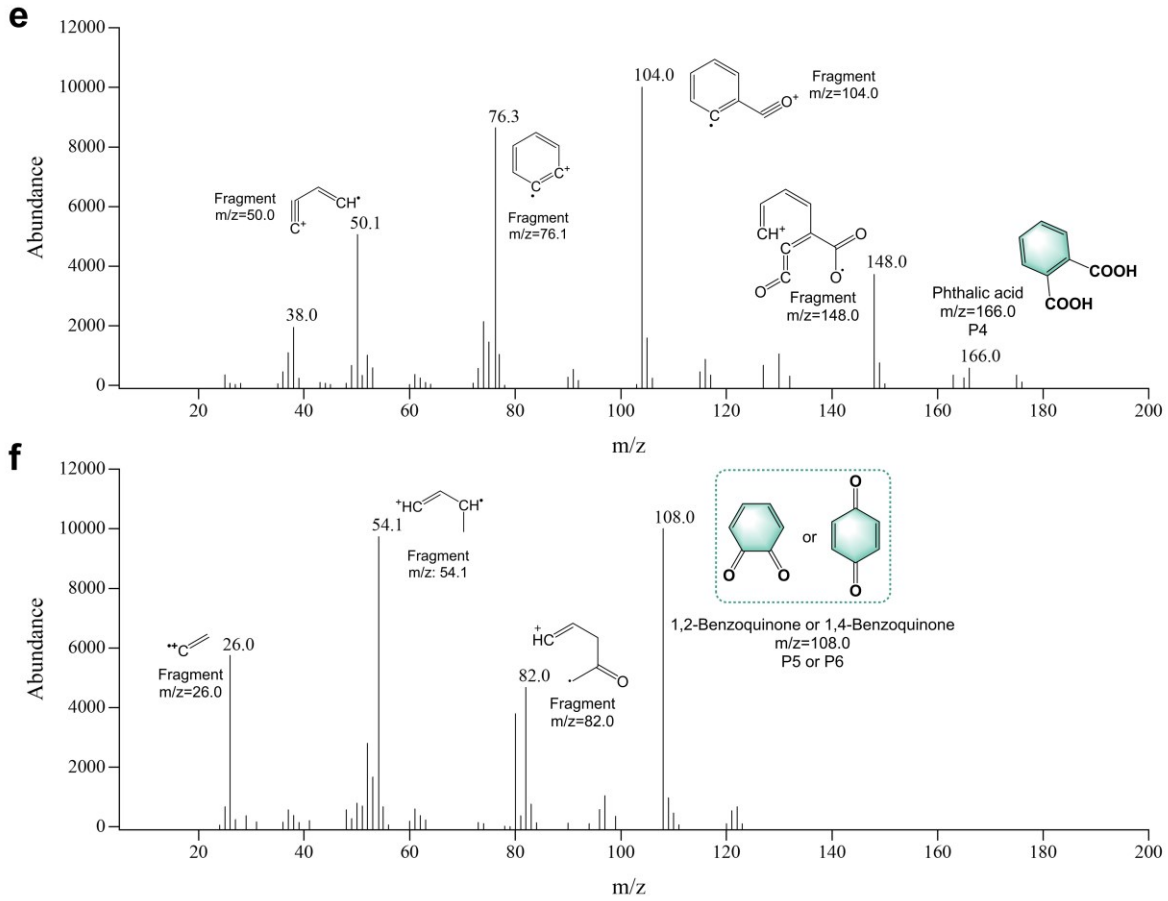

Supplementary Fig. 42. The intermediate products generated during Pyr degradation by the assembled laccase as identified by GC-MS, as well as that of their possible fragment ions. a Pyrene-4,5-dione (P2, m/z 232.1). **b** Phenanthrene-4,5-dicarboxylic acid (P3, m/z 266.1). **c** Naphthalene-1,2-dicarboxylic acid (P4, m/z 216.0). **d** 1-hydroxypyrene or pyrenone (P5 or P6, m/z 218.1). **e** Phthalic acid (P8, m/z 166.0). **f** 1,2-benzoquinone or 1,4-benzoquinone (P9 or P10, m/z 108.0).

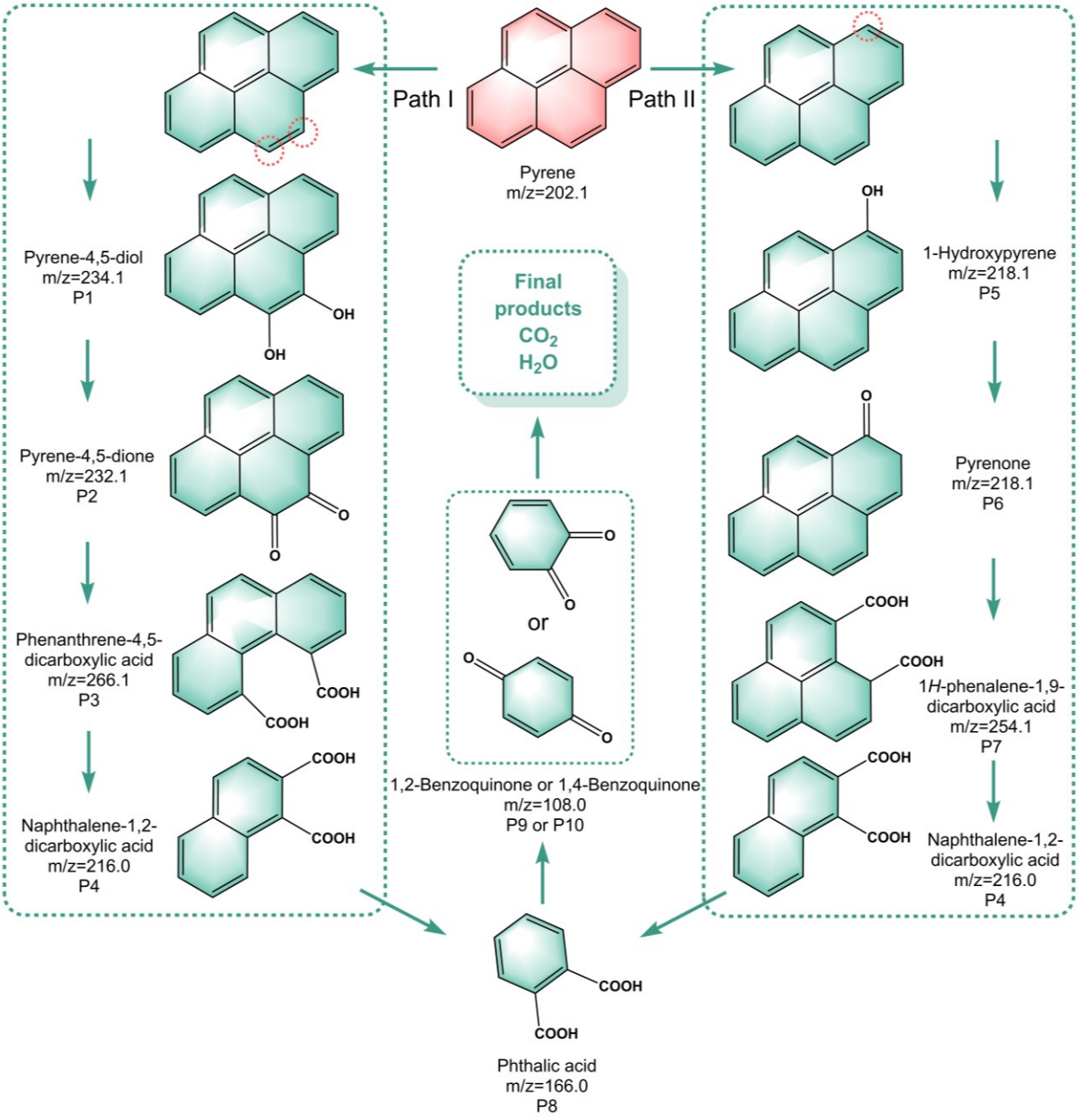

Supplementary Fig. 43. Degradation pathway proposed for Pyr by the assembled laccase.

Note: The HOMO distribution and the f_A^- values at C7-C10 (0.0578) and C11-C14 (0.0751) are more and higher than other atoms (Supplementary Fig. 41, Supplementary Table 14). Based on the identified degraded products (Supplementary Fig. 42), two possible degradation pathways for Pyr were proposed (Supplementary Fig. 43). In pathway I, it converted to pyrene-4,5-diol (P1, m/z 234.1) and pyrene-4,5-dione (P2, m/z 232.1) after attack to the atoms at C9 and C10. Subsequently, P2 underwent ring-opening and converted to phenanthrene-4,5-dicarboxylic acid (P3, m/z 266.1). It was then oxidized to naphthalene-1,2-dicarboxylic acid

(P4, m/z 216.0). Path II exhibited a similar pattern to path I. The attack on C11 led to the generation of 1-hydroxypyrene (P5, m/z 218.1). It was then converted to pyrenone (P6, m/z 218.1) by tautomerization. P6 experienced two successive ring-opening reactions, generating both 1*H*-phenalene-1,9-dicarboxylic acid (P7, m/z 254.1) and naphthalene-1,2-dicarboxylic acid (P4, m/z 216.0). P4 in paths I and II could be further converted to phthalic acid (P8, m/z 166.0), followed by the same degradation pathway as that for Phe.

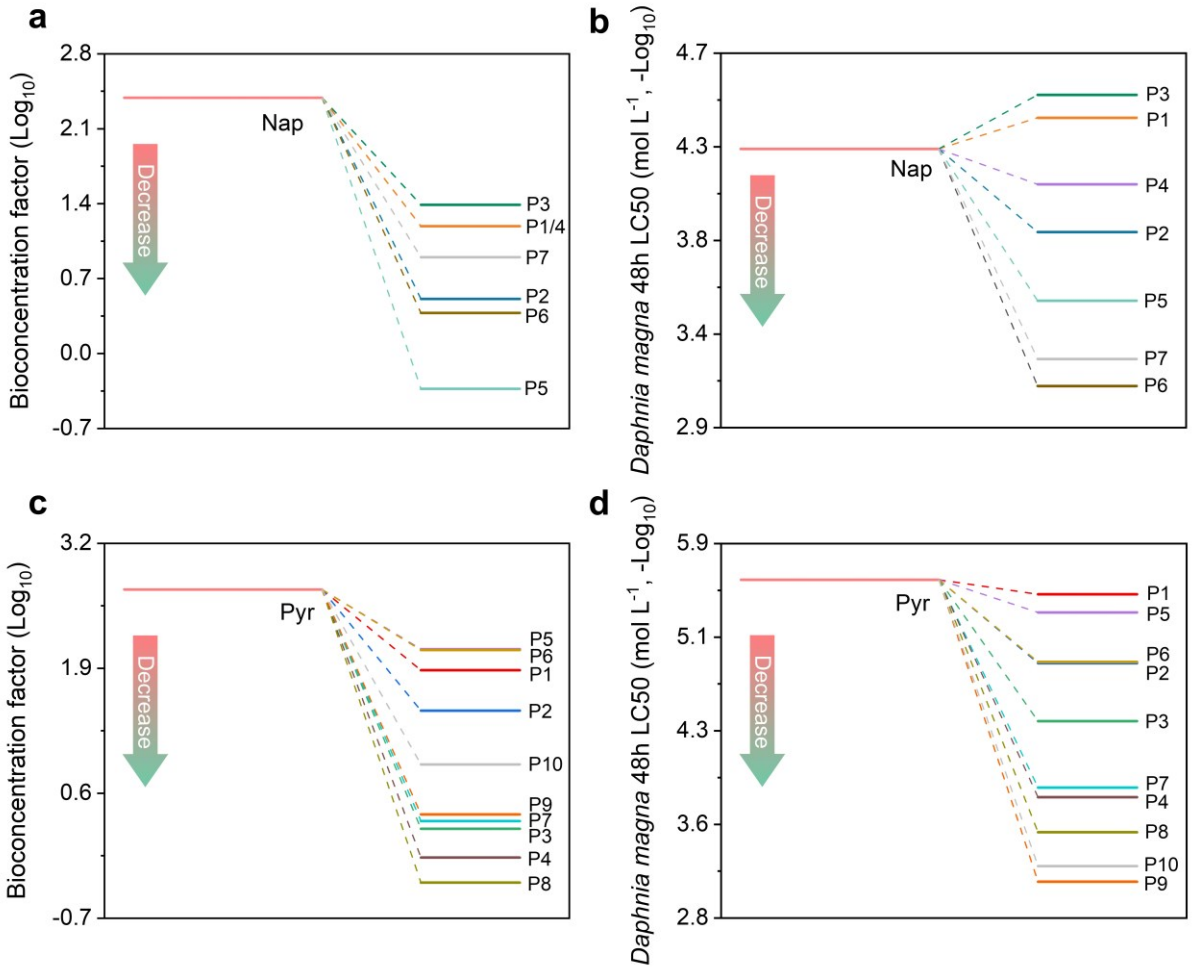

Supplementary Fig. 44. The acute toxicity and bioconcentration factor (BCF, Log_{10}) of Nap, Pyr and their degraded intermediates. a and c BCF of Nap (2.39) and Pyr (2.72) including their degraded intermediates. The BCF values of Nap and Pyr degraded intermediates are lower than those of their parents. **b** and **d** -Log_{10} *Daphnia magna* 48h LC50 (*Daphnia magna* -$Log_{10}^{(48\ h\ LC50)}$) for Nap (4.24 mol L^{-1}) and Pyr (5.60 mol L^{-1}) including their degraded intermediates. The *Daphnia magna* -$Log_{10}^{(48\ h\ LC50)}$ values for most of Nap and Pyr degraded intermediates are also lower than those of their parents. For the Nap and Pyr degraded intermediates, only P1 (4.39 mol L^{-1}, naphthalene-1,2-diol) and P3 (4.50 mol L^{-1}, naphthalene-1,4-diol) in Nap degraded intermediates have higher *Daphnia magna* -$Log_{10}^{(48\ h\ LC50)}$ values than their parent.

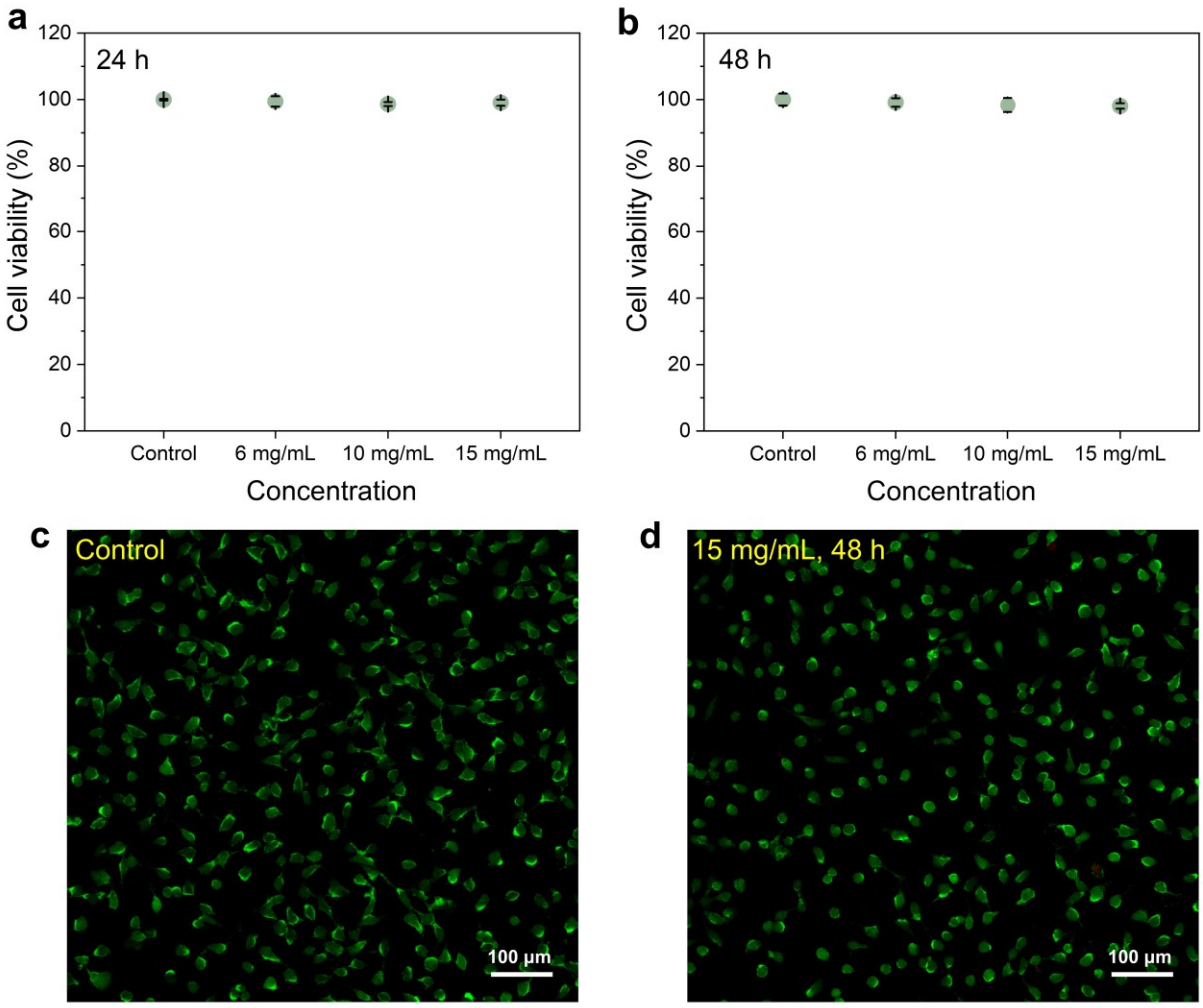

Supplementary Fig. 45. Biocompatibility of the laccase-assembled Cellulose-CD-MMT hydrogels. a, b Viability of L929 Mouse Fibroblast cells incubated with different concentrations (6-15 mg mL^{-1}, extracts) of laccase-assembled Cellulose-CD-MMT hydrogels at 24 h (**a**) and 48 h (**b**). **c, d** CLSM images of live (stained green)/dead (stained red) cells incubated with 0 mg mL^{-1} (**c**) and 15 mg mL^{-1} (**d**) of the laccase-assembled Cellulose-CD-MMT hydrogels (48 h). The cells without amendment of the laccase-assembled Cellulose-CD-MMT hydrogels were considered as controls, and their viability was set as 100%. For (**a-b**), data are presented as mean ± S.D. from three replicates (n = 3). Cell viability was measured using the standard in vitro cytotoxicity test method (ISO 10993-12/5; Cell Counting Kit-8: CCK8)[171-173].

Note: L929 Mouse Fibroblast cells are widely used to evaluate the biocompatibility of hydrogel materials[173-175]. As shown in Supplementary Fig. 45a-b, cytotoxicity of the laccase-assembled Cellulose-CD-MMT hydrogels at various concentrations (6-15 mg mL^{-1}, extracts) to L929 Mouse Fibroblast cells over 24 and 48 hours was negligible. Additionally, the CLSM live/dead

imaging of L929 Mouse Fibroblast cells incubated with extracts from the laccase-assembled Cellulose-CD-MMT hydrogels (15 mg mL^{-1}, 48 h) exhibited very few dead cells (Supplementary Fig. 45c-d). These results confirm the high degree of biocompatibility and low cytotoxicity of the laccase-assembled Cellulose-CD-MMT hydrogels, underscoring their potential for practical environmental remediation applications.

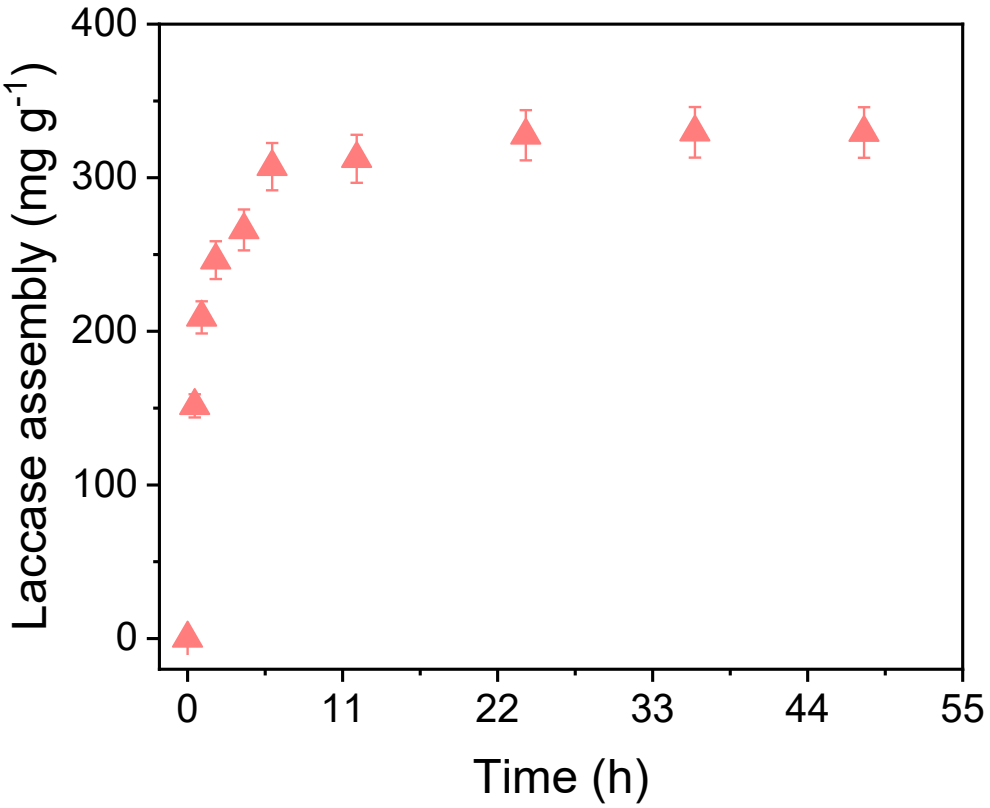

Supplementary Fig. 46. Assembly equilibrium time of laccase on the Cellulose-CD-MMT hydrogels at 1.0 mg mL^{-1}. Data are presented as mean ± S.D. from three replicates (n = 3). The assembly equilibrium was reached at 24 h.

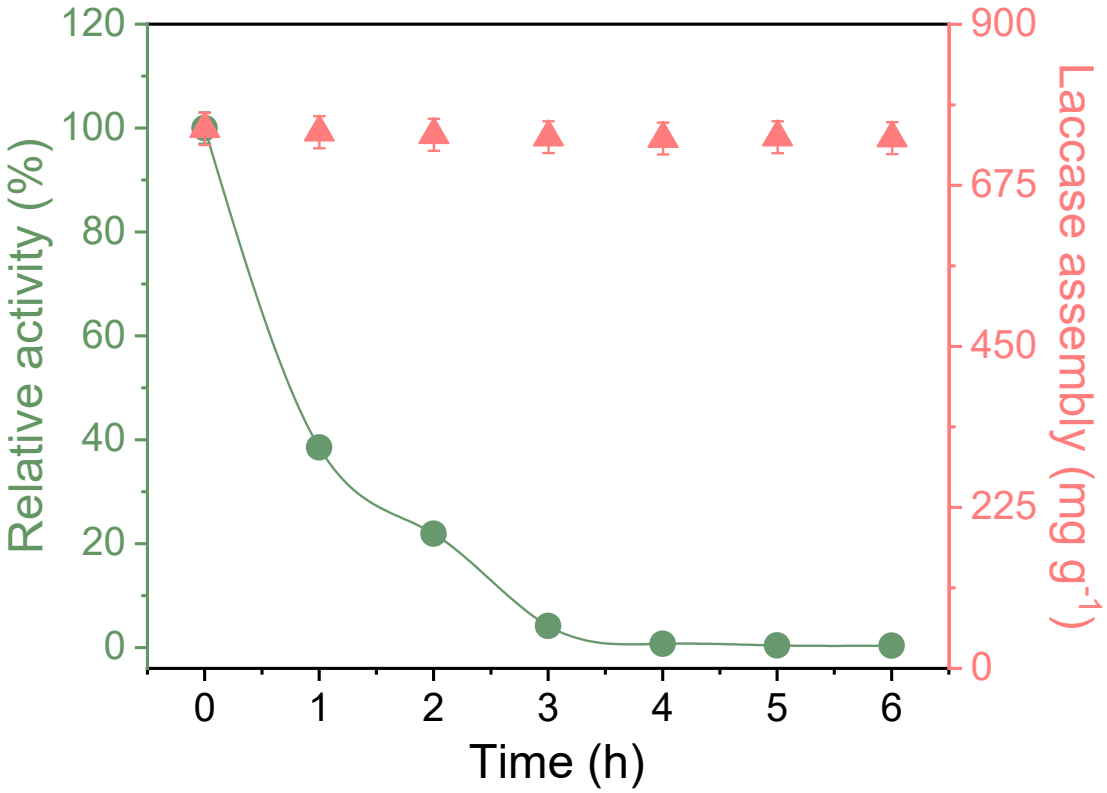

Supplementary Fig. 47. Variation of the relative activity and assembled amount of laccase at pH 10 and 90 °C within 0-6 h. Data are presented as mean ± S.D. from three replicates (*n* = 3). The assembled laccase became almost inactive after 6 h, while the assembled amount of laccase did not significantly change. Therefore, possible sorption of PAHs on the laccase-assembled hydrogels can be quantified by employing hydrogels assembled with inactivated laccase as a control. Symbols may cover error bars.

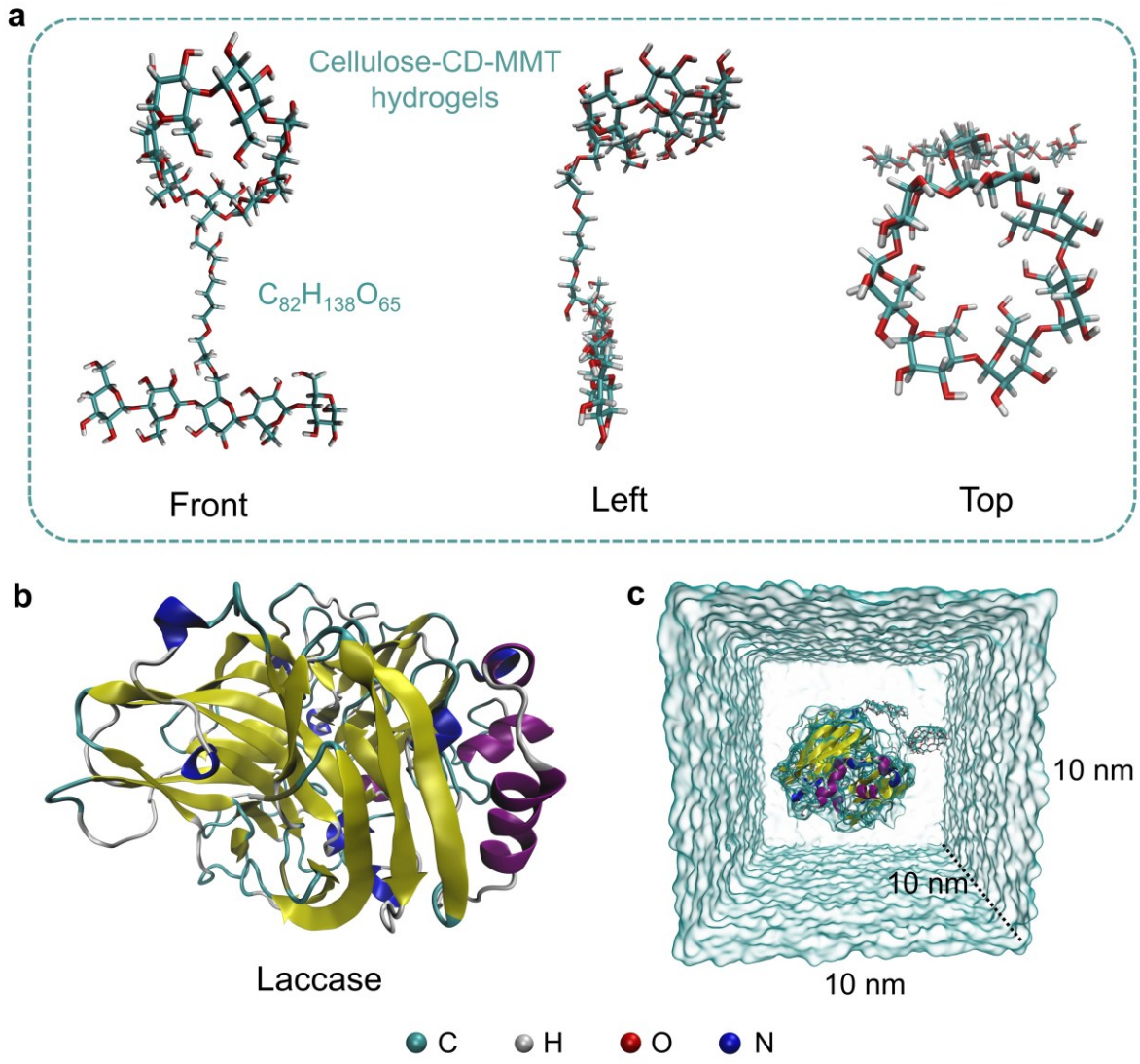

Supplementary Fig. 48. Models for MD simulation. a Cellulose-CD-MMT hydrogels. **b** Laccase (PDB ID: 1GYC). **c** The system containing hydrogels and laccase in a cubic water box of 10×10×10 nm. The specific details about MD simulation are summarized in Supplementary Note 9.

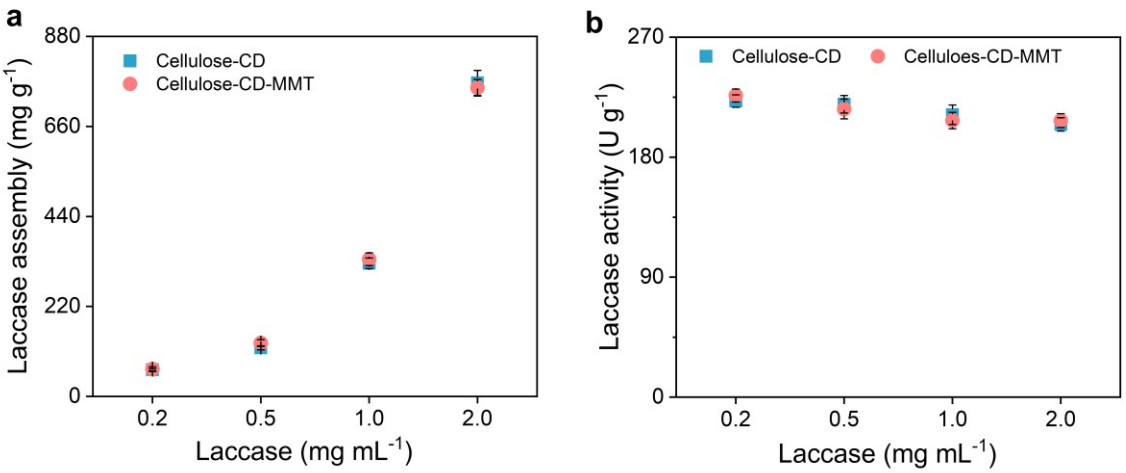

Supplementary Fig. 49. Assembled amount (a) and activity (b) of laccase on Cellulose-CD- and Cellulose-CD-MMT hydrogels. For (**a-b**), data are presented as mean ± S.D. from three replicates (n = 3). The assembled amount and activity of laccase on Cellulose-CD-MMT hydrogels are statistically comparable to those on the Cellulose-CD hydrogels, suggesting that the doped MMT has ignorable impact on the assembled amount and activity of laccase on hydrogels.

Supplementary References

1. Gilli, P., Pretto, L., Bertolasi, V. & Gilli, G. Predicting hydrogen-bond strengths from acid-base molecular properties. The pK_a slide rule: Toward the solution of a long-lasting problem. *Acc. Chem. Res.* **42**, 33-44 (2009).
2. Ward, M. D. Charge-assisted hydrogen-bonded networks. *Struct. Bonding (Berlin).* **132**, 1-23 (2009).
3. Fang, Y. et al. Charge-assisted hydrogen bond-directed self-assembly of an amphiphilic zwitterionic quinonemonoimine at the liquid–solid interface. *Chem. Commun.* **47**, 11255-11257 (2011).
4. Wang, P., Zhang, D., Tang, H., Li, H. & Pan, B. New insights on the understanding of the high adsorption of bisphenol compounds on reduced graphene oxide at high pH values via charge assisted hydrogen bond. *J. Hazard. Mater.* **371**, 513-520 (2019).
5. Li, X., Gámiz, B., Wang, Y., Pignatello, J. J. & Xing, B. Competitive sorption used to probe strong hydrogen bonding sites for weak organic acids on carbon nanotubes. *Environ. Sci. Technol.* **49**, 1409-1417 (2015).
6. Zhang, J. et al. Direct spectroscopic evidence for charge-assisted hydrogen-bond formation between ionizable organic chemicals and carbonaceous materials. *Environ. Sci. Technol.* **56**, 9356-9366 (2022).
7. Li, N., Liu, Y., Du, C., Wang, Y., Wang, L. & Li, X. A novel role of various hydrogen bonds in adsorption, desorption and co-adsorption of PPCPs on corn straw-derived biochars. *Sci. Total Environ.* **861**, 160623 (2023).
8. Liu, Y. et al. Various hydrogen bonds make different fates of pharmaceutical contaminants on oxygen-rich nanomaterials. *Environ. Pollut.* **316**, 120572 (2023).
9. Mahmudov, K. T., Kopylovich, M. N., Guedes da Silva, M. F. C. & Pombeiro, A. J. L. Non-covalent interactions in the synthesis of coordination compounds: Recent advances. *Coord. Chem. Rev.* **345**, 54-72 (2017).
10. Kah, M., Sigmund, G., Xiao, F. & Hofmann, T. Sorption of ionizable and ionic organic compounds to biochar, activated carbon and other carbonaceous materials. *Water Res.* **124**, 673-692 (2017).
11. Dereka, B., Yu, Q., Lewis, N. H. C., Carpenter, W. B., Bowman, J. M. & Tokmakoff, A. Crossover from hydrogen to chemical bonding. *Science* **371**, 160-164 (2021).
12. Li, X., Pignatello, J. J., Wang, Y. & Xing, B. New insight into adsorption mechanism of ionizable compounds on carbon nanotubes. *Environ. Sci. Technol.* **47**, 8334-8341 (2013).
13. Ling, C. et al. High adsorption of sulfamethoxazole by an amine-modified polystyrene–divinylbenzene resin and its mechanistic insight. *Environ. Sci. Technol.* **50**, 10015-10023 (2016).
14. Zhao, J. et al. Homo-conjugation of low molecular weight organic acids competes with their complexation with Cu(II). *Environ. Sci. Technol.* **52**, 5173-5181 (2018).
15. Xiao, F. & Pignatello, J. J. Effects of post-pyrolysis air oxidation of biomass chars on adsorption of neutral and ionizable compounds. *Environ. Sci. Technol.* **50**, 6276-6283 (2016).
16. Pignatello, J. J., Mitch, W. A. & Xu, W. Activity and reactivity of pyrogenic carbonaceous matter toward organic compounds. *Environ. Sci. Technol.* **51**, 8893-8908 (2017).
17. Bradford, M. M. Rapid and sensitive method for quantitation of microgram quantities of protein utilizing principle of protein-dye binding. *Anal. Biochem.* **72**, 248-254 (1976).
18. Xie, T., Liu, Z. & Wang, G. Structural basis for monolignol oxidation by a maize laccase. *Nat. Plants* **6**, 231-237 (2020).
19. Simón-Herrero, C. et al. Immobilized laccase on polyimide aerogels for removal of carbamazepine. *J. Hazard. Mater.* **376**, 83-90 (2019).
20. Wolfenden, B. S. & Willson, R. L. Radical-cations as reference chromogens in kinetic studies of one-electron transfer reactions: Pulse radiolysis studies of 2,2′ -azinobis-(3-ethylbenzthiazoline-6-sulphonate). *J. Chem. Soc., Perkin Trans.* **2**, 805-812 (1982).
21. Zhu, Y. et al. Continuous artificial synthesis of glucose precursor using enzyme-immobilized microfluidic reactors. *Nat. Commun.* **10**, 4049 (2019).
22. Kurwadkar, S., Sethi, S. S., Mishra, P. & Ambade, B. Unregulated discharge of wastewater in the mahanadi river basin: Risk evaluation due to occurrence of polycyclic aromatic hydrocarbon in surface water and sediments. *Mar. Pollut. Bull.* **179**, 113686 (2022).

23. Ololade, I. A., Apata, A. O., Oladoja, N. A., Alabi, B. A. & Ololade, O. O. Polycyclic aromatic hydrocarbons in rivers and health risk consequences of human exposure: A nigerian case study. *Int J Energ Water Res*. (2023). https://doi.org/10.1007/s42108-023-00236-1.
24. Xu, X. et al. Comprehensive insights into the occurrence, source, distribution and risk assessment of polycyclic aromatic hydrocarbons in a large drinking reservoir system. *Environ. Sci. Pollut. Res.* **29**, 6449-6462 (2021).
25. Chen, W. et al. Association of 16 priority polycyclic aromatic hydrocarbons with humic acid and humin fractions in a peat soil and implications for their long-term retention. *Environ. Pollut.* **230**, 882-890 (2017).
26. Chen, W. et al. Removal of PAHs at high concentrations in a soil washing solution containing TX-100 via simultaneous sorption and biodegradation processes by immobilized degrading bacteria in PVA-SA hydrogel beads. *J. Hazard. Mater.* **410**, 124533 (2021).
27. Qamar, Z., Khan, S., Khan, A., Aamir, M., Nawab, J. & Waqas, M. Appraisement, source apportionment and health risk of polycyclic aromatic hydrocarbons (PAHs) in vehicle-wash wastewater, Pakistan. *Sci. Total Environ.* **605-606**, 106-113 (2017).
28. Abraham, M. J. et al. Gromacs: High performance molecular simulations through multi-level parallelism from laptops to supercomputers. *SoftwareX* **1-2**, 19-25 (2015).
29. Zhang, D. et al. Mutagenesis and structural studies reveal the basis for the specific binding of SARS-CoV-2 SL3 RNA element with human TIA1 protein. *Nat. Commun.* **14**, 3715 (2023).
30. Antony, J., Grimme, S., Liakos, D. G. & Neese, F. Protein–ligand interaction energies with dispersion corrected density functional theory and high-level wave function based methods. *J. Phys. Chem. A.* **115**, 11210-11220 (2011).
31. Bursch, M., Mewes, J. M., Hansen, A. & Grimme, S. Best‐practice DFT protocols for basic molecular computational chemistry. *Angew. Chem. Int. Ed.* **61**, e202205735 (2022).
32. Gillespie, P. N. O. & Martsinovich, N. Electronic structure and charge transfer in the TiO_2 rutile (110)/graphene composite using hybrid DFT calculations. *J. Phys. Chem. C.* **121**, 4158-4171 (2017).
33. Frisch, M. J. et al. Gaussian 16., Revision C.01., (Gaussian, Inc., Wallingford C.T, 2016).
34. Maier, J. A., Martinez, C., Kasavajhala, K., Wickstrom, L., Hauser, K. E. & Simmerling, C. ff14SB: Improving the accuracy of protein side chain and backbone parameters from ff99SB. *J. Chem. Theory Comput.* **11**, 3696-3713 (2015).
35. Wang, J., Wolf, R. M., Caldwell, J. W., Kollman, P. A. & Case, D. A. Development and testing of a general amber force field. *J. Comput. Chem.* **25**, 1157-1174 (2004).
36. Lu, T. & Chen, F. Multiwfn: A multifunctional wavefunction analyzer. *J. Comput. Chem.* **33**, 580-592 (2012).
37. Zhang, J. & Lu, T. Efficient evaluation of electrostatic potential with computerized optimized code. *PCCP* **23**, 20323-20328 (2021).
38. Shen, Y. et al. Enzymatic polymerization of enantiomeric l-3,4-dihydroxyphenylalanine into films with enhanced rigidity and stability. *Nat. Commun.* **14**, 3054 (2023).
39. Humphrey, W., Dalke, A. & Schulten, K. VMD: Visual molecular dynamics. *J. Mol. Graphics* **14**, 33-38 (1996).
40. Goerigk, L., Kruse, H. & Grimme, S. Benchmarking density functional methods against the S66 and S66x8 datasets for non-covalent interactions. *Chemphyschem* **12**, 3421-3433 (2011).
41. Grimme, S., Ehrlich, S. & Goerigk, L. Effect of the damping function in dispersion corrected density functional theory. *J. Comput. Chem.* **32**, 1456-1465 (2011).
42. Xiao, R., Ye, T., Wei, Z., Luo, S., Yang, Z. & Spinney, R. Quantitative structure–activity relationship (QSAR) for the oxidation of trace organic contaminants by sulfate radical. *Environ. Sci. Technol.* **49**, 13394-13402 (2015).
43. Yoosefian, M., Ansarinik, Z. & Etminan, N. Density functional theory computational study on solvent effect, molecular conformations, energies and intramolecular hydrogen bond strength in different possible nano-conformers of acetaminophen. *J. Mol. Liq.* **213**, 115-121 (2016).
44. Akalin, E., Akyuz, S. & Akyuz, T. Adsorption and interaction of 5-fluorouracil with montmorillonite and saponite by FT-IR spectroscopy. *J. Mol. Struct.* **834-836**, 477-481 (2007).
45. Qiu, G., Huang, C., Sun, X. & Chen, B. Highly active niobium-loaded montmorillonite catalysts for the production of 5-hydroxymethylfurfural from glucose. *Green Chem.* **21**, 3930-3939 (2019).

46. Zhu, N., Zhang, M., Qiu, G., Tian, H. & Liu, Y. One-pot synthesis of 5-hydroxymethylfurfural from cellobiose and sucrose using niobium-modified montmorillonite catalysts. *Mol. Catal.* **532**, 112720 (2022).
47. Li, T., Wang, M. & Hao, Y. Highly efficient photodegradation of magnetic GO-Fe_3O_4@SiO_2@Cds for phenanthrene and pyrene: Mechanism insight and application assessment. *Sci. Total Environ.* **857**, 159254 (2023).
48. Yang, Z., Wang, Z., Wang, J., Li, Y. & Zhang, G. Facet-dependent activation of oxalic acid over magnetic recyclable Fe_3S_4 for efficient pollutant removal under visible light irradiation: Enhanced catalytic activity, DFT calculations, and mechanism insight. *Environ. Sci. Technol.* **56**, 18008-18017 (2022).
49. Zhu, Y., Ji, H., He, K., Blaney, L., Xu, T. & Zhao, D. Photocatalytic degradation of GenX in water using a new adsorptive photocatalyst. *Water Res.* **220**, 118650 (2022).
50. Wang, A. et al. Enhanced and synergistic catalytic activation by photoexcitation driven S−scheme heterojunction hydrogel interface electric field. *Nat. Commun.* **14**, 6733 (2023).
51. Yang, W. T. & Parr, R. G. Hardness, softness, and the fukui function in the electronic theory of metals and catalysis. *Proc. Natl. Acad. Sci. U. S. A.* **82**, 6723-6726 (1985).
52. Adeola, A. O. & Forbes, P. B. C. Assessment of reusable graphene wool adsorbent for the simultaneous removal of selected 2–6 ringed polycyclic aromatic hydrocarbons from aqueous solution. *Environ. Technol.* **43**, 1255-1268 (2020).
53. Angels Olivella, M., Jove, P., Sen, A., Pereira, H., Villaescusa, I. & Fiol, N. Sorption performance of quercus cerris cork with polycyclic aromatic hydrocarbons and toxicity testing. *Bioresources* **6**, 3363-3375 (2011).
54. Bruna, F., Celis, R., Real, M. & Cornejo, J. Organo/LDH nanocomposite as an adsorbent of polycyclic aromatic hydrocarbons in water and soil–water systems. *J. Hazard. Mater.* **225-226**, 74-80 (2012).
55. Kubheka, G., Adeola, A. O. & Forbes, P. B. C. Hexadecylamine functionalised graphene quantum dots as suitable nano-adsorbents for phenanthrene removal from aqueous solution. *RSC Adv.* **12**, 23922-23936 (2022).
56. Guo, W., Wang, S., Wang, Y., Lu, S. & Gao, Y. Sorptive removal of phenanthrene from aqueous solutions using magnetic and non-magnetic rice husk-derived biochars. *R. Soc. Open Sci.* **5**, 172382 (2018).
57. Zhao, H. et al. In situ forming cellulose nanofibril-reinforced hyaluronic acid hydrogel for cartilage regeneration. *Biomacromolecules* **22**, 5097-5107 (2021).
58. Ge, J. et al. Preparation and swelling behaviors of high-strength hemicellulose-g-polydopamine composite hydrogels. *Materials* **14**, 186 (2021).
59. Park, D., Kim, J. W., Shin, K. & Kim, J. W. Bacterial cellulose nanofibrils-reinforced composite hydrogels for mechanical compression-responsive on-demand drug release. *Carbohydr. Polym.* **272**, 118459 (2021).
60. Zhu, L., Liu, Y., Jiang, Z., Sakai, E., Qiu, J. & Zhu, P. Highly temperature resistant cellulose nanofiber/polyvinyl alcohol hydrogel using aldehyde cellulose nanofiber as cross-linker. *Cellulose* **26**, 5291-5303 (2019).
61. Shu, L., Wang, Z., Zhang, X. F. & Yao, J. Highly conductive and anti-freezing cellulose hydrogel for flexible sensors. *Int. J. Biol. Macromol.* **230**, 123425 (2023).
62. Luo, J. et al. Multifunctioning of carboxylic-cellulose nanocrystals on the reinforcement of compressive strength and conductivity for acrylic-based hydrogel. *Carbohydr. Polym.* **327**, 121685 (2024).
63. Zhang, M. et al. A strategy of tailoring polymorphs and nanostructures to construct self-reinforced nonswelling high-strength bacterial cellulose hydrogels. *Nanoscale* **11**, 15347-15358 (2019).
64. Wang, S. et al. Strong, tough, ionic conductive, and freezing-tolerant all-natural hydrogel enabled by cellulose-bentonite coordination interactions. *Nat. Commun.* **13**, 3408 (2022).
65. Liu, Q., Liu, J., Qin, S., Pei, Y., Zheng, X. & Tang, K. High mechanical strength gelatin composite hydrogels reinforced by cellulose nanofibrils with unique beads-on-a-string morphology. *Int. J. Biol. Macromol.* **164**, 1776-1784 (2020).
66. Yu, X. et al. Double network microcrystalline cellulose hydrogels with high mechanical strength and biocompatibility for cartilage tissue engineering scaffold. *Int. J. Biol. Macromol.* **238**, 124113 (2023).

67. Tang, Z., Yu, M., Yang, Y., Pan, Y., Mondal, A. K. & Lin, X. Development of an antioxidant and UV-shielding composite hydrogel using mussel-inspired cellulose nanocrystals, polydopamine, and poly(vinyl alcohol) for application in sunscreens. *ACS Appl. Polym. Mater.* **5**, 6625-6632 (2023).
68. Lin, F. et al. In situ polymerization approach to cellulose–polyacrylamide interpenetrating network hydrogel with high strength and pH-responsive properties. *Cellulose* **26**, 1825-1839 (2019).
69. Gokhale, D., Hamelberg, A. F. & Doyle, P. S. Multifunctional zwitterionic hydrogels for the rapid elimination of organic and inorganic micropollutants from water. *Nat. Water* **2**, 62-71 (2024).
70. Weerasundara, L., Gabriele, B., Figoli, A., Ok, Y.S. & Bundschuh, J. Hydrogels: Novel materials for contaminant removal in water-a review. *Crit. Rev. Environ. Sci. Technol.* **51**, 1970-2014 (2020).
71. Zhang, F. et al. Laccase immobilized on functionalized cellulose nanofiber/alginate composite hydrogel for efficient bisphenol a degradation from polluted water. *Adv. Compos. Hybrid Mater.* **5**, 1852-1864 (2022).
72. Lin, K. et al. How can vanillin improve the performance of lignocellulosic biomass conversion in an immobilized laccase microreactor system? *Bioresour. Technol.* **374**, 128775 (2023).
73. Lou, X. et al. Construction of co-immobilized laccase and mediator based on MOFs membrane for enhancing organic pollutants removal. *Chem. Eng. J.* **451**, 138080 (2023).
74. Qiu, X., Wang, S., Miao, S., Suo, H., Xu, H. & Hu, Y. Co-immobilization of laccase and ABTS onto amino-functionalized ionic liquid-modified magnetic chitosan nanoparticles for pollutants removal. *J. Hazard. Mater.* **401**, 123353 (2021).
75. Bao, C. et al. Reversible immobilization of laccase onto glycopolymer microspheres via protein-carbohydrate interaction for biodegradation of phenolic compounds. *Bioresour. Technol.* **342**, 126026 (2021).
76. Wu, D. et al. Biomass-derived nanocellulose aerogel enable highly efficient immobilization of laccase for the degradation of organic pollutants. *Bioresour. Technol.* **356**, 127311 (2022).
77. Sun, H., Yuan, F., Jia, S., Zhang, X. & Xing, W. Laccase encapsulation immobilized in mesoporous ZIF-8 for enhancement bisphenol a degradation. *J. Hazard. Mater.* **445**, 130460 (2023).
78. Tang, Y. et al. Fabrication of hollow covalent-organic framework microspheres via emulsion-interfacial strategy to enhance laccase immobilization for tetracycline degradation. *Chem. Eng. J.* **421**, 129743 (2021).
79. Shao, B. et al. Immobilization of laccase on hollow mesoporous carbon nanospheres: Noteworthy immobilization, excellent stability and efficacious for antibiotic contaminants removal. *J. Hazard. Mater.* **362**, 318-326 (2019).
80. Banjare, M. K., Behera, K., Satnami, M. L., Pandey, S. & Ghosh, K. K. Host–guest complexation of ionic liquid with α- and β-cyclodextrins: A comparative study by ^{1}H-NMR, ^{13}C-NMR and cosy. *New J. Chem.* **42**, 14542-14550 (2018).
81. Del Campo, G., Zuriarrain, J., Zuriarrain, A. & Berregi, I. Quantitative determination of carboxylic acids, amino acids, carbohydrates, ethanol and hydroxymethylfurfural in honey by ^{1}H NMR. *Food Chem.* **196**, 1031-1039 (2016).
82. Hesse-Ertelt, S., Heinze, T., Kosan, B., Schwikal, K. & Meister, F. Solvent effects on the NMR chemical shifts of imidazolium-based ionic liquids and cellulose therein. *Macromol. Symp.* **294**, 75-89 (2010).
83. Zivkovic, A. et al. Introducing students to NMR methods using low-field ^{1}H NMR spectroscopy to determine the structure and the identity of natural amino acids. *J. Chem. Educ.* **94**, 115-120 (2016).
84. Sorgenfrei, N. et al. NMR spectroscopic characterization of charge assisted strong hydrogen bonds in brønsted acid catalysis. *J. Am. Chem. Soc.* **138**, 16345-16354 (2016).
85. Xu, R., Zhou, Q., Li, F. & Zhang, B. Laccase immobilization on chitosan/poly(vinyl alcohol) composite nanofibrous membranes for 2,4-dichlorophenol removal. *Chem. Eng. J.* **222**, 321-329 (2013).
86. Jiang, S., Ren, D., Wang, Z., Zhang, S., Zhang, X. & Chen, W. Improved stability and promoted activity of laccase by One-Pot encapsulation with Cu (PABA) nanoarchitectonics and its application for removal of Azo dyes. *Ecotoxicol. Environ. Saf.* **234**, 113366 (2022).
87. Ormategui, N., Veloso, A., Leal, G. P., Rodriguez-Couto, S. & Tomovska, R. Design of stable and powerful nanobiocatalysts, based on enzyme laccase immobilized on self-assembled 3D graphene/polymer composite hydrogels. *ACS Appl. Mater. Interfaces* **7**, 14104-14112 (2015).

88. Yang, X., Chen, X., Wang, H., Cavaco-Paulo, A. & Su, J. Co-immobilizing laccase-mediator system by in-situ synthesis of MOF in PVA hydrogels for enhanced laccase stability and dye decolorization efficiency. *J. Environ. Manage.* **353**, 120114 (2024).
89. Zhu, Y. et al. Encapsulation of laccase within zwitterionic poly-carboxybetaine hydrogels for improved activity and stability. *Catal. Sci. Technol.* **8**, 5217-5224 (2018).
90. El-Bendary, M. A., Ezzat, S. M., Ewais, E. A. & Al-Zalama, M. A. Efficient immobilization of highly stable bacillus amyloliquefaciens spore laccase for biodecolorization of textile dyes in water. *Environ. Sci. Eur.* **36**, 36 (2024).
91. Du, M. et al. Spatial nanopores promote laccase degradation of bisphenol a and its analogs. *Sci. Total Environ.* **901**, 166429 (2023).
92. Liu, J. et al. Immobilization of laccase by 3D bioprinting and its application in the biodegradation of phenolic compounds. *Int. J. Biol. Macromol.* **164**, 518-525 (2020).
93. Niu, J., Dai, Y., Guo, H., Xu, J. & Shen, Z. Adsorption and transformation of PAHs from water by a laccase-loading spider-type reactor. *J. Hazard. Mater.* **248-249**, 254-260 (2013).
94. Dai, Y., Niu, J., Yin, L., Xu, J. & Xu, J. Laccase-carrying electrospun fibrous membrane for the removal of polycyclic aromatic hydrocarbons from contaminated water. *Sep. Purif. Technol.* **104**, 1-8 (2013).
95. Vaidyanathan, V. K. et al. Removal of pentachlorophenol and phenanthrene from lignocellulosic biorefinery wastewater by a biocatalytic/biosurfactant system comprising cross-linked laccase aggregates and rhamnolipid. *Environ. Pollut.* **329**, 121635 (2023).
96. Rocha, A. B. et al. Shrimp laccase degrades polycyclic aromatic hydrocarbons from an oil spill disaster in brazil: A tool for marine environmental bioremediation. *Mar. Pollut. Bull.* **194**, 115445 (2023).
97. Deng, J. et al. Catalyzed degradation of polycyclic aromatic hydrocarbons by recoverable magnetic chitosan immobilized laccase from trametes versicolor. *Chemosphere* **301**, 134753 (2022).
98. Goudarzi, S. et al. Laccase-functionalized hexagonal boron nitride-coated sponges for the removal and degradation of anthracene. *ACS Appl. Nano Mater.* **5**, 4493-4505 (2022).
99. Perini, B. L. B., Daronch, N. A., Bitencourt, R. L., Santos Schneider, A. L., Andrade, C. J. & Oliveira, D. Application of immobilized laccase on polyurethane foam for ex-situ polycyclic aromatic hydrocarbons bioremediation. *J. Polym. Environ.* **29**, 2200-2213 (2021).
100. Wulandari, R., Lotrakul, P., Punnapayak, H., Amirta, R., Kim, S. W. & Prasongsuk, S. Toxicity evaluation and biodegradation of phenanthrene by laccase from *Trametes polyzona* PBURU 12. *3 Biotech* **11**, 32 (2021).
101. Ike, P. T. L., Birolli, W. G., dos Santos, D. M., Porto, A. L. M. & Souza, D. H. F. Biodegradation of anthracene and different PAHs by a yellow laccase from *Leucoagaricus gongylophorus*. *Environ. Sci. Pollut. Res.* **26**, 8675-8684 (2019).
102. Dodor, D. E., Miyittah, M. & Ahiabor, B. D. K. Immobilized laccase mediator-catalyzed oxidation of aqueous mixtures of polycyclic aromatic hydrocarbons. *Polycyc. Aromatic Compounds* **40**, 563-573 (2020).
103. Bautista, L. F., Morales, G. & Sanz, R. Biodegradation of polycyclic aromatic hydrocarbons (PAHs) by laccase from *Trametes versicolor* covalently immobilized on amino-functionalized SBA-15. *Chemosphere* **136**, 273-280 (2015).
104. Majcherczyk, A., Johannes, C. & Hüttermann, A. Oxidation of polycyclic aromatic hydrocarbons (PAH) by laccase of *Trametes versicolor*. *Enzyme Microb. Technol.* **22**, 335-341 (1998).
105. Pozdnyakova, N. N., Rodakiewicz-Nowak, J., Turkovskaya, O. V. & Haber, J. Oxidative degradation of polyaromatic hydrocarbons and their derivatives catalyzed directly by the yellow laccase from *Pleurotus ostreatus* D1. *J. Mol. Catal. B: Enzym.* **41**, 8-15 (2006).
106. Han, M. J., Park, H. T. & Song, H. G. Degradation of phenanthrene by *Trametes versicolor* and its laccase. *J. Microbiol.* **42**, 94-98 (2004).
107. Chang, Y. T., Lee, J. F., Liu, K. H., Liao, Y. F. & Yang, V. Immobilization of fungal laccase onto a nonionic surfactant-modified clay material: Application to PAH degradation. *Environ. Sci. Pollut. Res.* **23**, 4024-4035 (2016).
108. Mayolo-Deloisa, K., Machín-Ramírez, C., Rito-Palomares, M. & Trejo-Hernández, M. R. Oxidation of polycyclic aromatic hydrocarbons using partially purified laccase from residual compost of *Agaricus bisporus*. *Chem. Eng. Technol.* **34**, 1368-1372 (2011).
109. Zeng, J., Lin, X., Zhang, J., Li, X. & Wong, M. H. Oxidation of polycyclic aromatic hydrocarbons by the bacterial laccase CueO from *E. Coli. Appl. Microbiol. Biotechnol.* **89**, 1841-1849 (2011).

110. Dong, W., Yan, J., Yang, Y., Wu, Q. & Hu, X. Immobilization of laccase on magnetic mesoporous silica as a recoverable biocatalyst for the efficient degradation of benzo[*a*]pyrene. *Chemosphere* **346**, 140642 (2024).
111. Fernando Bautista, L., Morales, G. & Sanz, R. Immobilization strategies for laccase from *Trametes versicolor* on mesostructured silica materials and the application to the degradation of naphthalene. *Bioresour. Technol.* **101**, 8541-8548 (2010).
112. Chen, X., Hu, Z., Xie, H., Ngo, H. H., Guo, W. & Zhang, J. Enhanced biocatalysis of phenanthrene in aqueous phase by novel CA-Ca-SBE-laccase biocatalyst: Performance and mechanism. *Colloids Surf. Physicochem. Eng. Aspects* **611**, 125884 (2021).
113. Saber, A. N., Djellabi, R., Fellah, I., Abderrahim, N. & Bianchi, C. L. Synergistic sorption/photo-Fenton removal of typical substituted and parent polycyclic aromatic hydrocarbons from coking wastewater over CuO-montmorillonite. *J. Water Process Eng.* **44**, 102377 (2021).
114. Bai, X., Sun, H., Sun, J. & Zhu, Z. Efficient removal of sixteen priority polycyclic aromatic hydrocarbons from textile dyeing sludge using electrochemical Fe^{2+}-activated peroxymonosulfate oxidation-a green pretreatment strategy for textile dyeing sludge toxicity reduction. *J. Hazard. Mater.* **435**, 129087 (2022).
115. Ke, Y. et al. Sludge treatment by integrated ultrasound-Fenton process: Characterization of sludge organic matter and its impact on PAHs removal. *J. Hazard. Mater.* **343**, 191-199 (2018).
116. Al Sbani, N. H. et al. PAH-degrading rhizobacteria of *Lepironia articulata* for phytoremediation enhancement. *J. Water Process Eng.* **39**, 101688 (2021).
117. Ordonez, D., Valencia, A., Sadmani, A. H. M. A. & Chang, N.-B. Green sorption media for the removal of perfluorooctanesulfonic acid (PFOS) and perfluorooctanoic acid (PFOA) from water. *Sci. Total Environ.* **819**, 152886 (2022).
118. Luo, Q., Yan, X., Lu, J. & Huang, Q. Perfluorooctanesulfonate degrades in a laccase-mediator system. *Environ. Sci. Technol.* **52**, 10617-10626 (2018).
119. Pierpaoli, M. et al. Electrochemical oxidation of PFOA and PFOS in landfill leachates at low and highly boron-doped diamond electrodes. *J. Hazard. Mater.* **403**, 123606 (2021).
120. Uwayezu, J. N., Carabante, I., van Hees, P., Karlsson, P. & Kumpiene, J. Combining electrochemistry and ultraviolet radiation for the degradation of per- and poly-fluoroalkyl substances in contaminated groundwater and wastewater. *J. Water Process Eng.* **54**, 104028 (2023).
121. Jiang, Y. et al. Insights to PFOS elimination with peroxydisulfate activation mediated by boron modified Fe/C catalysts: Enhancing mechanism of boron and PFOS degradation pathway. *J. Colloid Interface Sci.* **652**, 1743-1755 (2023).
122. Chen, J. et al. Effective biodegradation of chlorophenols, sulfonamides, and their mixtures by bacterial laccase immobilized on chitin. *Ecotoxicol. Environ. Saf.* **256**, 114856 (2023).
123. Liu, X. et al. Intensified sulfamethoxazole removal in an electrolysis-integrated tidal flow constructed wetland system. *Chem. Eng. J.* **390**, 124545 (2020).
124. Huang, J., Zimmerman, A. R., Chen, H. & Gao, B. Ball milled biochar effectively removes sulfamethoxazole and sulfapyridine antibiotics from water and wastewater. *Environ. Pollut.* **258**, 113809 (2020).
125. Li, J., Wang, F., Meng, L., Han, M., Guo, Y. & Sun, C. Controlled synthesis of $BiVO_4/SrTiO_3$ composite with enhanced sunlight-driven photofunctions for sulfamethoxazole removal. *J. Colloid Interface Sci.* **485**, 116-122 (2017).
126. Huang, D. et al. Nitrogen-doped nanocarbon derived from candle soot for persulfate activation on sulfamethoxazole removal: Performance and mechanism. *J. Colloid Interface Sci.* **629**, 685-696 (2023).
127. Lin, N. & Dufresne, A. Supramolecular hydrogels from in situ host–guest inclusion between chemically modified cellulose nanocrystals and cyclodextrin. *Biomacromolecules* **14**, 871-880 (2013).
128. Alam, M. N., Islam, M. S. & Christopher, L. P. Sustainable production of cellulose-based hydrogels with superb absorbing potential in physiological saline. *ACS Omega.* **4**, 9419-9426 (2019).
129. Li, Y., Shen, S., Wang, C., Peng, X. & Yuan, S. The effect of difference in chemical composition between cellulose and lignin on carbon based solid acids applied for cellulose hydrolysis. *Cellulose* **25**, 1851-1863 (2018).
130. Bou, M., Martin, J. M., Le Mogne, T. & Vovelle, L. Chemistry of the interface between aluminium and polyethyleneterephthalate by XPS. *Appl. Surf. Sci.* **47**, 149-161 (1991).

131. Chen, E., Bevilacqua, M., Tavagnacco, C., Montini, T., Yang, C. M. & Fornasiero, P. High surface area N/O co-doped carbon materials: Selective electrocatalysts for O_2 reduction to H_2O_2. *Catal. Today* **356**, 132-140 (2020).
132. Li, X. et al. Effect of pH-dependent homo/heteronuclear CAHB on adsorption and desorption behaviors of ionizable organic compounds on carbonaceous materials. *Int. J. Environ. Res. Public Health* **19**, 12118 (**2022)**.
133. Chen, L. et al. Scalable production of biodegradable, recyclable, sustainable cellulose–mineral foams via coordination interaction assisted ambient drying. *ACS Nano* **16**, 16414-16425 (2022).
134. Jlassi, K., Sliem, M. H., Benslimane, F. M., Eltai, N. O. & Abdullah, A. M. Design of hybrid clay/ polypyrrole decorated with silver and zinc oxide nanoparticles for anticorrosive and antibacterial applications. *Prog. Org. Coat.* **149**, 105958 (2020).
135. Ye, X., Shang, S., Zhao, Y., Cui, S., Zhong, Y. & Huang, L. Ultra-efficient adsorption of copper ions in chitosan–montmorillonite composite aerogel at wastewater treatment. *Cellulose* **28**, 7201-7212 (2021).
136. Bridelli, M. G., Stani, C. & Bedotti, R. Fourier transform infrared conformational investigation of type I collagen aged by in vitro induced dehydration and non-enzymatic glycation treatments. *J. Biol. Res.* **90**, 6254 (2017).
137. Ji, N., Liu, C., Li, M., Sun, Q. & Xiong, L. Interaction of cellulose nanocrystals and amylase: Its influence on enzyme activity and resistant starch content. *Food Chem.* **245**, 481-487 (2018).
138. Alsbaiee, A., Smith, B. J., Xiao, L., Ling, Y., Helbling, D. E. & Dichtel, W. R. Rapid removal of organic micropollutants from water by a porous β-cyclodextrin polymer. *Nature* **529**, 190-194 (2016).
139. Lin, Z. W. et al. Trace organic contaminant removal from municipal wastewater by styrenic β-cyclodextrin polymers. *Environ. Sci. Technol.* **57**, 19624-19636 (2023).
140. Ling, Y., Klemes, M. J., Xiao, L., Alsbaiee, A., Dichtel, W. R. & Helbling, D. E. Benchmarking micropollutant removal by activated carbon and porous β-cyclodextrin polymers under environmentally relevant scenarios. *Environ. Sci. Technol.* **51**, 7590-7598 (2017).
141. Baltacıoğlu, H., Bayındırlı, A. & Severcan, F. Secondary structure and conformational change of mushroom polyphenol oxidase during thermosonication treatment by using ftir spectroscopy. *Food Chem.* **214**, 507-514 (2017).
142. Yu, X., Zou, F., Li, Y., Lu, L., Huang, X. & Qu, Y. Effect of three trifluoromethanesulfonate ionic liquids on the activity, stability and conformation of laccase. *Int. J. Biol. Macromol.* **56**, 62-68 (2013).
143. López-Cruz, J. I., Viniegra-González, G. & Hernández-Arana, A. Thermostability of native and pegylated Myceliophthora thermophila laccase in aqueous and mixed solvents. *Bioconj. Chem.* **17**, 1093-1098 (2006).
144. Liang, W., Chen, X., Zhao, C., Li, L. & He, D. Seasonal changes of dissolved organic matter chemistry and its linkage with greenhouse gas emissions in saltmarsh surface water and porewater interactions. *Water Res.* **245**, 120582 (2023).
145. Liu, L., Liu, Y., Gao, B., Ji, R., Li, C. & Wang, S. Removal of perfluorooctanoic acid (PFOA) and perfluorooctane sulfonate (PFOS) from water by carbonaceous nanomaterials: A review. *Crit. Rev. Environ. Sci. Technol.* **50**, 2379-2414 (2019).
146. Ratié, G., Chrastný, V., Guinoiseau, D., Marsac, R., Vaňková, Z. & Komárek, M. Cadmium isotope fractionation during complexation with humic acid. *Environ. Sci. Technol.* **55**, 7430-7444 (2021).
147. Selvam, S. et al. Human health risk assessment of heavy metal and pathogenic contamination in surface water of the Punnakayal estuary, south India. *Chemosphere* **298**, 134027 (2022).
148. Sims, J. L. et al. Global occurrence and probabilistic environmental health hazard assessment of per- and polyfluoroalkyl substances (PFASs) in groundwater and surface waters. *Sci. Total Environ.* **816**, 151535 (2022)
149. Balabushevich, N. G. et al. Immobilization of antioxidant enzyme catalase on porous hybrid microparticles of vaterite with mucin. *Adv. Eng. Mater.* **24**, 2101797 (2022).
150. Liang, W. et al. Enhanced activity of enzymes encapsulated in hydrophilic metal–organic frameworks. *J. Am. Chem. Soc.* **141**, 2348-2355 (2019).
151. Zhang, J. et al. Adsorption, desorption and coadsorption behaviors of sulfamerazine, Pb(II) and benzoic acid on carbon nanotubes and nano-silica. *Sci. Total Environ.* **738**, 139685 (2020).

152. Li, Y. M. et al. Fine-tuning the micro-environment to optimize the catalytic activity of enzymes immobilized in multivariate metal-organic frameworks. *J. Am. Chem. Soc.* **143**, 15378-15390 (2021).
153. Świderek, K. et al. Mechanistic studies of a lipase unveil effect of pH on hydrolysis products of small PET modules. *Nat. Commun.* **14**, 3556 (2023).
154. Chen, Q. et al. Active and stable alcohol dehydrogenase-assembled hydrogels via synergistic bridging of triazoles and metal ions. *Nat. Commun.* **14**, 2117 (2023).
155. Romero-Arcos, M., Pérez-Robles, J. F., Guadalupe Garnica-Romo, M., Luna-Martinez, M. S. & Gonzalez-Reyna, M. A. Synthesis and functionalization of carbon nanotubes and nanospheres as a support for the immobilization of an enzyme extract from the mushroom trametes versicolor. *J. Mater. Sci.* **54**, 11671-11681 (2019).
156. Coros, M., Varodi, C., Pogacean, F., Gal, E. & Pruneanu, S. M. Nitrogen-doped graphene: The influence of doping level on the charge-transfer resistance and apparent heterogeneous electron transfer rate. *Sensors* **20**, 1815 (2020).
157. Moradi, S., Shokri, Z., Ghorashi, N., Navaee, A. & Rostami, A. Design and synthesis of a versatile cooperative catalytic aerobic oxidation system with co-immobilization of palladium nanoparticles and laccase into the cavities of mcf. *J. Catal.* **382**, 305-319 (2020).
158. Dai, S. et al. Low-barrier hydrogen bonds in enzyme cooperativity. *Nature* **573**, 609-613 (2019).
159. Borshchevskiy, V. et al. True-atomic-resolution insights into the structure and functional role of linear chains and low-barrier hydrogen bonds in proteins. *Nat. Struct. Mol. Biol.* **29**, 440-450 (2022).
160. Yang, K. R., Lakshmi, K. V., Brudvig, G. W. & Batista, V. S. Is deprotonation of the oxygen-evolving complex of photosystem II during the $S_1 \rightarrow S_2$ transition suppressed by proton quantum delocalization? *J. Am. Chem. Soc.* **143**, 8324-8332 (2021).
161. Peng, F. et al. Selective electrochemical oxidation of benzylic C–H to benzylic alcohols with the aid of imidazolium radical mediators. *J. Am. Chem. Soc.* **145**, 23905-23909 (2023).
162. Wang, Z. et al. Enhanced mass transfer of ozone and emerging pollutants through a gas–solid–liquid reaction interface for efficient water decontamination. *Environ. Sci. Technol.* **57**, 18647-18657 (2023).
163. Zhong, C., Cao, H., Huang, Q., Xie, Y. & Zhao, H. Degradation of sulfamethoxazole by manganese(IV) oxide in the presence of humic acid: Role of stabilized semiquinone radicals. *Environ. Sci. Technol.* **57**, 13625-13634 (2023).
164. Li, K. et al. Significantly accelerated photochemical perfluorooctanoic acid decomposition at the air-water interface of microdroplets. *Environ. Sci. Technol.* **57**, 21448-21458 (2023).
165. Ewusi, A., Sunkari, E. D., Seidu, J. & Coffie-Anum, E. Hydrogeochemical characteristics, sources and human health risk assessment of heavy metal dispersion in the mine pit water–surface water–groundwater system in the largest manganese mine in Ghana. *Environ. Technol. Innovation.* **26**, 102312 (2022).
166. Hu, J. et al. Interaction analysis of hydrochemical factors and dissolved heavy metals in the karst Caohai Wetland based on PHREEQC, cooccurrence network and redundancy analyses. *Sci. Total Environ.* **770**, 145361 (2021).
167. Wu, S., Li, H., Li, X., He, H. & Yang, C. Performances and mechanisms of efficient degradation of atrazine using peroxymonosulfate and ferrate as oxidants. *Chem. Eng. J.* **353**, 533-541 (2018).
168. Famiglini, G., Palma, P., Termopoli, V. & Cappiello, A. The history of electron ionization in LC-MS, from the early days to modern technologies: A review. *Anal. Chim. Acta* **1167**, 338350 (2021).
169. Fang, J., Zhao, H., Zhang, Y., Lu, M. & Cai, Z. Atmospheric pressure chemical ionization in gas chromatography-mass spectrometry for the analysis of persistent organic pollutants. *Trends Environ. Anal. Chem.* **25**, e00076 (2020).
170. Wang, Y., Sun, J., Qiao, J., Ouyang, J. & Na, N. A "soft" and "hard" ionization method for comprehensive studies of molecules. *Anal. Chem.* **90**, 14095-14099 (2018).
171. Gonciarz, W., Chmiela, M., Kost, B., Piątczak, E. & Brzeziński, M. Stereocomplexed microparticles loaded with *Salvia cadmica* Boiss. Extracts for enhancement of immune response towards *Helicobacter pylori. Sci. Rep.* **13**, 7039 (2023).
172. Huang, Y. et al. Ultrasound-activated piezo-hot carriers trigger tandem catalysis coordinating cuproptosis-like bacterial death against implant infections. *Nat. Commun.* **15**, 1643 (2024).
173. Tang, Z. et al. A general protein unfolding-chemical coupling strategy for pure protein hydrogels with mechanically strong and multifunctional properties. *Adv. Sci.* **9**, 2102557 (2022).

174. Luo, Q. et al. Non-toxic chitosan-based hydrogel with strong adsorption and sensitive detection abilities for tetracycline. *Chem. Eng. J.* **427**, 131738 (2022).
175. Yang, F. et al. A synthetic hydrogel composite with the mechanical behavior and durability of cartilage. *Adv. Funct. Mater.* **30**, 2003451 (2020).